FLORIDA STATE UNIVERSITY

COLLEGE OF ENGINEERING

UNCERTAINTY ANALYSIS OF MULTIFUNCTIONAL CONSTITUTIVE RELATIONS AND ADAPTIVE STRUCTURES

By

PAUL R. MILES

A Dissertation submitted to the
Department of Mechanical Engineering
in partial fulfillment of the
requirements for the degree of
Doctor of Philosophy

2017

Paul R. Miles defended this dissertation on June 22, 2017.
The members of the supervisory committee were:

William Oates
Professor Co-Directing Dissertation

M. Yousuff Hussaini
Professor Co-Directing Dissertation

Changchun Zeng
University Representative

Kunihiko Taira
Committee Member

Shangchao Lin
Committee Member

Ralph Smith
Committee Member

The Graduate School has verified and approved the above-named committee members, and certifies that the dissertation has been approved in accordance with university requirements.

To my wife, whose persevering work ethic and patience have been inspirational to me.

ACKNOWLEDGMENTS

I am indebted to the faculty from various institutions who have invested their lives in me. From Florida State University I must give special thanks to Dr. Oates for giving me the opportunity to work in his lab group and for the encouragement he has provided over the last four years. My research has encompassed far more than I could have imagined, and I will always admire Dr. Oates's ability to work on such a broad range of topics. My thanks to Dr. Taira and his entire lab group for letting me pretend to be a CFD student - the enthusiam with which they approach their research made for a fantastic work environment. Thank you Dr. Hussaini for your guidance in exploring new areas of research and for all the wonderful stories - I am also extremely grateful for the second office in which I was able to hide. I also wish to thank Dr. Lin and Dr. Zeng for their feedback on my research and for serving on my committee. Thanks also to the support from Dr. Smith from North Carolina State University, especially for his assistance in learning more about uncertainty quantification.

The desire to pursue graduate school came from the encouragement I received from the entire mechanical engineering program at Grove City College, especially from my advisor, Dr. Clauss. Her commitment to detail and enthusiasm for teaching provided an excellent role model for working in academia. I am also very grateful for the support and mentoring provided by many other faculty as well as retired faculty from Grove City College. My thanks to Mr. and Mrs. Leo for their continuous encouragement and the example they set by their heart for serving others.

I am extremely indebted to the instruction provided by my high school chemistry and physics professor, Dr. Dieter, whose approach to teaching served as excellent preparation for college classes (I still use unit multipliers at least once every day). My thanks to Mr. Hagin for providing an introduction to robotics and encouraging me to learn more about statistics. A truly exhaustive listing of people who have made an impact on my life would extend well beyond the length of this dissertation, but please know that the encouragement I have received along the way has meant more than I can express.

Additional thanks must be given to my parents, especially my mother's tireless efforts of getting me through a home school curriculum - I will always miss the lunch hours spent playing Scrabble. My father set an extraordinary example of life-long learning and encouragement, and I am excited to follow his example. The journey has been made more joyful by sharing it with my wife, whose ability to listen and make me smile have brought me through many challenges. The road to get here has been much different than I ever could have expected, and I am grateful to God for providing me with these invaluable sources of encouragement along the way.

TABLE OF CONTENTS

List of Tables ix
List of Figures xi
Abstract xvii

1 Introduction 1
1.1 Dielectric Elastomers 1
1.2 Ferroelectric Materials 3
1.3 Uncertainty Quantification 4
1.4 Motivation 5

2 Uncertainty Quantification 6
2.1 Bayesian Statistical Analysis 6
2.1.1 Markov Chain Monte Carlo (MCMC) 8
2.1.2 Delayed Rejection Adaptive Metropolis (DRAM) 8
2.1.3 Uncertainty Propagation: Credible & Prediction Intervals 9

3 Viscoelasticity of Soft Elastomers: Integer Order Approach 11
3.1 Introduction 11
3.2 Experimental Setup 11
3.3 Theory 13
3.3.1 Finite Deformation Energy Relations 13
3.3.2 Nonlinear Viscoelastic Model 16
3.3.3 Linear Viscoelastic Model 17
3.3.4 Hyperelastic Energy Function 18
3.4 Uncertainty Analysis 19
3.4.1 Model Calibration: Linear Viscoelastic and Hyperelastic Parameters . 19
3.4.2 Model Calibration: Linear Viscoelastic Parameters 23
3.4.3 Model Prediction Procedure 24
3.4.4 Model Prediction: Linear Viscoelasticity 25
3.4.5 Model Calibration: Nonlinear Viscoelastic and Hyperelastic Parameters 27
3.4.6 Model Calibration: Nonlinear Viscoelastic Parameters 28
3.4.7 Model Prediction: Nonlinear Viscoelasticity 31
3.5 Conclusions 32

4 Viscoelasticity of Soft Elastomers: Fractional Order Approach 34
4.1 Introduction 34
4.2 Theory 35
4.2.1 Definitions of Fractional Derivatives 35
4.2.2 Finite Deformation Energy Formulation 36

4.2.3 Linear Viscoelastic Model for Fractal Media 37
4.2.4 Nonlinear Viscoelastic Model for Fractal Media 38
4.2.5 Internal State Variables and Fractional Derivative of Strain 40
4.2.6 Summary of Models and Parameters 40
4.3 Uncertainty Analysis 42
4.3.1 Model Calibration: Linear Viscoelasticity 43
4.3.2 Model Calibration: Nonlinear Viscoelasticity 45
4.3.3 Model Prediction Procedure 47
4.3.4 Model Prediction: Linear Viscoelasticity 49
4.3.5 Model Prediction: Nonlinear Viscoelasticity 51
4.4 Conclusions 51

5 Electromechanics of Soft Elastomers 55
5.1 Introduction 55
5.2 Experimental Setup 56
5.2.1 Transverse Load - Displacement 57
5.2.2 Electric Displacement - Electric Field 58
5.3 Theory 61
5.3.1 Transverse Load - Displacement 62
5.3.2 Electric Displacement - Electric Field 66
5.4 Uncertainty Analysis 67
5.4.1 Electromechanical Parameter Estimation 67
5.4.2 Rate-Dependent Dielectric Hysteresis 69
5.4.3 Case Studies 69
5.4.4 Case F1: Hyperelastic Parameter Estimation 71
5.4.5 Cases F2: Electrostrictive Parameter Estimation 75
5.4.6 Case F3(a-f): Electrostrictive Parameter Estimation - Field Analysis 75
5.4.7 Case D1: Rate-Dependent Dielectric Model 77
5.4.8 Case D2(a-c): Rate-Dependent Dielectric Model - Effect of Transverse Displacement 79
5.5 Concluding Remarks 80

6 Ferroelectric Domain Structure Evolution: Theory 83
6.1 Introduction 83
6.2 Density Functional Theory Calculations 84
6.3 Continuum Phase Field Model 88
6.4 Monodomain Structures 91
6.5 Polydomain Structures 92
6.5.1 Uniform Domain Regions 92
6.5.2 180° Domain Wall 93
6.6 Concluding Remarks 100

7 Ferroelectric Domain Structure Evolution: Uncertainty Analysis 102
7.1 Introduction . . . 102
7.2 Monodomain Structures . . . 102
7.2.1 Model Calibration: Energy . . . 102
7.2.2 Model Calibration: Stresses . . . 106
7.3 Polydomain Structures . . . 110
7.3.1 180° Domain Wall . . . 110
7.4 Concluding Remarks . . . 114

8 Concluding Remarks & Future Work 116
8.1 Publications & Proceedings . . . 117

Appendix

A Supplemental Material 120
A.1 Dempster-Shafer Theory of Evidence . . . 120
A.1.1 Rules of Combination . . . 123

References . . . 125

Biographical Sketch . . . 133

LIST OF TABLES

3.1 Integer Order Linear Viscoelastic: Model parameter means ($\bar{\theta}$) and standard deviations (σ_θ). Nominal value of hyperelastic parameters: $G_c = 7.55$ kPa, $\lambda_{max} = 4.83$, and $G_e = 17.7$ kPa. 23

3.2 Integer Order Linear Viscoelastic: Model error in units of kPa^2. Model evaluated using parameter distributions calibrated using the data specified in the first column. 27

3.3 Integer Order Nonlinear Viscoelastic: Model parameter means ($\bar{\theta}$) and standard deviations (σ_θ). Nominal value of hyperelastic parameters: $G_c = 4.47$ kPa, $\lambda_{max} = 5.47$, and $G_e = 2.77$ kPa. 29

3.4 Integer Order Nonlinear Viscoelastic: Model error in units of kPa^2 when using mean parameter value from calibration at single stretch rate. 32

4.1 Fractional Order Linear Viscoelastic: Model error (3.24) in units of kPa^2. Model evaluated using parameter distributions calibrated using the data specified in the first column. Mean value of parameter distributions is reported by $\bar{\theta}$. Nominal value of hyperelastic parameters: $G_c = 6.79$ kPa, $\lambda_{max} = 4.86$, and $G_e = 15.3$ kPa. 51

4.2 Fractional Order Nonlinear Viscoelastic: Model error in units of kPa^2. Model evaluated using parameter distributions calibrated using the data specified in the first column. Parameter statistics are given in Table 4.3. 53

4.3 Fractional Order Nonlinear Viscoelastic: Model parameter means ($\bar{\theta}$) and standard deviations (σ_θ). Nominal value of hyperelastic parameters: $G_c = 11.88$ kPa, $\lambda_{max} = 8.50$, and $G_e = 4.47$ kPa. 53

5.1 Calibration cases using transverse load-displacement data. 70

5.2 Calibration cases using data from Sawyer-Tower experiment. 71

5.3 Comparison of mean non-affine hyperelastic parameters from uni-axial model calibration [50] and current transverse membrane loading conditions. The units for G_c and G_e are in kPa, and λ_{max} is unitless. 74

5.4 Parameter statistics are provided in columns 3 (mean - $\bar{\kappa}_r$) and 4 (standard deviation - σ_{κ_r}). Columns 5-10 reflect the model error ($L_2 - norm$) in units of N^2. Error calculated based on model prediction for each voltage level. 78

6.1 Displacement boundary conditions for finite element model of 180° domain wall structure. 95

6.2 This table summarizes the energy contributions as calculated via (6.30) for each energy component for both finite element (FEA) and finite-difference (FD) approximations of the 180° domain wall structure. All units for energy are in mJ/m^2. 100

7.1 A summary of the continuum material parameters determined using Bayesian statistics and the MCMC/DRAM methods. 104

7.2 A summary of the continuum material parameters determined using Bayesian statistics and the MCMC/DRAM methods. The parameters with an asterisk were identified using $\theta_{\sigma 2}$. 108

LIST OF FIGURES

2.1 (a) Calibrated model parameters (θ_i) and observation errors (ϵ_i). (b) Example of $n\%$ credible and prediction intervals. 10

3.1 (a-c) Cyclic loading over 12 cycles and (d) decay of peak stress per cycle. The decay of the peak stress is normalized by the maximum stress when $\dot{\lambda} = 0.67$ Hz. Similar results are not shown for tests performed at 0.10 Hz and 0.50 Hz. . . . 12

3.2 Comparison of the viscoelastic behavior for the 12^{th} cycle for each stretch rate (Note: $\frac{d\lambda}{dt} = 6.7 \times 10^{-5}$ Hz was only run for one cycle, and the stretch $\lambda = 1$ has been adjusted by subtracting out viscoplastic strain from cyclic loading.) . 13

3.3 Parameter chains for calibration at slowest stretch rate with integer order, linear viscoelastic, and nonaffine hyperelastic models. 20

3.4 Marginal posterior densities for calibration at slowest stretch rate with integer order, linear viscoelastic, and nonaffine hyperelastic models. 21

3.5 Pairwise correlation between each sampled parameter for calibration at the slowest stretch rate using the integer order, linear viscoelastic, and nonaffine hyperelastic models. A nearly single-valued linear correlation is observed between several parameters. 22

3.6 Linear viscoelastic model response when predicting behavior at the same rate used to calibrate. Parameter uncertainty propagated through model to generate 95% prediction (PI) and credible (CI) intervals. (b) Highlights the scale of prediction and credible intervals. 24

3.7 Prediction of material behavior at nontrained boundary conditions using the integer order linear viscoelastic model. Model was calibrated using $\dot{\lambda} = 6.7 \times 10^{-5}$ Hz. Error measurements are given in Table 3.2. Results not shown for $\dot{\lambda} = 0.10$ and 0.50 Hz. Note that 95% prediction (PI) and credible (CI) intervals are not visible at this scale. 26

3.8 Parameter chains for calibration at slowest stretch rate with integer order, nonlinear viscoelastic, and nonaffine hyperelastic models. 28

3.9 Marginal posterior densities for calibration at slowest stretch rate with integer order, nonlinear viscoelastic, and nonaffine hyperelastic models. 29

3.10 Pairwise correlation between each sampled parameter for calibration at the slowest stretch rate using the integer order, nonlinear viscoelastic, and nonaffine hyperelastic models. A nearly single-valued linear correlation is observed between several parameters. 30

3.11 Nonlinear viscoelastic model response when predicting behavior at the same rate used to calibrate. Parameter uncertainty propagated through model to generate 95% prediction (PI) and credible (CI) intervals. Note that the 95% credible intervals are not visible at this scale. 31

3.12 Prediction of material behavior at nontrained boundary conditions using the integer order nonlinear viscoelastic model. Model was calibrated using $\dot{\lambda} = 0.67$ Hz. Error measurements are given in Table 3.4. Results not shown for $\dot{\lambda} = 0.10$ and 0.50 Hz. 33

4.1 Numerical agreement between internal state variable and fractional derivative of deformation 41

4.2 Parameter chains for calibration at slowest stretch rate with fractional order, linear viscoelastic model. The marginal posterior densities for each parameter appears to be stable. 44

4.3 Marginal posterior densities for calibration at slowest stretch rate with fractional order, linear viscoelastic model. 45

4.4 Pairwise correlation between each sampled parameter for calibration at the slowest stretch rate using the fractional order, linear viscoelastic model. A linear relationship is observed between several parameters. Every 200 sample points from chain taken for plotting. 46

4.5 Parameter chains from MCMC sampling of $\dot{\lambda} = 6.7 \times 10^{-5}$ Hz data set. All model parameters were considered for this calibration. 47

4.6 Chains from MCMC sampling of $\dot{\lambda} = 0.67$ Hz data set. Note hyperlastic parameters are set to nominal values. 48

4.7 Marginal posterior densities from MCMC sampling of the $\dot{\lambda} = 0.67$ Hz data set. Note hyperlastic parameters are set to nominal values. Every 100 sample points from the chain are taken for plotting. 48

4.8 Pairwise correlation from MCMC sampling of the $\dot{\lambda} = 0.67$ Hz data set. Note hyperlastic parameters are set to nominal values. Every 100 sample points from the chain are taken for plotting. 49

4.9 Prediction of material behavior at nontrained boundary conditions using the fractional order linear viscoelastic model. The model was calibrated using $\dot{\lambda} = 6.7\times10^{-5}$ Hz. Error measurements are given in Table 4.1. Results not shown for

$\dot{\lambda} = 0.0472, 0.10$ and 0.50 Hz. (b) Highlights 95% prediction (PI) and credible (CI) intervals. 50

4.10 Prediction of material behavior at nontrained boundary conditions using the fractional order nonlinear viscoelastic model. Model was calibrated using $\dot{\lambda} = 0.67$ Hz. Error measurements are given in Table 4.2. 52

5.1 (a) Elastomer is stretched over acrylonitrile butadiene styrene (ABS) plastic frame and electrically isolated for electrode application. (b) Top view of experimental setup. 58

5.2 Cross section illustration of the membrane structure. The structure is loaded along the surface of the center ring. The load is denoted by F and is applied in the transverse direction. Inhomogeneous deformation along l is neglected in the reduced-order model. 59

5.3 (a) Measured transverse load during complete experimental cycle under different applied fields. Additional data sets at 1 kV, 3 kV, and 5 kV are not shown for clarity. (b) Measured transverse load during *loading* of specimen. 59

5.4 Sawyer-Tower circuit with VHB in series with $C_0 = 153\ \mu F$. VHB specimen shown in non-deformed configuration. 60

5.5 Data collected from Sawyer-Tower circuit. (Left) Electric displacement plotted as a function of the nominal field and (Right) electric displacement as a function of index from a single loop. 60

5.6 (a) Slope of D-E hysteresis cycle has changed due to application of transverse load. (b) Negligible variations in slope are observed by adjusting the amount of pre-stretch. 61

5.7 Parameter chain obtained with 5×10^5 realizations of the non-affine hyperelastic model to demonstrate convergence. 72

5.8 Marginal posterior parameter densities for non-affine hyperelastic model at $E_i = 0kV$. Note the units for G_c and G_e are in kPa, and λ_{max} is unitless. . . . 72

5.9 Joint sample points of parameter chains. 73

5.10 Marginal posterior parameter density for the relative permittivity. Calibration performed using transverse load model and data for all voltages applied to membrane. 76

5.11 95% prediction (PI) and credible (CI) intervals for the transverse load data along with median model estimates. Data sets found in Figure 5.3 are included for comparison. (d) Highlights scale of prediction and credible intervals. Results not shown for applied voltages at 2 kV, 4 kV, and 5 kV. 77

5.12 Marginal posterior parameter densities for dielectric model. The densities are created using data from the D-E loops for case study D1. 78

5.13 95% credible and prediction intervals for the $D - E$ loops along with median model estimates. Data sets found in Figure 5.5 are included for comparison. Note the data has been plotted with respect to index to more clearly represent the 95% prediction (PI) and credible (CI) intervals. 79

5.14 Model underpredicts effects of electrostriction at higher fields when using parameters calibrated from electric displacement-electric field (DE) hysteresis cycles (Case D1). 80

5.15 Comparison of marginal posterior densities for the relative permittivity in the dielectric hysteresis model. These densities represent the distributions identified for case studies D2(a-c). It is clearly seen that the addition of transverse displacement significantly affects the calibrated density of κ_r. 81

6.1 (a) Atomic displacement showing the relationship between the position of the titanium atom in the x_2 and x_3 directions as the deformation component F_{23} varies between 0 and 0.17. (b) Relationship between the atomic position (titanium atom) and polarization in the x_3 direction as the deformation gradient component F_{23} varies between 0 and 0.17. 86

6.2 Polarization states at which energy and stress tensor were calculated. Six different polarization studies were performed. 87

6.3 Plots of (a) total energy and (b) shear stress (σ_{23}) as a function of P_2 and P_3. Lines are numbered for reference in later discussion. 88

6.4 Example of the electron density solutions for (a) the reference undeformed cubic structure and (b) shear deformed state where the unit cell has been sheared such that the deformation gradient component F_{23} is non-zero. 91

6.5 Polarization field in 180° domain wall structure. 94

6.6 Numerical solution for 180° domain wall polarization in the P_3-direction and the strain component, $\Delta\varepsilon_{11}$. Note, for a given set of parameters it took 26 time steps (TS) to meet convergence requirements. 99

6.7 Energy density over 180° domain wall. Results from finite-difference (FD) approach agree well with finite element (FEA) solution using a consistent set of parameters. 100

7.1 Parameter chains for calibration of phase field model parameters with respect to DFT energy measurements for monodomain structures. 103

7.2 Marginal posterior densities for calibration of phase field model parameters with respect to DFT energy measurements for monodomain structures. 104

7.3 Pairwise correlation between each sampled parameter for calibration of phase field model parameters with respect to DFT energy measurements for monodomain structures. A nearly single-valued linear correlation is observed between several parameters. 105

7.4 95% prediction (PI) and credible (CI) intervals for monondomain energy model. (a) Model comparison with all DFT calculations in 3D polarization space. (b,c) Two-dimensional representations of lines 1 and 4 with respect to polarization. 106

7.5 Marginal posterior densities for calibration of phase field model parameters with respect to DFT stress measurements for monodomain structures. The marginal posterior densities for the shear stress parameters are reduced if calibrated separately, as seen by the dashed lines. 109

7.6 Examples of the mean model estimates along with 95% prediction (PI) and credible (CI) intervals in relation to DFT stresses for (a) σ_{11} , (b) σ_{22}, (c) σ_{33} and (d) σ_{23}. Note that each plot consists of a set of stresses along different lines in the P_2P_3-plane. The lines have been numbered 1-6 for reference in later discussion. 111

7.7 Two-dimensional representations of the uncertainty propagation shown in Figure 7.6. Note, (c,d) presents a contrast to Figure 7.6 in that the 95% prediction and credible intervals were generated from propagating the uncertainty from the reduced parameter set θ_{σ_s}. 112

7.8 (a) Sampling chain of g_{44}. (b) Marginal posterior density generated using a Kernel Density Estimator (KDE). 113

7.9 Credible intervals for energy density model of 180° domain wall structure. . . 113

A.1 The shape of the belief structure must be refined for meaningful interprepation. The partitioning of the evidence must by done in such a manner that a convex belief structure (b) is generated. A structure without convex shape as seen in (a) does not allow for any meaningful statistical inference of the proposition. . 122

A.2 Venn diagram relationships describing two cases of belief and plausibility functions. In (a), the belief and plausibility functions lead to differences since not all b_i that intersect A are subsets of A. In (b), belief and plausibility functions are equal because all sets b_i intersect A and are subsets of A. These distinctions give additional statistical information that can be used in decision making which is not contained within probability theory. 123

A.3 Relationship between belief, plausibility, and uncertainty for a given proposition, A. The mass of uncertainty is evidence that could either support or conflict with A [28]. 123

ABSTRACT

Practically all engineering applications require knowledge of uncertainty. Accurately quantifying uncertainty within engineering problems supports model development, potentially leading to identification of key risk factors or cost reductions. Often the full problem requires modeling behavior of materials or structures from the quantum scale all the way up to the macroscopic scale. Predicting such behavior can be extremely complex, and uncertainty in modeling is often increased due to necessary assumptions. We plan to demonstrate the benefits of performing uncertainty analysis on engineering problems, specifically in the development of constitutive relations and structural analysis of smart materials and adaptive structures. This will be highlighted by a discussion of ferroelectric materials and their domain structure interaction, as well as dielectric elastomers' viscoelastic and electrostrictive properties.

CHAPTER 1

INTRODUCTION

Mechanical engineering covers a broad array of topics. Inherent in these areas is the need to accurately model and predict physical behavior. Many tools exist for model development and calibration; however, few offer the ability to quantify underlying uncertainty within the model as well as experimental measurements. Uncertainty analysis is often minimal or completely overlooked in the realm of material design. The uncertainty that exists in these types of problems can be clearly shown, and often the results of such analysis can provide guidance towards enhancing our understanding of material physics and structural engineering predictions. We propose to show the diverse range of applications in which uncertainty quantification techniques may be applied in the context of engineering mechanics, starting from constitutive modeling all the way up to structural modeling.

1.1 Dielectric Elastomers

Dielectric elastomers are a subset of materials known as active polymers, which are commonly used in adaptive structures. Active polymers provide unique capabilities for real time control of a structure's shape, stiffness, or damping [5, 74]. In such applications it is extremely important to have knowledge of the viscoelastic constitutive behavior, particularly in instances where actuator control or dynamic tunability is of critical importance. The actuation mechanism is different depending on which type of polymer is considered. In the case of dielectric elastomers, the material deforms proportionally to the square of the applied field. This type of behavior is typically called electrostriction. The material deforms as a result of competing mechanisms between the solid material's elasticity and the attractive Lorentz forces that exist due to the applied field. The membrane is compressed in the direction of the applied field due to the electrostatic stress generated by the unlike charges.

This stress leads to contraction of the membrane parallel to the field and expansion in the perpendicular directions.

A good description of the dielectric elastomer and electrodes is given by a parallel plate capacitor. The distance between the plates is filled by the elastomer, but as a result of increased electrostatic forces, the distance between the two plates reduces. Due to the near incompressible nature of the material, the capacitance of the membrane is directly related to the square of the planar area, making these materials a viable form of a pressure sensor [22,60]. As opposed to many other smart materials, dielectric elastomers can be used for mechanical work without large power supplies or magnetic coils. Due to their light weight and intrinsic material properties, active polymers have begun to serve as viable options for artificial muscles [5].

Dielectric elastomers are a part of a broad range of materials used in a variety of applications. Several specific areas in which dielectric elastomers have been or could be potentially applied include robotics [36, 61, 62], optical switches and speakers [3, 57], and prosthetic pumps [24]. These materials provide a unique combination of being able to withstand large deformation while being lightweight. Furthermore, these materials can be controlled by varying the application of electric field across the membrane. This make these materials ideally suitable for applications in robotic structures where they are used to emulate artificial muscle. Often these elastomers operate over a broad range of deformation rates, experiencing complex viscoelastic behavior [17, 70]. Therefore, knowledge of the viscoelastic constitutive behavior is critically important. Developing a model that accounts for this broad range of time scales is non-trivial, and uncertainty analysis provides insight into understanding and characterizing this complex behavior. Very High Bond (VHB) 4910, made by 3M, is a dielectric elastomer and previous research has shown the effectiveness of a non-linear viscoelastic model in capturing the behavior of VHB 4910 [50], but robust predictions for the material behavior over a large range of deformation rates is still an open challenge. In Chapter 3 we present the results from modeling the viscoelastic behavior using integer order calculus operations. An alternative approach is presented in Chapter 4 which highlights the potential usefulness of using fractional order calculus operations to predict a material's viscoelastic response.

Understanding material constitutive behavior does not completely characterize a problem. Often, the material is implemented on a structure where it works with other materials as a system or device. Structural modeling must also be understood in order to better characterize and quantify the uncertainty in these engineering systems and devices. For example dielectric elastomers are often implemented on robotic platforms. Using Bayesian statistical methods, we considered the behavior of the dielectric elastomer VHB 4910 when bi-axially pre-stretched and exposed to transverse loading as well as different electrostatic fields [49]. The preliminary results for this research are presented in Chapter 5. On-going research is focused on a solution that completely characterizes the electromechanical behavior over the range of testing conditions.

1.2 Ferroelectric Materials

Ferroelectricity defines a class of materials that respond mechanically to the presence of an electric field and conversely can generate charge when stressed. Within an unpoled ferroelectric material there are many regions of randomly aligned dipoles, yet the macroscopic polarization is zero [42]. Upon application of an electric field these dipoles can be oriented to partially align with the applied electric field. Furthermore, after the applied electric field is reduced to zero, the material maintains a finite polarization. This ability to control the electronic structure makes ferroelectrics prevalent in sensor and actuator applications [74]. One common application is in capacitors where the nonlinear ferroelectric properties allow for capacitance tuning.

A piezoelectric material differs from ordinary solids in that upon application of stress, there is a proportional strain and also the creation of electric charge. Furthermore, this effect works in both directions, so the application of an electric field yields a corresponding change in strain and stress. Piezoelectric ceramics typically have dielectric constants on the order of several hundred to several thousand [35]. A similar phenomenon occurs in pyroelectric materials where an electric charge is developed as a result of uniform heating. Note, that the unique aspect of pyroelectrics is that a charge is developed as a result of *uniform* heating, as any piezolectric crystal will develop charge in the presence of non-uniform heating. All ferroelectric materials have the properties of a piezoelectric and pyroelectric solid, but with the additional ability to reverse their polarization in the presence of an electric field.

Ferroelectric materials are well established in engineering applications, including energy harvesting [77], structural health monitoring [58], flow-control [7, 9, 39], transportation [53], and robotic structures [30, 64, 83, 84]. Further discussion related to the various applications in which ferroelectric materials are an active component can be found in [12,41,74,76,79–81]. Accurately predicting the constitutive behavior of these materials from the atomic scale all the way up to a macroscopic continuum is important in light of their impact in active structures and systems. Several methods exist to predict the material behavior at one particular scale, but many methods become inaccurate at higher length scales where homogenization produces loss of information. We propose to analyze the domain structure characteristics predicted from density functional theory (DFT) calculations versus a continuum phase field model. This analysis will assess uncertainty by quantifying the input model parameter probabilities using Bayesian statistical methods. The theoretical framework for this study is outlined in Chapter 6 and the uncertainty analysis is presented in Chapter 7.

1.3 Uncertainty Quantification

Depending on the problem being considered or the quantity of interest (QoI), different uncertainty quantification techniques are more appropriate than others. Often uncertainty in the input is known (or attainable), and the resulting uncertainty in the model output is of interest. This is especially important in the design process. Understanding the relationship between model input uncertainty and model output can drastically affect the design choice. This type of analysis is typically done for models that are amenable to Monte Carlo sampling (i.e., many evaluations can be taken in a short amount of time). The forward model approach of simply propagating uncertainty though the model allows tuning of input parameter uncertainty to achieve the desired output. This is especially important in engineering applications where input uncertainty is often directly correlated with costs. Decreasing the uncertainty in the input parameters typically requires increased costs, which is especially relevant with regard to manufacturing methods. Decreasing the tolerance on dimensions, surface properties, etc., can be expensive. Finding the optimal input to decrease costs but achieve the desired output is an important problem. Of course most models have many input parameters, which makes solving these problems non-trivial. This highlights the importance of combining sensitivity analysis along with uncertainty quantification. As opposed to this forward model approach, one can, alternatively, consider the case of inverse problems.

For problems in which experimental data or high-fidelity simulations exist, one can attempt to identify uncertainty in the model input parameters based on the model output. This constitutes a class of inverse problems in which input parameters are assumed uncertain (stochastic variables) and their underlying distributions (posterior densities) are ascertained through a sampling technique. We propose to employ a Markov Chain Monte Carlo (MCMC) algorithm, coupled with the delayed rejection adaptive Metropolis (DRAM) sampling technique, in order to quantify uncertainty in the model parameters [26, 27]. This approach employs Bayesian statistical analysis, which will be discussed in more detail in Chapter 2.

1.4 Motivation

The goal of this research is to apply uncertainty quantification techniques to smart material and adaptive structure engineering problems to gain insight into model limitations and enhance model prediction in light of limited information. Furthermore, applying these principles during the design process enhances our understanding of the material physics, especially with regard to characterization. Calculating the uncertainty and propagating it through a model allows us to see the effect of lack of knowledge or random error on the system. The advantage of this approach is that we are given more realistic bounds on the limits of our model and can use this information to refine our methods to potentially improve predictions over broader operating regimes.

CHAPTER 2

UNCERTAINTY QUANTIFICATION

2.1 Bayesian Statistical Analysis

When considering the value of unknown model parameters, there are several approaches for parameter estimation. Determining model parameters in light of data or high-fidelity simulations is called model calibration. Oftentimes these parameters are considered to be deterministic and are found by performing a basic curve fitting algorithm. Bayesian model calibration employs a different approach to parameter calibration, acknowledging the existence of uncertainty due to model discrepancies and observation errors associated with data. By using this Bayesian approach and taking the parameters to be stochastic variables instead of fixed values, one can quantify the inherent uncertainty attributed to such parameters in light of data or higher fidelity models.

Because model parameters are found using data, this is what is called an *inverse problem*. As such, it is important to test the results of the model against untrained boundary conditions. In other words, the model may agree well with the data used to calibrate the parameters because by definition those parameters were found such that they fit that particular data. Therefore, the true strength of the model is best considered in light of model *prediction*, how well does the model predict the quantity of interest for different data sets.

Based on the quantity of interest, a statistical model is employed

$$M^{data}(i) = M(i;\theta) + \epsilon_i, \quad i = 1, ..., N \tag{2.1}$$

where $M^{data}(i)$ and ϵ_i are random variables denoting the i^{th} experimental data point and associated observation error, respectively. The parameter-dependent model response is given by $M(i;\theta)$, where θ denotes the unknown parameters. Essentially, we expect the data to be distributed about the model response within some random noise defined by ϵ_i. These observation errors constitute measurement errors inherent in measurement devices, variability between test specimens, and also model discrepancies due to limitations in physical models. The statistical model assumes that the observation errors are independent and identically distributed (iid).

To determine the parameter distributions, Bayesian model calibration uses Bayes' relation

$$\pi(\theta|M^{data}) = \frac{p(M|\theta)\pi_0(\theta)}{\int_{\mathbb{R}_p} p(M|\theta)\pi_0(\theta)d\theta} \tag{2.2}$$

where $\pi(\theta|M^{data})$ is called the posterior density. The posterior density quantifies the probability of observing parameter values θ given the data M^{data}. Bayes' relation comes directly from the formal definitions of conditional probability and the product rule of probability. The relation incorporates *a priori* knowledge about the parameters in the prior density, $\pi_0(\theta)$. The prior is updated by using the likelihood $p(M|\theta)$, which incorporates information provided by the model and data. The denominator normalizes the posterior density to have an area of unity.

One must be careful in initializing the prior density in order not to bias the posterior. Often model parameters have some physical constraints (e.g., positivity, $\in [0, \infty]$, etc.). To ensure noninformative priors, a uniform distribution across the feasible parameter space is often assumed. The other part of Bayes' relation that we must consider is the likelihood function. In order to construct the likelihood function, assumptions must be made about the observation errors, ϵ_i. It is assumed that the observation errors are independent and identically distributed (iid) and $\epsilon_i \sim N(0, \sigma^2)$, yielding a Gaussian likelihood

$$p(M|\theta) = e^{-\sum_{i=1}^{N}[M^{data}(i) - M(i;\theta)]/(2\sigma^2)}. \tag{2.3}$$

This corresponds with the fact that the observed data is independent and normally distributed with $M^{data}(i) \sim N(M(i;\theta), \sigma^2)$, which comes from (2.1). Note that the variance, σ^2, can be inferred with the other calibration parameters, θ. The variance estimates the error in observations, which for some experiments may be known (although that is not often the case). Using the statistical model we must now employ a sampling method to develop the posterior densities.

2.1.1 Markov Chain Monte Carlo (MCMC)

For a moderate number of parameters, p, one can employ a sparse grid quadrature technique; however, for larger p, Monte Carlo integration techniques are required. Pure Monte Carlo presents some difficulties, so the alternative approach used here is the Markov Chain Monte Carlo (MCMC) method. When sampling it is important to use a method that will adequately explore the sample space. By constructing a Markov chain whose stationary distribution is the posterior density, we can ensure that the geometry of the distribution is adequately explored [75]. In addition to exploring the sample space, the problem is complicated by the fact that model parameters are often correlated. The MCMC method accomodates the potential correlative nature of the problem, making it an ideal choice for engineering analysis.

2.1.2 Delayed Rejection Adaptive Metropolis (DRAM)

As part of our sampling routine, we will also employ the delayed rejection adaptive Metropolis (DRAM) algorithm [26, 27]. The combination of delayed rejection (DR) and adaptive metropolis (AM) provides complementary mechanisms for updating the parameter values [75]. The Metropolis algorithm accepts chain candidates, θ_{new}, based on

$$\alpha(\theta_{new}|\theta_{old}) = \min(1, \frac{p(M|\theta_{new})}{p(M|\theta_{old})}). \tag{2.4}$$

This essentially says that the new chain value is accepted with probability α, where α is the minimum between 1 and the ratio of the likelihood functions. From (2.3) we see that the ratio in likelihoods will be less than 1 when the new chain value increases the error measure compared to the current chain value. So, AM says that the new chain candidate is automatically accepted if it reduces the error, and accepted with some probability α if the error is increased. Furthermore, the probability of acceptance is directly correlated with the amount of error difference between the new and current chain candidates. If the new candidate is rejected, then the process is continued with the current candidate. When sampling it is important to have a good mixture of values. So, if when using AM the new candidate is consistently rejected, then you may not achieve good mixing. To improve mixing, delayed rejection (DR) is added to the algorithm. Simply put, DR constructs an alternative chain candidate for testing instead of just keeping the original chain. The alternative candidate is then put through the AM routine. The nuances of the mathematical approach can be found in [26, 27, 75], but with this framework for Bayesian methods in mind, we will demonstrate its application in several engineering problems.

2.1.3 Uncertainty Propagation: Credible & Prediction Intervals

Once the uncertainty associated with the input variables has been quantified, it is then useful to consider how that uncertainty propagates through the model and affects the quantities of interest. We will demonstrate the use of two types of uncertainty propagation. First, we will discuss the generation and interpretation of credible intervals. This will be followed by a description of prediction intervals.

A $100 \times (1-\alpha)\%$ credible interval is defined to be the interval with probability $1-\alpha$ of containing the quantity of interest. Credible intervals represent the result of propagating the parameter uncertainty through the model. This type of interval is generated by sampling a statistically significant amount of times from the parameter posterior densities (θ_i) and evaluating the model response for each sample set. The model realizations are put in ascending order from which one can generate intervals of credibility. The other type of interval we consider is called a prediction interval. The difference between credible and prediction intervals is that when predicting we also include the estimate for the observation errors (ϵ_i). This highlights the different components of uncertainty. If your observations errors are Gaussian, then you should find that $n\%$ of your data points are within the $n\%$ prediction interval. A detailed description of both credible and prediction intervals can be found in [75]. An example of input uncertainty is shown in Figure 2.1(a) and the resulting prediction and credible intervals are shown in Figure 2.1(b).

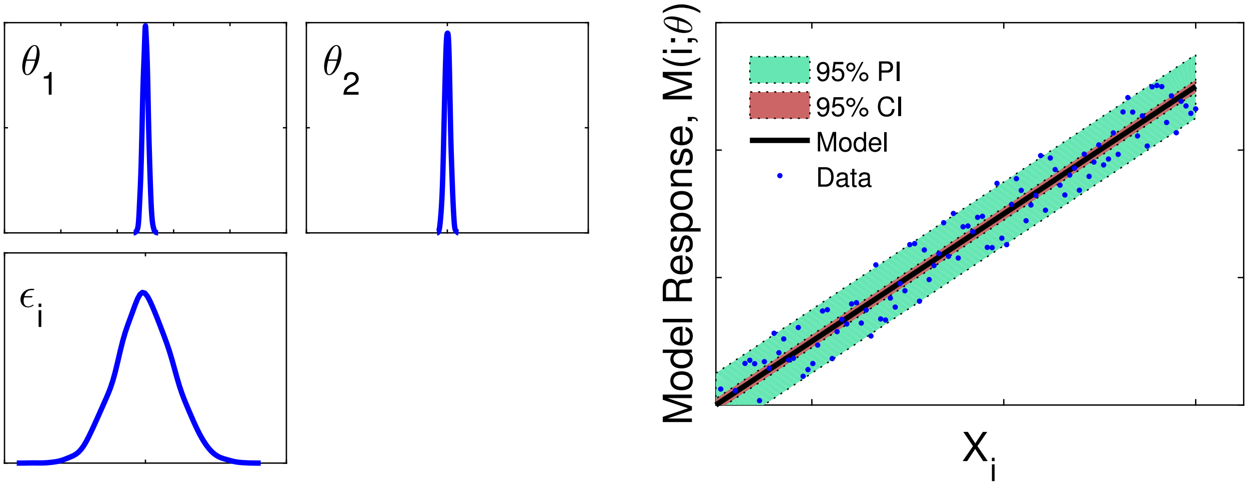

(a) Observed input uncertainty (b) Propagated output uncertainty

Figure 2.1: (a) Calibrated model parameters (θ_i) and observation errors (ϵ_i). (b) Example of $n\%$ credible and prediction intervals.

CHAPTER 3

VISCOELASTICITY OF SOFT ELASTOMERS: INTEGER ORDER APPROACH

3.1 Introduction

Viscoelasticity is pervasive in materials when they are subjected to different deformation rates. This means that stress exhibited by the material has an elastic component as well as a viscous component. In engineering applications this can be very useful as the viscous nature of the response yields a damping effect to the motion, where the excess energy is released as heat from the material [40]. The nature of this viscoelastic response is often quite complicated with characteristics that vary many orders of magnitude as a function of the deformation rates. This phenomenon has been studied extensively [6, 13, 17, 29, 31, 73]; however, accurately quantifying and predicting rate-dependent, finite deformation over a broad range of deformation rates continues to pose a significant challenge.

3.2 Experimental Setup

The experimental research focused on a series of uniaxial load measurments of the dielectric elastomer Very High Bond (VHB) 4910, made by 3M[1]. The specimens of VHB 4910 were cut and measured by hand, and then tested using an MTS Insight 1 kN load frame and 5 N load cell. The separation between the MTS clamps was initially 30 mm. The specimen was stretched at a constant rate until the MTS clamps were separated by 180 mm, meaning the specimen was stretched to approximately six times its initial length. Once maximum extension was achieved, the specimen was relaxed back to the initial grip separation distance at

---

[1] The experimental data collection for this project was performed by Dr. Michael Hays and Paul Miles as part of a research experience for undergraduates (REU) hosted by Florida State University and sponsored by the National Science Foundation (NSF).

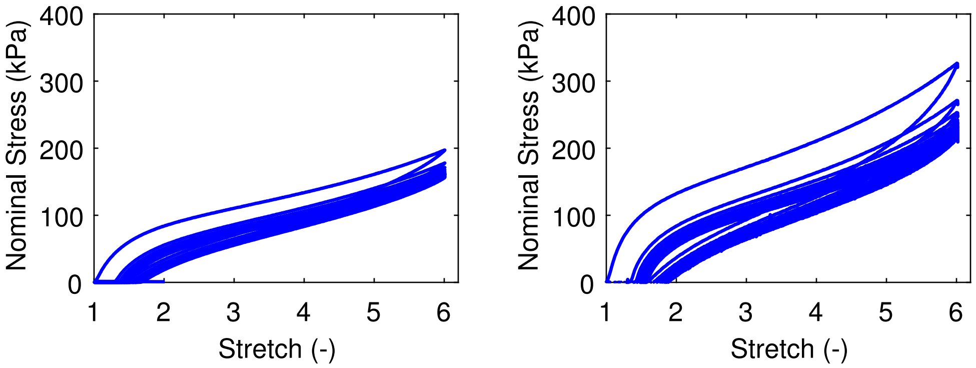

(a) $\frac{d\lambda}{dt} = 0.0472$ Hz (b) $\frac{d\lambda}{dt} = 0.335$ Hz

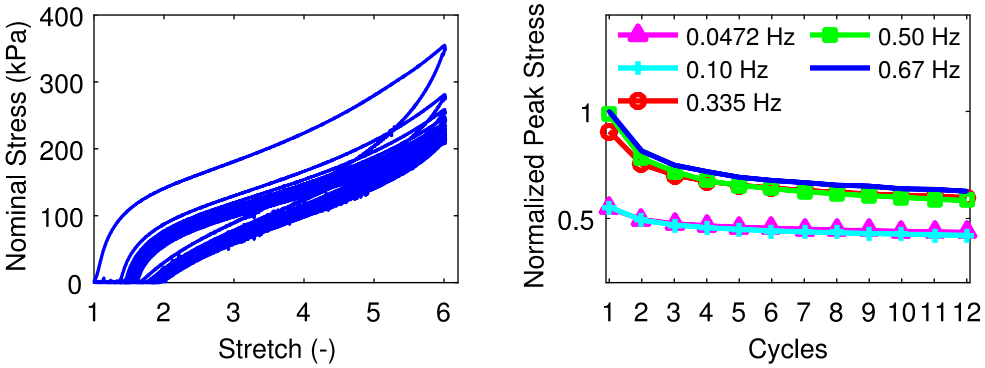

(c) $\frac{d\lambda}{dt} = 0.67$ Hz (d) Peak stress decay

Figure 3.1: (a-c) Cyclic loading over 12 cycles and (d) decay of peak stress per cycle. The decay of the peak stress is normalized by the maximum stress when $\dot{\lambda} = 0.67$ Hz. Similar results are not shown for tests performed at 0.10 Hz and 0.50 Hz.

the same speed. A cyclic loading was applied to each specimen until a steady-state hysteresis was reached as seen in Figure 3.1(a-c). In general 12 cycles was found to be sufficient to reach a steady-state hysteresis curve, which we have highlighted by showing the asymptotic behavior of the peak stresses per cycle in Figure 3.1(d). A range of deformation rates were tested, spanning four orders of magnitude. As seen in Figure 3.2, the rate of loading significantly affected the stress response. The hysteresis in the data highlights the viscoelastic nature of the material, and makes this data useful for calibrating model parameters as will be discussed in Section 3.4.

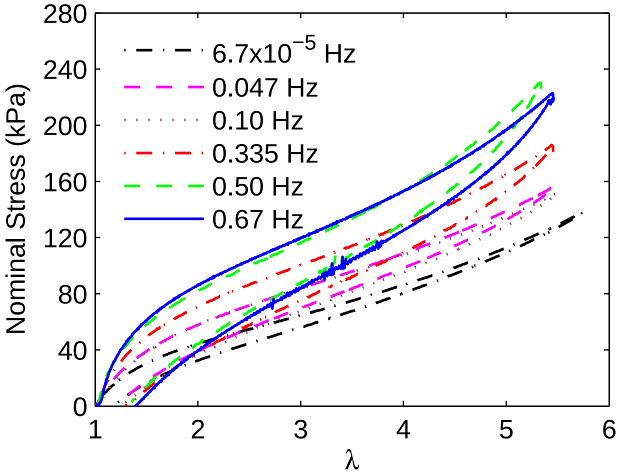

Figure 3.2: Comparison of the viscoelastic behavior for the 12^{th} cycle for each stretch rate (Note: $\frac{d\lambda}{dt} = 6.7 \times 10^{-5}$ Hz was only run for one cycle, and the stretch $\lambda = 1$ has been adjusted by subtracting out viscoplastic strain from cyclic loading.)

3.3 Theory

We summarize the hyperelastic and viscoelastic governing equations in this section. Internal variables associated with rate-dependent dissipation are developed following the general thermodynamic framework outlined in [14, 33, 63]. The origins of the dissipative equation governing internal loss is based on an unknown function of entropy generation derived from the second law of thermodynamics. This relationship is highlighted to provide guidance to the integration of the hyperelastic energy functions and coupling with viscoelastic dissipative energy functions. Through this approach, we develop linear and nonlinear forms of the viscoelastic stress and analyze its uncertainty using Baysian statistics in Section 3.4.

3.3.1 Finite Deformation Energy Relations

The following thermodynamic framework starts with the inclusion of thermal effects, but will later focus on model validation under the assumption of isothermal deformation. The total energy density function including non-conservative order parameters is given by

$$\psi = \psi_{\infty}(F_{iK}, \Theta) + \Upsilon(F_{iK}, \Theta, \Gamma^{\nu}_{iK}) \tag{3.1}$$

per reference volume where ψ_∞ is the conserved, hyperelastic free energy function and Υ is a dissipative energy function. The hyperelastic free energy is a function of the deformation gradient F_{iK} and temperature Θ while Υ includes Γ^ν_{iK}, which are a set of internal variables ($\alpha = 1, \ldots, n$ non-measurable internal states) that contribute to dissipation during rate dependent deformation.

Since elastomers typically undergo incompressible deformation, a penalty term is added to the free energy, so that the total free energy density is

$$\hat{\psi} = \psi - p(J-1), \tag{3.2}$$

where p is the unknown Lagrange multiplier, which represents a hydrostatic stress and $J = \det(F_{iK})$. Incompressible deformation is thus described by $J = 1$.

It will be shown that the work conjugate variable to the deformation gradient is the nominal stress

$$s_{iK} = \frac{\partial \hat{\psi}}{\partial F_{iK}} = \frac{\partial \psi_\infty}{\partial F_{iK}} - pJH_{iK} + \frac{\partial \Upsilon}{\partial F_{iK}}, \tag{3.3}$$

where we have used the identity $\dfrac{\partial J}{\partial F_{iK}} = JH_{iK}$ and $H_{iK}F_{jK} = \delta_{ij}$ [32].

The work conjugate variable for Γ^ν_{iK} is

$$Q^\nu_{iK} = -\frac{\partial \hat{\psi}}{\partial \Gamma^\nu_{iK}} = -\frac{\partial \Upsilon}{\partial \Gamma^\nu_{iK}} \tag{3.4}$$

where Q^ν_{iK} denotes the viscoelastic stress [33].

The origin of the work conjugate stress s_{iK} and viscoelastic stress Q_{iK} are determined by combining the first and second laws of thermodynamics. We briefly summarize the thermodynamic framework given by Peng et al. [63] and Holzapfel and Simo [33] and extend the results by considering differences in linear versus nonlinear viscoelasticity using uncertainty analysis.

The first law is written as a balance between the stored energy rate and applied thermomechanical power,

$$\rho^0 \dot{\Sigma} = s_{iK}\dot{F}_{iK} + \rho^0 r - Q_{I,I}, \tag{3.5}$$

where ρ^0 is the mass per undeformed volume, $\dot{\Sigma}$ is the stored energy rate, r is heat generation, and $Q_{I,I} = \dfrac{\partial Q_I}{\partial X_I}$ is divergence of heat flow in the Lagrangian frame. Introducing the Legendre transformation, $\hat{\psi} = \Sigma - S\Theta$, where S is the entropy per mass and Θ is temperature, we obtain

$$\rho^0 \dot{\hat{\psi}} = s_{iK}\dot{F}_{iK} + \rho^0 r - Q_{I,I} - \rho^0 \Theta \dot{S} - \rho^0 S \dot{\Theta}. \tag{3.6}$$

This form of the first law is combined with the second law, given here in the Lagrangian frame as

$$\rho^0 \dot{S} \geq \frac{\rho^0 r}{\Theta} - \frac{1}{\rho^0}\left(\frac{Q_I}{\Theta}\right)_{,I}. \tag{3.7}$$

Prior to combining (3.6) and (3.7), we take the time derivative of the total energy function $\hat{\psi}$,

$$\dot{\hat{\psi}} = \frac{\partial \hat{\psi}}{\partial F_{iK}}\dot{F}_{iK} + \frac{\partial \hat{\psi}}{\partial \Theta}\dot{\Theta} + \frac{\partial \hat{\psi}}{\partial \Gamma^{\nu}_{iK}}\dot{\Gamma}^{\nu}_{iK}, \tag{3.8}$$

based upon the state variables given in (3.1). A substitution of this relation into the first and second law equations (3.6) and (3.7) yields

$$\left(s_{iK} - \frac{\partial \hat{\psi}}{\partial F_{iK}}\right)\dot{F}_{iK} - \rho^0\left(S + \frac{\partial \hat{\psi}}{\partial \Theta}\right)\dot{\Theta} - \frac{\partial \hat{\psi}}{\partial \Gamma^{\nu}_{iK}}\dot{\Gamma}^{\nu}_{iK} - \frac{Q_I \Theta_{,I}}{\Theta^2} \geq 0, \tag{3.9}$$

which confirms the work conjugate relation in (3.3). The third term gives the viscoelastic stress from (3.4). The additional work conjugate relation on entropy is $S = -\dfrac{\partial \hat{\psi}}{\partial \Theta}$. The second law then requires that

$$-\frac{\partial \hat{\psi}}{\partial \Gamma^{\nu}_{iK}}\dot{\Gamma}^{\nu}_{iK} - \frac{Q_I \Theta_{,I}}{\Theta^2} \geq 0. \tag{3.10}$$

These two terms describe the entropy production. The second relation is normally restricted to be positive definite by allowing the heat flux to be $Q_I = -\kappa_{IJ}\Theta_{,J}$ where the thermal conductivity tensor (κ_{IJ}) is positive definite. In cases where the thermal gradients are negligible but viscoelastic effects are present, the first term on the right hand side must be positive definite.

We assume that thermal gradients are negligible and the viscoelasticity is the only source of entropy production. Following Peng et al. [63], we assume entropy production is a function of the time rate of change of the internal state variable and the deformation gradient,

$$-\frac{\partial\hat{\psi}}{\partial\Gamma^{\nu}_{iK}}\dot{\Gamma}^{\nu}_{iK} = Q^{\nu}_{iK}\dot{\Gamma}^{\nu}_{iK} = F(\dot{\Gamma}^{\nu}_{iK}, F_{iK}) \geq 0, \tag{3.11}$$

where both the viscoelastic stress from (3.4) and the entropy production function $F(\dot{\Gamma}^{\nu}_{iK}, F_{iK})$ are unknown. We assume the entropy production can be approximated by a Taylor expansion of the form

$$F(\dot{\Gamma}^{\nu}_{iK}, F_{iK}) = \eta^{\nu}\dot{\Gamma}^{\nu}_{iK}\dot{\Gamma}^{\nu}_{jL} + \cdots, \tag{3.12}$$

where η^{ν} must be positive definite to satisfy the second law. By assuming relative small rates of change of the internal state, we neglect any higher order terms in (3.12) and substitute this relation into (3.11) to obtain the equation

$$\eta^{\nu}\dot{\Gamma}^{\nu}_{iK}\dot{\Gamma}^{\nu}_{iK} - Q_{iK}\dot{\Gamma}^{\nu}_{iK} = 0 \rightarrow Q^{\nu}_{iK} = \eta^{\nu}\dot{\Gamma}^{\nu}_{iK}. \tag{3.13}$$

This is a generalized viscoelastic constitutive law analogous to a spring-dashpot model in one dimension [32]; however, it is important to note that this does not necessarily mean that the viscoelastic behavior is linear. It only states that the rate of change of the internal state is linearly proportional to the viscous stress. The dissipative function, Υ, may be nonlinear which will give rise to different viscoelastic stresses according to (3.4). We elaborate on these differences in the following paragraphs.

3.3.2 Nonlinear Viscoelastic Model

We must now specify how $\hat{\psi}$ may depend on Γ^{ν}_{iK}. We first consider the more general case of a nonlinear viscoelasticity model by defining a nonlinear dissipative energy, $\Upsilon_{NL} = \Upsilon$. We assume that the dissipative energy function is proportional to the hyperelastic function so that $\Upsilon \propto \sum_{\alpha} \beta^{\nu}_{\infty}\psi_{\infty}$. The proper form that satisfies the governing equations is [33]

$$\Upsilon_{NL} = \sum_{\alpha}\left[\frac{1}{2}\gamma_{\alpha}\Gamma^{\nu}_{iK}\Gamma^{\nu}_{iK} - \beta^{\nu}_{\infty}\frac{\partial\psi_{\infty}}{\partial F_{iK}}\Gamma^{\nu}_{iK} + \beta^{\nu}_{\infty}\psi_{\infty}\right] \tag{3.14}$$

where β^{ν}_{∞} is an unknown set of parameters for each α and γ^{ν} is a set of parameters that are proportional to the viscosity of the polymer network. It will be shown that the linear viscoelastic model follows directly from this equation if ψ_{∞} is a quadratic function of the difference between the internal state and the deformation gradient. For the nonlinear case, the total nominal stress can be determined from (3.3). Solution of the stress also requires solving the entropy production equation since Γ^{ν}_{iK} must be known. From (3.13), we must solve

$$\eta^{\nu}\dot{\Gamma}^{\nu}_{iK} + \frac{\partial \Upsilon_{NL}}{\partial \Gamma^{\nu}_{iK}} = 0 \tag{3.15}$$

where we have used the work conjugate relation for the viscoelastic stress (3.4).

3.3.3 Linear Viscoelastic Model

If linear viscoelasticity is assumed ($\Upsilon_L = \Upsilon$), the quadratic dissipative function

$$\Upsilon_L = \sum_{\alpha}\left[\frac{1}{2}\gamma^{\nu}\left(F_{iK} - \Gamma^{\nu}_{iK}\right)\left(F_{iK} - \Gamma^{\nu}_{iK}\right)\right] \tag{3.16}$$

is implemented. This version of the viscoelastic dissipation function can be directly related to the nonlinear viscoelastic model if $\psi_{\infty} = \sum_{\alpha} \frac{\gamma^{\nu}}{\beta^{\nu}_{\infty}} F_{iK}F_{iK}$. This illustrates that finite deformation, linear viscoelasticity requires implementing a dissipation function that is analogous to the neo-Hookean hyperelastic energy function. It will be shown that if the stretch is significant such that the neo-Hookean model breaks down, the viscoelastic behavior is less accurately modeled using the neo-Hookean viscous proportionality.

Implementation of the linear viscoelastic model for comparison to the nonlinear model requires modifying (3.15) by substitution of Υ_L instead of Υ_{NL} to solve for the internal state using

$$\eta^{\nu}\dot{\Gamma}^{\nu}_{iK} + \gamma^{\nu}\Gamma^{\nu}_{iK} = \gamma^{\nu}F_{iK}. \tag{3.17}$$

It is often preferable to re-write this equation in terms of the viscoelastic stress given by (3.4). A substitution of this stress into (3.15) and taking the time derivative of the entire equation leads to

$$\dot{Q}^{\nu}_{iK} + \frac{1}{\tau^{\nu}}Q^{\nu}_{iK} = \gamma^{\nu}\dot{F}_{iK} \tag{3.18}$$

where $\tau^{\nu} = \frac{\eta^{\nu}}{\gamma^{\nu}}$. This linear viscoelastic stress equation will be coupled with the calculation of the hyperelastic stress in (3.3) which results in the total stress

$$s_{iK} = \frac{\partial \psi_{\infty}}{\partial F_{iK}} - pJH_{iK} + \sum_{\alpha} Q^{\nu}_{iK} \tag{3.19}$$

since in the linear viscoelastic model we have $Q^{\nu}_{iK} = \dfrac{\partial \Upsilon}{\partial F_{iK}} = -\dfrac{\partial \Upsilon}{\partial \Gamma^{\nu}_{iK}}$.

In summary, the nonlinear viscoelastic model requires solving (3.3) and (3.15) where $\Upsilon \rightarrow \Upsilon_{NL}$. In the linear viscoelastic model, the total stress requires solving (3.19) together with (3.18). Solution of these equations requires specifying a hyperelastic energy function. In the following subsection, we introduce the Ogden and nonaffine hyperelasticity functions (ψ_{∞}) to complete the set of relations required to quantify rate-dependent stresses.

3.3.4 Hyperelastic Energy Function

Two hyperelastic energy functions are introduced for integration into the viscoelastic model and its coupling with the dissipative energy functions given by (3.14) and (3.16). First, the Ogden hyperelastic model is considered. It is written in terms of the principal stretches λ_i for the principal directions $i = 1$ to 3. This hyperelastic energy is

$$\psi^{O}_{\infty} = \sum_{d=1}^{3} \frac{\mu_d}{\alpha_d} \left(\lambda_1^{\alpha_d} + \lambda_2^{\alpha_d} + \lambda_3^{\alpha_d} - 3\right) \tag{3.20}$$

where μ_d are shear moduli with the effective shear modulus, $\mu = \sum_{d=1}^{3} \mu_d$, and α_d are unitless constants [32]. The model is physically constrained so that $\sum_{d=1}^{3} \mu_d \alpha_d \geq 0$.

In comparison, the nonaffine model combines the effect of a crosslinked network with entanglement effects described by the free energy [15]

$$\psi^{N}_{\infty} = \frac{1}{6} G_c I_1 - G_c \lambda_{max}^2 \ln(3\lambda_{max}^2 - I_1) + G_e \sum_{j} (\lambda_j + \frac{1}{\lambda_j}) \tag{3.21}$$

where G_c is the crosslink network modulus, G_e is the plateau modulus, λ_{max} is the maximum stretch of the effective affine tube, and $I_1 = \lambda_i \lambda_i$ is the first stretch invariant where summation on i is implied.

A comparison of the Ogden and nonaffine models revealed that predictions for hyperelastic stress were similar for both approaches. As the nonaffine model contains fewer parameters and is less phenomenological, the uncertainty analysis will focus on coupling the nonaffine hyperelastic model with the linear and nonlinear viscoelastic models. Further discussion on the reasoning behind this decision can be found in [50].

3.4 Uncertainty Analysis

The uncertainty analysis of the integer order viscoelastic models was guided by the following objectives:

1) Quantify the relative accuracy of the linear and nonlinear viscoelastic models in conjunction with the nonaffine hyperelastic model by comparing error measurements with respect to experimental data. Use Bayesian statistical analysis to quantify uncertainty associated with parameters and discuss the extent to which parameters can be uniquely identified. Determine degree to which each model can be simplified. Fixing hyperelastic parameters at values determined at the slowest rate is motivated based on model restrictions discussed in Section 3.3.
2) Identify viscoelastic parameter distributions associated with each experimental stretch rate.
3) Test predictive capability of each viscoelastic model. Models calibrated with one set of data must always be tested to see how well they predict other sets or types of data. Each set of parameters calibrated at a particular experimental rate will be used to predict the behavior at all the other rates.

We will address these objectives with regard to the linear viscoelastic model in Sections 3.4.1-3.4.4. Similar discussion for the nonlinear model is provided in Sections 3.4.5-3.4.7.

3.4.1 Model Calibration: Linear Viscoelastic and Hyperelastic Parameters

We first focus our analysis on considering the linear viscoelastic model. The initial analysis requires identification of the hyperelastic model parameters, meaning we wish to quantify the uncertainty associated with the following set of parameters,

$$\theta = [G_c, \lambda_{max}, G_e, \gamma, \eta], \tag{3.22}$$

where G_c, λ_{max}, and G_e can be found in (3.21), γ is found in (3.16), and η is found in (3.13). Using the MCMC sampling approach outlined in Chapter 2, we can calibrate the model parameters in (3.22) with respect to the slowest experimental stretch rate ($\dot{\lambda} = 6.7 \times 10^{-5}$ Hz).

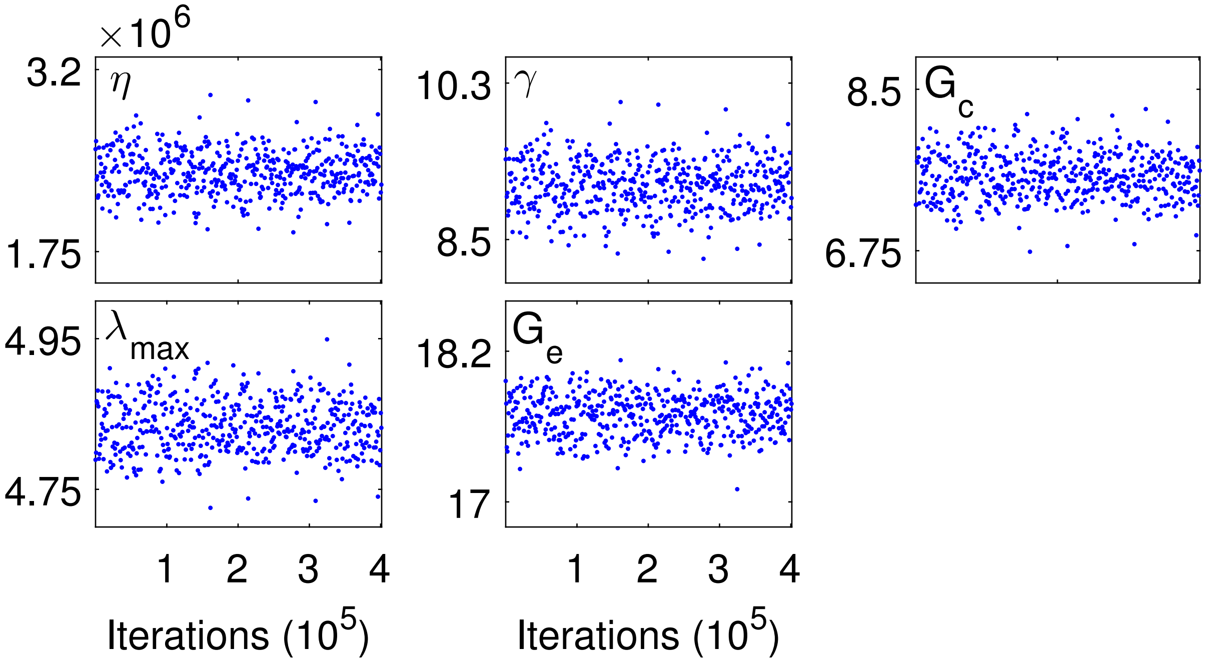

Figure 3.3: Parameter chains for calibration at slowest stretch rate with integer order, linear viscoelastic, and nonaffine hyperelastic models.

In theory the hyperelastic nature of the material should be independent of the rate of deformation. Therefore, we choose to identify the hyperelastic distributions at the slowest rate as the viscoelastic response should be minimal, which is in agreement with the small amount of hysteresis observed in Figure 3.2. The hope is to simplify the model by choosing a reasonable nominal value for the hyperelastic parameters, but we must first analyze the chain from the MCMC analysis.

There are several tools we can use to analyze the chain. First, we observe the sampling history for each parameter chain in Figure 3.3. After approximately 4×10^5 evaluations the chain is burned-in in the sense that it has converged to the posterior density. Qualitatively, we can make this observation based on the fact that each chain has the appearance of white noise with no significant jumps or periods of stagnation. Details regarding the criteria for statistical acceptance and convergence tests when using DRAM can be found in [21, 26, 27].

The burned-in parameter chains are used to construct marginal posterior densities, shown in Figure 3.4. This is accomplished using a kernel density estimation (KDE) algorithm. It

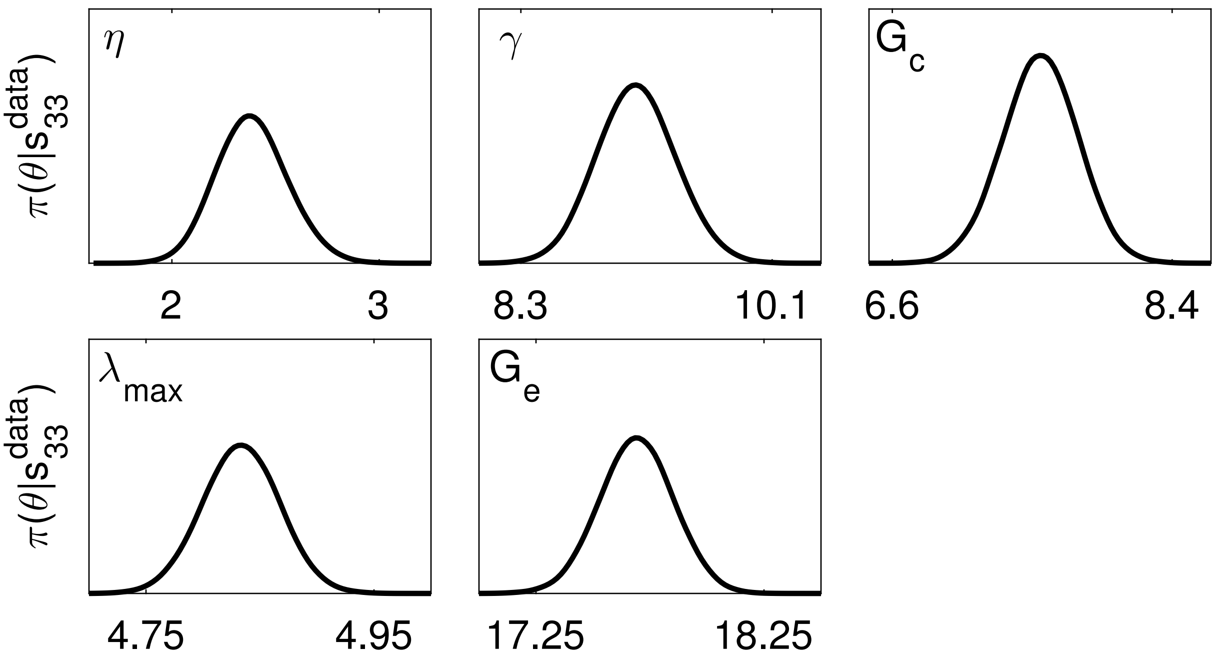

Figure 3.4: Marginal posterior densities for calibration at slowest stretch rate with integer order, linear viscoelastic, and nonaffine hyperelastic models.

is important to point out that the posterior densities need not be Gaussian distributions; however, for this model all parameter distributions appear to be approximately normal. This is an important observation, especially with regard to the hyperelastic model parameters. In theory the hyperelastic behavior of the material should be independent of rate; therefore, to simplify model analysis at higher rates we can simply use the hyperelastic parameters found at the slowest rate. As the parameter distributions appear to be normally distributed, it is reasonable to take the mean value for each hyperelastic parameter and use it for analysis at higher rates.

Another component of analyzing the chain is quantifying the correlation between parameters. We quantify this correlation with the pairwise plots in Figure 3.5. Several nearly single-valued linear correlations can be observed between parameters. Specifically, the nearly single-valued correlation we see between the viscoelastic damping coefficient, η, and the viscoelastic modulus, γ, indicates that the two parameters are not identifiable in the sense that they cannot be uniquely determined by the data since a single value for one can be used to

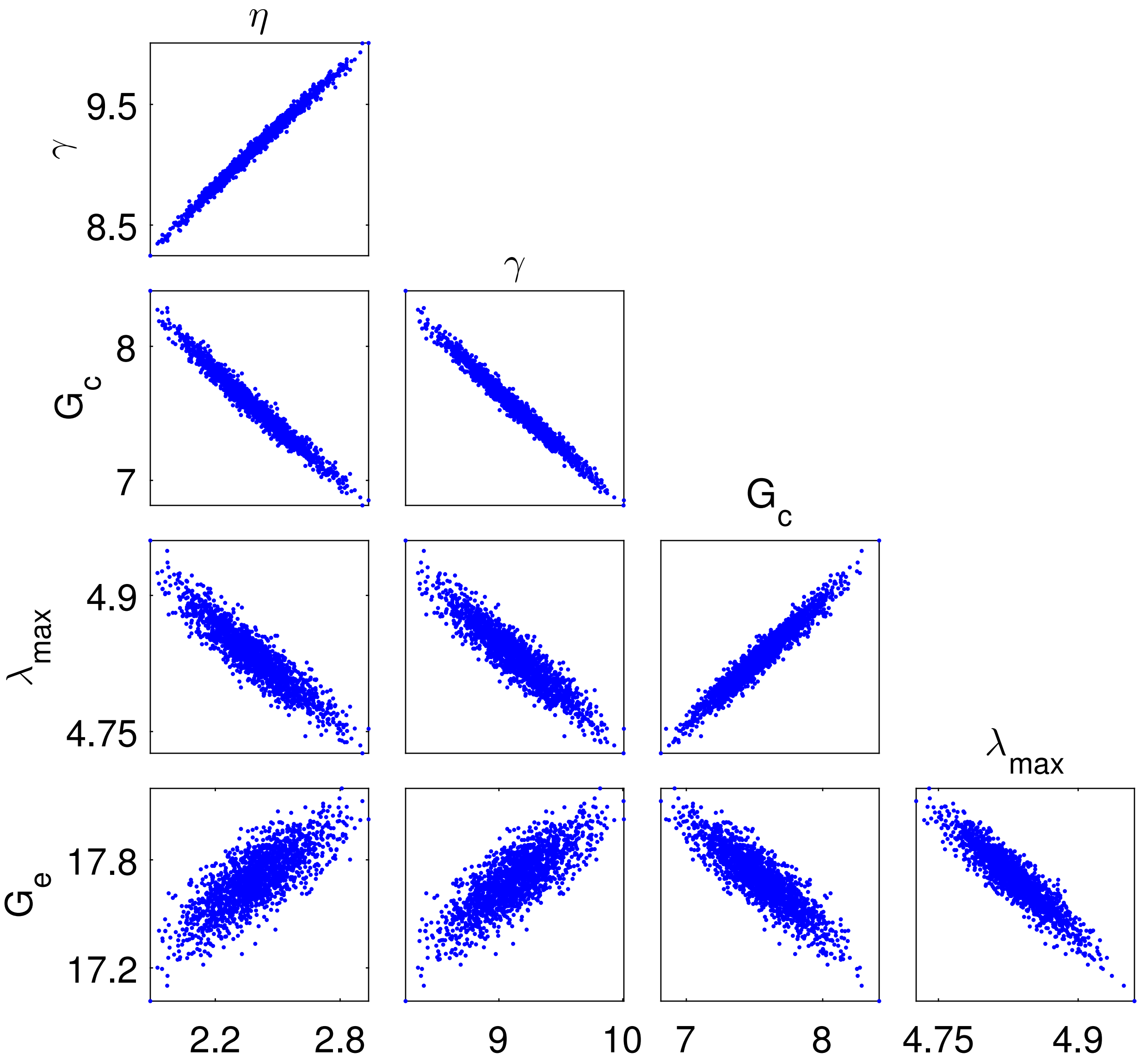

Figure 3.5: Pairwise correlation between each sampled parameter for calibration at the slowest stretch rate using the integer order, linear viscoelastic, and nonaffine hyperelastic models. A nearly single-valued linear correlation is observed between several parameters.

define the other. A similar correlation can be observed between the crosslinking modulus, G_c, and the two viscoelastic parameters. The strength of the correlation can be observed by the amount of spread observed in the pairwise plot.

We are also interested in observing how the uncertainty propagates through the model to affect the quantity of interest, in this case the nominal stress. Before doing that, however, we wish to decouple the hyperelastic and viscoelastic response. In theory, the hyperelastic parameters should be independent of the deformation rate. As such, it is reasonable to assume a nominal value for the hyperelastic parameters. In this case we choose the mean values of the densities seen in Figure 3.4 for G_c, G_e, and λ_{max}. We then focus our analysis on identification of the viscoelastic parameters.

3.4.2 Model Calibration: Linear Viscoelastic Parameters

In this next step we will follow a very similar approach, except we have now chosen nominal values for the hyperelastic parameters. So, for implementing the MCMC algorithm, we are interested in just the viscoelastic parameters,

$$\theta = [\gamma, \eta]. \tag{3.23}$$

The linear viscoelastic model was calibrated at each stretch rate separately, and a different set of parameter distributions was found in each case. A summary of the parameter statistics found at each rate is given in Table 3.1. For all calibration cases the parameter distributions were found to be approximately Gaussian.

We have demonstrated how we analyze uncertainty associated with input parameters, but it is also of interest to see how that uncertainty affects the output. A statistically significant

Table 3.1: Integer Order Linear Viscoelastic: Model parameter means ($\bar{\theta}$) and standard deviations (σ_θ). Nominal value of hyperelastic parameters: $G_c = 7.55$ kPa, $\lambda_{max} = 4.83$, and $G_e = 17.7$ kPa.

Stretch Rate (1/s)	η		γ	
	$\bar{\eta}$	σ_η	$\bar{\gamma}$	σ_γ
6.7×10^{-5}	2.38×10^{6}	1.08×10^{4}	9.12	1.39×10^{-2}
0.0472	7.36×10^{3}	102.2	17.3	5.67×10^{-2}
0.10	3.05×10^{3}	51.9	17.2	7.75×10^{-2}
0.335	1.84×10^{3}	34.3	32.6	1.50×10^{-1}
0.50	1.23×10^{3}	25.3	33.6	1.75×10^{-1}
0.67	7.37×10^{2}	12.4	33.4	1.71×10^{-1}

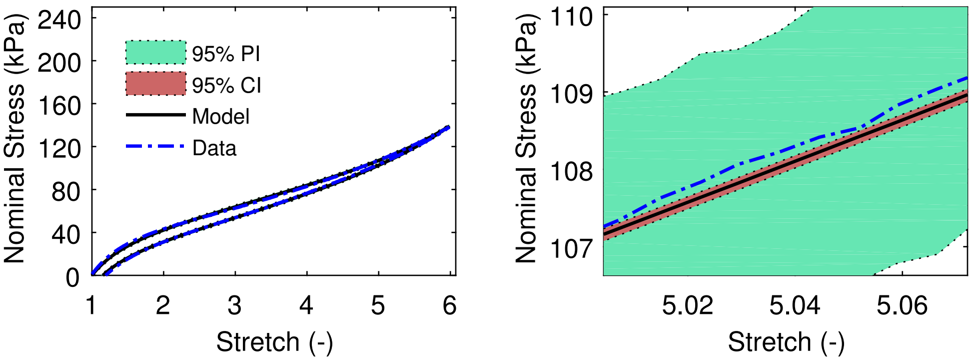

(a) 6.7×10^{-5} Hz (b) 6.7×10^{-5} Hz, Zoomed-In

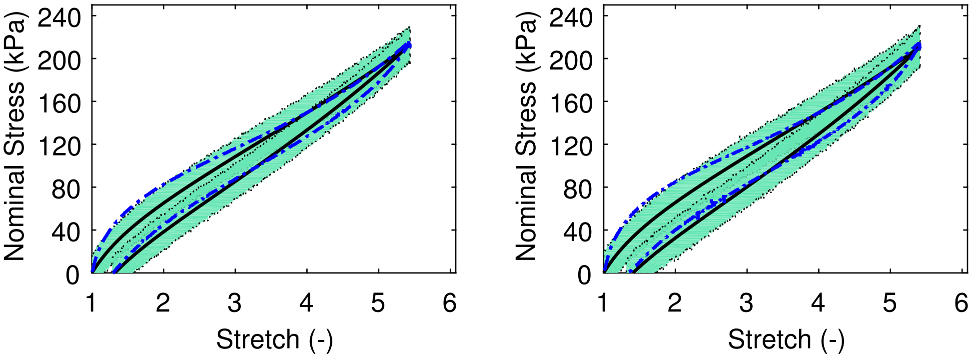

(c) 0.335 Hz (d) 0.67 Hz

Figure 3.6: Linear viscoelastic model response when predicting behavior at the same rate used to calibrate. Parameter uncertainty propagated through model to generate 95% prediction (PI) and credible (CI) intervals. (b) Highlights the scale of prediction and credible intervals.

number of samples are taken from the posterior distributions and the resulting uncertainty is propagated through the model. This information is used to generate 95% credible and prediction intervals, as shown in Figure 3.6. Figure 3.6 demonstrates the model response when predicting the material behavior at the same rate used for calibration.

3.4.3 Model Prediction Procedure

In Sections 3.4.1 and 3.4.2 several specific calibration studies were highlighted. Additional tests were performed by calibrating the model at each stretch rate separately. In each case a different set of parameter distributions were identified. The uncertainty associated with these distributions, as well as the observation error, was propagated through the model.

This allowed for the calculation of credible and prediction intervals, giving an estimate on the amount of uncertainty there is in the output. The error between the statistical model and the data was measured using

$$e_{mcmc} = \frac{1}{N} \sum (\sigma^{model} - \sigma^{data})^2 \tag{3.24}$$

where N is the number of data points, σ^{model} is the model stress, and σ^{data} is the stress measured experimentally. Each set of parameters was tested by predicting the behavior at all stretch rates. A summary of the error based on the calibration and predictions is given in Tables 3.2 and 3.4. Also, plots of the predicted model response across the range of rates tested are given for each model.

To assess the reliability of our model calibration, it is important to test the resulting parameters on non-trained boundary conditions. Parameter distributions are identified using one data set, i.e., one particular stretch rate. We then sample from the resulting parameter distributions to generate our estimated model response. This predicted response is compared with data sets collected at other stretch rates, which provides an indication as to how well the model predicts the material behavior. This procedure is followed in order to test all the models under consideration. We first consider how well the linear viscoelastic model predicts the material behavior.

3.4.4 Model Prediction: Linear Viscoelasticity

When performing model calibration it is extremely important to test the model using distinct data sets. That is to say, if a model is calibrated with a specific type of experiment, then in general it is expected that the model will perform well at predicting the behavior of that experiment. In the present study, if the model is calibrated at a specific stretch rate, then it is expected that the model response will agree with that stretch rate data. The true test of the effectiveness of a model is determined by how well it predicts behavior of data not used for calibration. To test the linear viscoelastic model we will take the set of parameters calibrated at a given rate, and then use those parameter values to predict the behavior at all the other rates. A representative set of results are shown in Figure 3.7, where the parameters

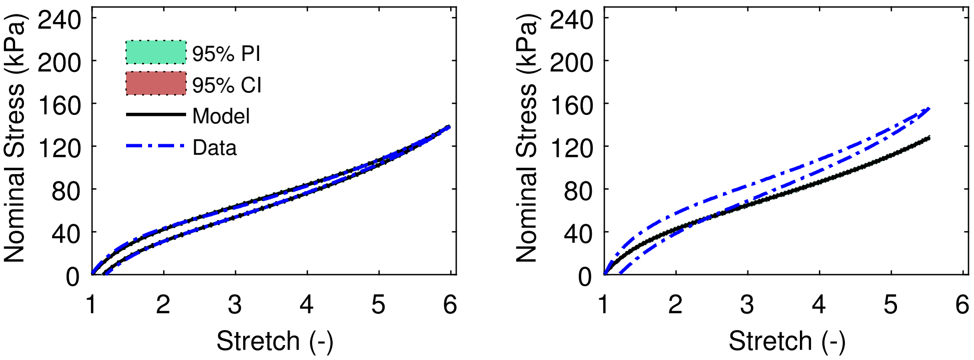

(a) 6.7×10^{-5} Hz (b) 0.0472 Hz

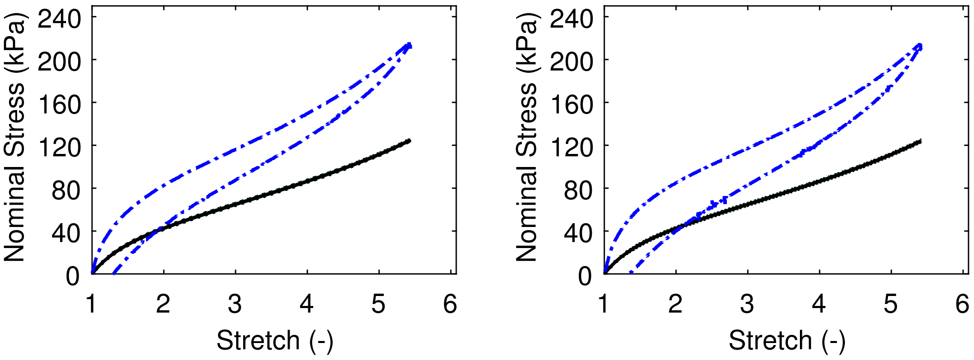

(c) 0.335 Hz (d) 0.67 Hz

Figure 3.7: Prediction of material behavior at nontrained boundary conditions using the integer order linear viscoelastic model. Model was calibrated using $\dot{\lambda} = 6.7 \times 10^{-5}$ Hz. Error measurements are given in Table 3.2. Results not shown for $\dot{\lambda} = 0.10$ and 0.50 Hz. Note that 95% prediction (PI) and credible (CI) intervals are not visible at this scale.

calibrated at $\dot{\lambda} = 6.7 \times 10^{-5}$ Hz are used to predict the stress response at all experimental rates. As expected, the model agrees well at the rate used for calibration; however, the model fails to predict the viscoelastic behavior at higher rates. This response is observed regardless of the parameter set tested as seen by the error measurements presented in Table 3.2. It is important to observe that poor model prediction does not imply large uncertainty. Recall that credible intervals reflect propagating the parameter uncertainty through the model. The calibration yielded relatively low amounts of uncertainty for the parameters. This could be an indication that the model as formulated is extremely sensitive to the parameter values.

Table 3.2: Integer Order Linear Viscoelastic: Model error in units of kPa^2. Model evaluated using parameter distributions calibrated using the data specified in the first column.

Calibrated Rate ($1/s$):	Predicted Rate ($1/s$) 6.7×10^{-5}	0.0472	0.10	0.335	0.50	0.67	Total Error
6.7×10^{-5}	0.9	263	251	2484	2725	2418	8142
0.0472	450.7	11	49	945	1067	927	3450
0.10	452.6	102	18	1002	1110	951	3635
0.335	453.2	806	560	74	95	219	2207
0.50	453.5	1054	661	116	72	162	2518
0.67	453.7	1221	852	420	175	93	3215

3.4.5 Model Calibration: Nonlinear Viscoelastic and Hyperelastic Parameters

A similar approach is taken with regard to the nonlinear viscoelastic model. We first consider the combined parameter set

$$\theta = [G_c, \lambda_{max}, G_e, \gamma, \eta, \beta], \tag{3.25}$$

where G_c, λ_{max}, and G_e can be found in (3.21), and γ and β, are found in (3.14) and η is in (3.13). Recall that in theory the hyperelastic parameters should be independent of deformation rate, so we will once again use MCMC sampling to calibrate the model parameters in (3.22) with respect to the data from the slowest experimental stretch rate ($\dot{\lambda} = 6.7 \times 10^{-5}$ Hz).

From Figure 3.8, we see that the parameter chains are not nearly as stable as those observed in Figure 3.3. Additionally, we observe that the posterior densities are no longer Gaussian in nature, which is seen in Figure 3.9. This is often the case when you increase the number of parameters being sampled. The non-Gaussian nature of the posteriors is acceptable, but a careful assessment is required when interpreting the results.

The nonlinear model by its very definition has correlation between the hyperelastic and viscoelastic terms. The correlation is clearly seen in Figure 3.10, where nearly single-valued linear and nonlinear relationships are evident between several parameter pairs. This lack of

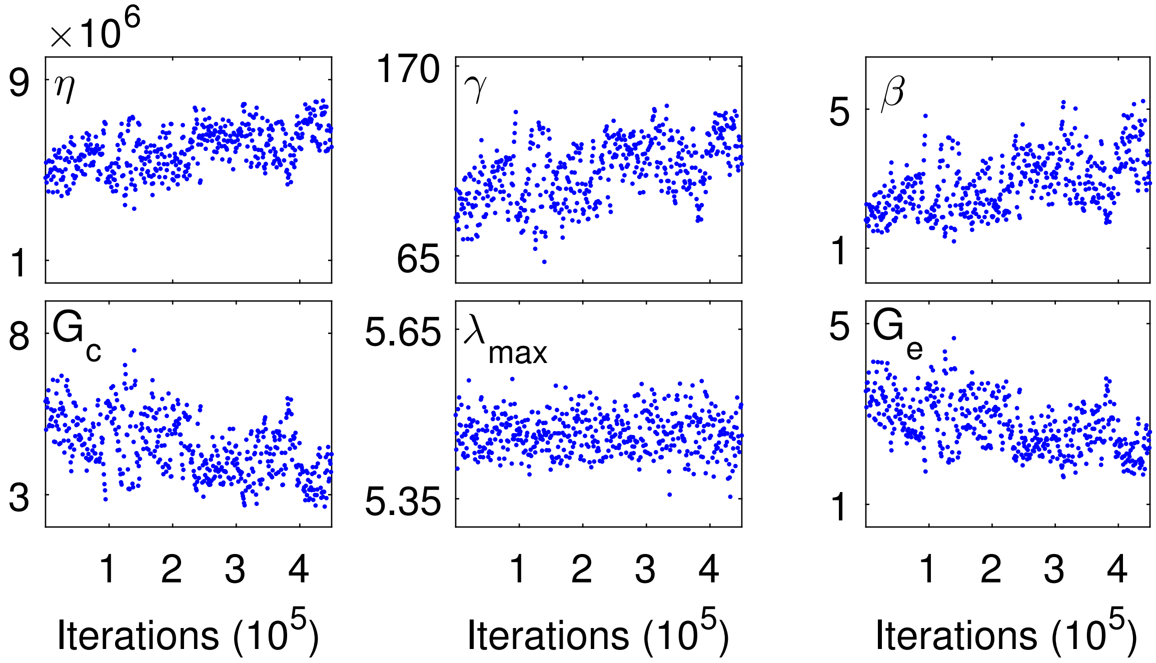

Figure 3.8: Parameter chains for calibration at slowest stretch rate with integer order, nonlinear viscoelastic, and nonaffine hyperelastic models.

identifiability is typically addressed in one of two ways. One approach is to employ physical analysis to reduce the non-identifiable parameters. In some cases it is impossible to eliminate these terms, so instead we define the non-identifiable parameters using physically reasonable nominal values. The latter approach was chosen for this analysis, where we set the nominal value for the hyperlastic parameters by taking the mean of the posterior densities observed in Figure 3.9. It is important to realize that the observed distributions are not all Gaussian in nature, so further analysis should be interpreted in light of the uncertainty introduced by taking these nominal values. With the hyperelastic parameter set, we can now proceed to identify the viscoelastic parameters at each stretch rate.

3.4.6 Model Calibration: Nonlinear Viscoelastic Parameters

At this point we can perform MCMC calibration for the parameter set

$$\theta = [\gamma, \eta, \beta], \tag{3.26}$$

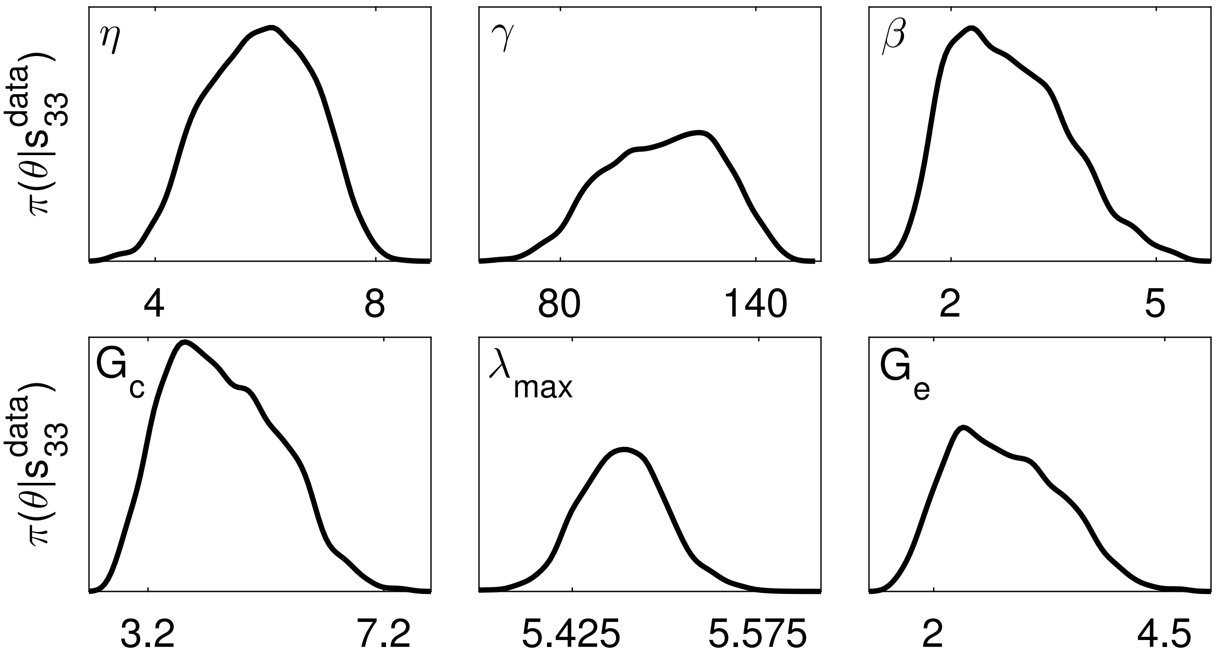

Figure 3.9: Marginal posterior densities for calibration at slowest stretch rate with integer order, nonlinear viscoelastic, and nonaffine hyperelastic models.

on each stretch rate data set. A summary of the parameter statistics found at each rate is given in Table 3.3. For all calibration cases the parameter distributions were found to be approximately Gaussian.

Propagating the uncertainty through the model, we find reasonable model predictions

Table 3.3: Integer Order Nonlinear Viscoelastic: Model parameter means ($\bar{\theta}$) and standard deviations (σ_θ). Nominal value of hyperelastic parameters: $G_c = 4.47$ kPa, $\lambda_{max} = 5.47$, and $G_e = 2.77$ kPa.

Stretch	η		γ		β	
Rate (1/s)	$\bar{\eta}$	σ_η	$\bar{\gamma}$	σ_γ	$\bar{\beta}$	σ_β
6.7×10^{-5}	5.9×10^6	1.6×10^5	111	0.99	2.68	6.7×10^{-3}
0.0472	4.9×10^3	90.3	121	0.57	4.08	1.0×10^{-2}
0.10	1.7×10^3	30.9	110	0.48	4.25	1.3×10^{-2}
0.335	1.1×10^3	25.9	136	1.20	6.25	2.3×10^{-2}
0.50	1.1×10^3	49.5	118	4.34	6.07	3.4×10^{-2}
0.67	5.2×10^2	12.2	118	1.31	6.42	2.8×10^{-2}

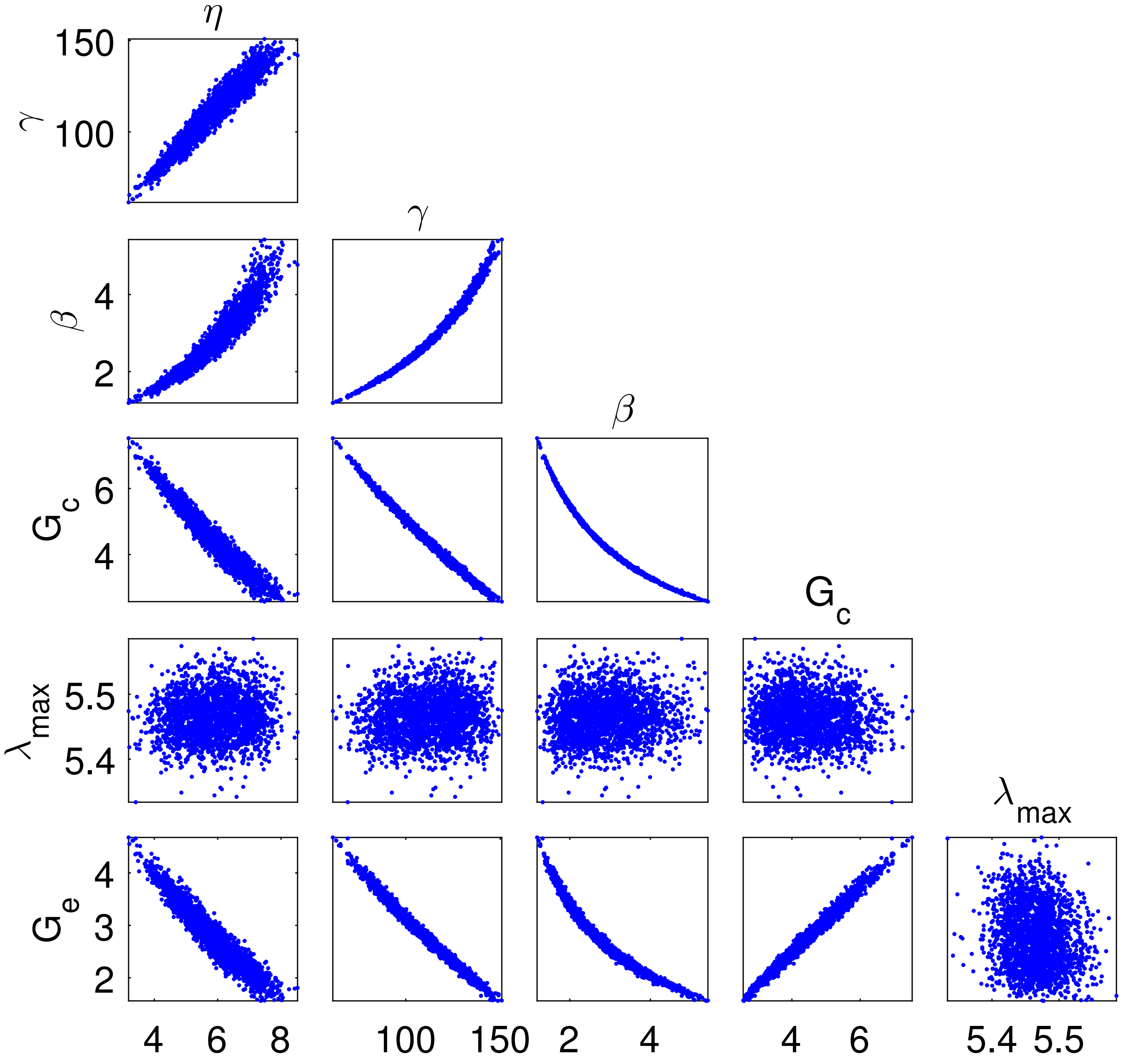

Figure 3.10: Pairwise correlation between each sampled parameter for calibration at the slowest stretch rate using the integer order, nonlinear viscoelastic, and nonaffine hyperelastic models. A nearly single-valued linear correlation is observed between several parameters.

at each rate. Figure 3.11 demonstrates the model response when predicting the material behavior at the same rate used for calibration. This gives us confidence that the attributes of the model can capture the physical behavior of the material; however, it still leaves the question as to whether a single set of parameters can be used to capture the entire range of

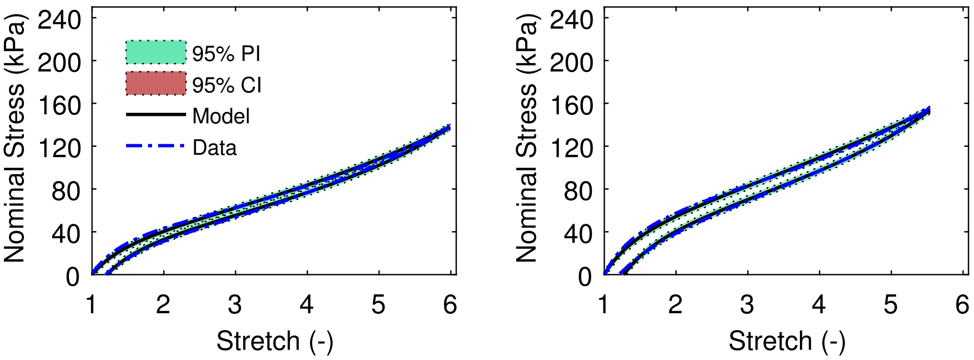

(a) 6.7×10^{-5} Hz (b) 0.0472 Hz

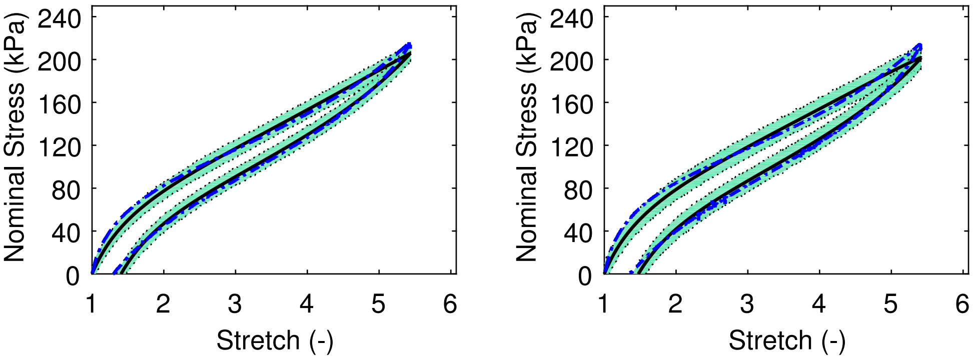

(c) 0.335 Hz (d) 0.67 Hz

Figure 3.11: Nonlinear viscoelastic model response when predicting behavior at the same rate used to calibrate. Parameter uncertainty propagated through model to generate 95% prediction (PI) and credible (CI) intervals. Note that the 95% credible intervals are not visible at this scale.

data tested.

3.4.7 Model Prediction: Nonlinear Viscoelasticity

Once again, we test the model to determine how well it predicts the viscoelastic behavior against data not used for model calibration. As seen in Figure 3.12, the parameter set found by calibrating at the fastest stretch rate does not perform well at predicting the response at slower rates. The error measurements presented in Table 3.4 highlight the parameter sensitivity to rate. From these measurments, we can clearly say that the model parameters are rate dependent.

3.5 Conclusions

When considering the linear viscoelastic model, it was observed in Figure 3.6 that the model response performed reasonably well at slower stretch rates. This potentially highlights that a transition occurs as you increase the rate of deformation and at a certain point nonlinear effects characterize the physics. As seen in Figure 3.11, the nonlinear viscoelastic model performs well at capturing the physical characteristics of the stress reponse at each rate. However, for both the linear and nonlinear models, we observe the same limiting characteristics that the model parameters are rate dependent.

The predictive capability of the linear model is seen in Figure 3.7, where the parameters that describe the physics at the slowest rate clearly do not perform well predicting behavior at higher rates. A rigorous quantitative assessment in Table 3.2 reveals the linear model's strong parameter sensitivity to rate. Similar observations can be made with regard to the nonlinear model, highlighted by the predictions shown in Figure 3.12 and the error measurements given in Table 3.4. Figure 3.12 shows how the parameters at the highest rate perform poorly at predicting behavior at slower rates. Furthermore, Table 3.4 shows that none of the parameter sets found at intermediate rates perform any better when it comes to model prediction.

The approach presented in this chapter shows promise for modeling the viscoelastic behavior of dielectric elastomers. However, the model lacks robustness with respect to the rate of deformation. Throughout the theoretical model development, the assumption was made

Table 3.4: Integer Order Nonlinear Viscoelastic: Model error in units of kPa^2 when using mean parameter value from calibration at single stretch rate.

Calibrated	Predicted Rate ($1/s$)						Total
Rate ($1/s$):	6.7×10^{-5}	0.0472	0.10	0.335	0.50	0.67	Error
6.7×10^{-5}	2.6	210	205	2313	2526	2252	7508
0.0472	239	3.3	47.2	566	620	528	2003
0.10	222	33.9	4.2	657	643	485	2044
0.335	1336	364	472	17.9	52.6	193	2436
0.50	852	166	243	38.2	36.6	118	1455
0.67	933	215	220	195	140	27.7	1730

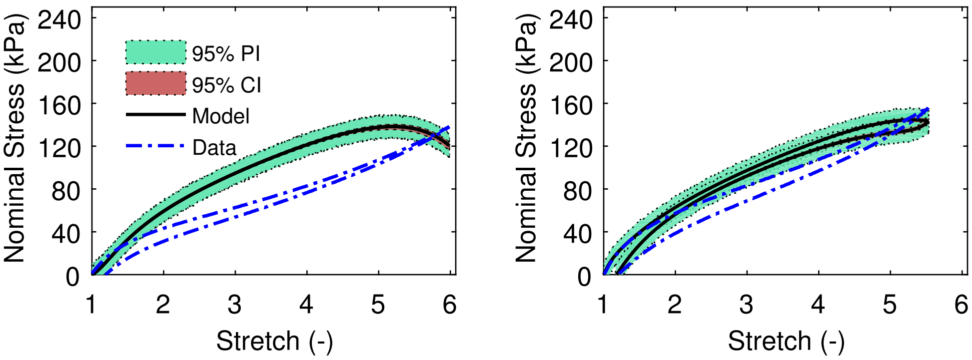

(a) $\dot{\lambda} = 6.7 \times 10^{-5}$ Hz (b) $\dot{\lambda} = 0.0472$ Hz

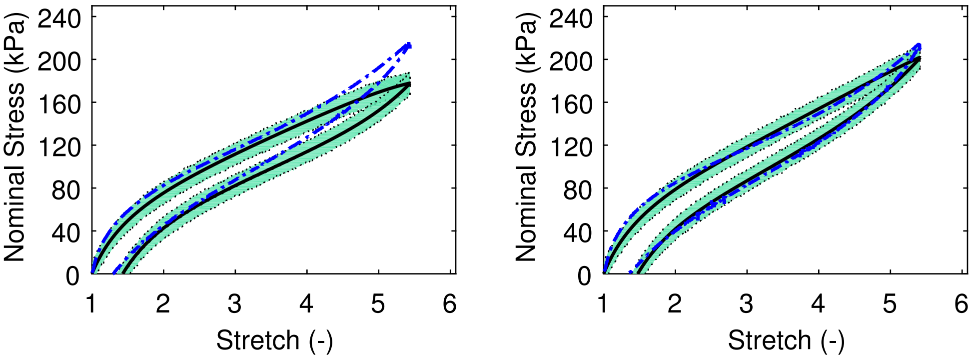

(c) $\dot{\lambda} = 0.335$ Hz (d) $\dot{\lambda} = 0.67$ Hz

Figure 3.12: Prediction of material behavior at nontrained boundary conditions using the integer order nonlinear viscoelastic model. Model was calibrated using $\dot{\lambda} = 0.67$ Hz. Error measurements are given in Table 3.4. Results not shown for $\dot{\lambda} = 0.10$ and 0.50 Hz.

that the material behaved as a conventional nonlinear solid. In Chapter 4 we will introduce the idea of modeling the elastomers as fractal media, and using fractional order calculus operators to characterize the physical response.

CHAPTER 4

VISCOELASTICITY OF SOFT ELASTOMERS: FRACTIONAL ORDER APPROACH

4.1 Introduction

In Chapter 3 we introduced two different models for predicting the viscoelastic behavior of dielectric elastomers. The nonlinear model performed better at capturing the observed phenomena across the range of rates tested; however, both models suffered from being limited to rate dependent model parameters. In this chapter we will present an alternative framework which uses fractional order calculus operations to model viscoelasticity.

Fractional calculus has been applied extensively in the field of linear viscoelasticity due to its ability to model phenomena with long memory [44]. The original application of fractional methods to the study of viscoelasticity had no physical basis. A physical justification for this approach was proposed by Bagley and Torvik [4], who extended the work of both Ferry [18] and Zimm [90], which is based on the molecular theory of Rouse. Fractional calculus has been shown to lead to well-posed structural dynamics problems with both elastic and viscoelastic components [4]. Furthermore, fractional order methods have shown the potential for reducing the number of parameters required to accurately describe the dynamic properties [1].

The rest of this chapter will be divided into the following sections. In Section 4.2 the basic definitions for fractional order calculus operators will be explained, as well as how these definitions are implemented within the context of finite deformation discussed in Chapter 3. A discussion of the model parameter uncertainty and corresponding model predictions will be given in Section 4.3, and concluding remarks will be provided in Section 4.4.

4.2 Theory

The theoretical derivation for the fractional order approach is best understood within the context of fractal media. A complete discussion of this model development can be found in the submitted manuscript [46]. In the current study we are considering uniform loading, independent of position, which means our models are the same for both fractal and non-fractal media. Furthermore, the additional convective term that appears in the time derivative associated with fractal media disappears as a result of the uniform loading. Fractals are sometimes defined as continuous functions with no derivative (tangents) at any point. Subsequently, in analyzing the local properties of a fractal set, it is reasonable to use a fractional derivative [52]. The key attribute of the constitutive models considered here is that when converted to non-fractal media ($c = 1$), fractional order viscoelastic models are applicable to the materials under consideration.

Before summarizing the key findings from the finite deformation energy formulations, we will first provide some brief definitions of fractional derivatives.

4.2.1 Definitions of Fractional Derivatives

There are various definitions for fractional derivatives. The widely used definitions include the Caputo, Riemann-Liouville, and the Grünwald-Letnikov fractional derivatives [65].

Definition 1: Caputo's fractional derivative of order α is defined as

$$(D_C^\alpha f)(t) = \frac{1}{\Gamma(n-\alpha)} \int_0^t \frac{f^{(n)}(s)}{(t-s)^{\alpha+1-n}} ds, \quad n-1 < \alpha \leq n, \ n \in \mathbb{N}, \tag{4.1}$$

where $\alpha > 0$ is the order of the derivative and n is the smallest integer greater than α. For the Caputo derivative we have

$$D_C^\alpha c = 0, \quad (c \text{ is a constant}) \tag{4.2}$$

$$D_C^\alpha t^\nu = \begin{cases} \frac{\Gamma(\nu+1)}{\Gamma(\nu+1-\alpha)} t^{\nu-\alpha}, & n-1 < \alpha < n, \ \nu > n-1, \ \nu \in \mathbb{R}, \\ 0, & n-1 < \alpha < n, \ \nu \leq n-1, \ \nu \in \mathbb{N}. \end{cases} \tag{4.3}$$

Definition 2: Riemann-Liouville's fractional derivative of order α is defined as

$$(D_R^\alpha f)(t) = \frac{1}{\Gamma(n-\alpha)} \frac{d^n}{dt^n} \int_0^t \frac{f(s)}{(t-s)^{\alpha+1-n}} ds, \quad n-1 < \alpha \leq n, \ n \in \mathbb{N}, \tag{4.4}$$

where $\alpha > 0$ is the order of the derivative and n is the smallest integer greater than α. For the Riemann-Liouville's derivative we have

$$D_R^{\alpha} c = c \frac{t^{-\alpha}}{\Gamma(1-\alpha)}, \quad (c \text{ is a constant}) \tag{4.5}$$

$$D_R^{\alpha} t^{\nu} = \tfrac{\Gamma(\nu+1)}{\Gamma(\nu+1-\alpha)} t^{\nu-\alpha}, \;\; n-1 < \alpha < n, \; \nu > -1, \; \nu \in \mathbb{R}. \tag{4.6}$$

Definition 3: The Grünwald-Letnikov fractional derivative of order α is defined as

$$(D_G^{\alpha} f)(t) = lim_{h \to 0} \frac{1}{h^{\alpha}} \sum_{0 \le m < \infty} (-1)^m \left(\begin{smallmatrix} \alpha \\ m \end{smallmatrix} \right) f(t - mh). \tag{4.7}$$

Proposition 1: Let $t > 0, \; \alpha \in \mathbb{R}, \; n-1 < \alpha < n \in \mathbb{N}$. Then the following relation between the Riemann-Liouville and Caputo operators holds

$$(D_C^{\alpha} f)(t) = (D_R^{\alpha} f)(t) - \Sigma_{k=0}^{n-1} \frac{t^{k-\alpha}}{\Gamma(k+1-\alpha)} f^{(k)}(0). \tag{4.8}$$

Proposition 2: If $f(t)$ is $(n-1)$ times differentiable in $[0, b]$ and the n^{th} derivative of $f(t)$ is integrable in $[0, b]$. Then, for every $n - 1 < \alpha < n$ we have

$$(D_G^{\alpha} f)(t) = (D_R^{\alpha} f)(t), \quad 0 \le t \le b. \tag{4.9}$$

We have used D_t^{α} as a fractional derivative and we will call it the fractional time derivative.

The Riemann-Liouville derivative has certain disadvantages when trying to model real-world phenomena [56], so the Caputo fractional derivative has been used for most analyses. In the linear model of viscoelasticity, we use Definition 1 since the rate of strain is known from data while Γ_{iK}^{ν} is not known *a priori*. In the nonlinear model of viscoelasticity, the rate of hyperelastic stress is not known *a priori*, only total stress and the deformation rate are known. Therefore we use the Grünwald-Letnikov fractional derivative (Definition 3) that is equivalent to the Caputo fractional derivative according to Propositions 1 and 2. This is because the value of hyperelastic stress is zero at $t = 0$.

4.2.2 Finite Deformation Energy Formulation

The finite deformation energy relations presented in Chapter 3 maintain a similar form when derived in the context of fractal media. We will not reiterate the derivation here, but a few key equations are defined for easier reference. It will be shown that the work conjugate variable to the deformation gradient is the nominal stress

$$s_{iK} = \frac{\partial \hat{\psi}}{\partial F_{iK}} = \frac{\partial \psi_{\infty}}{\partial F_{iK}} - pJH_{iK} + \frac{\partial \Upsilon}{\partial F_{iK}}. \tag{4.10}$$

as well as the work conjugate relationship between viscoelastic stress and the internal state variables

$$Q^{\nu}_{iK} = -\frac{\partial \hat{\psi}}{\partial \Gamma^{\nu}_{iK}} = -\frac{\partial \Upsilon}{\partial \Gamma^{\nu}_{iK}}, \tag{4.11}$$

The derivation eventually leads to the key result presented here

$$Q^{\nu}_{iK} = \eta^{\nu} \left(\frac{d}{dt}\right)_D \Gamma^{\nu}_{iK} \tag{4.12}$$

where $(\frac{d}{dt})_D$ is a fractal time derivative. This is the form of the fractional viscoelastic constitutive law analogous to a spring-dashpot model in one dimension [32]. We can subsequently use this relationship in our linear and nonlinear viscoelastic model formulations.

4.2.3 Linear Viscoelastic Model for Fractal Media

In the linear case we suppose the energy function has the following form

$$\Upsilon_L = \sum_{\nu} \left[\frac{1}{2}\gamma^{\nu} \left(F^D_{iK} - \Gamma^{\nu}_{iK}\right)\left(F^D_{iK} - \Gamma^{\nu}_{iK}\right)\right], \tag{4.13}$$

and by using (4.11), we have

$$Q^{\nu}_{iK} = -\frac{\partial \hat{\psi}}{\partial \Gamma^{\nu}_{iK}} = \gamma^{\nu}\left(F^D_{iK} - \Gamma^{\nu}_{iK}\right). \tag{4.14}$$

By using (4.11), (4.12), (4.13) and (4.14) we have

$$\eta^{\nu}\left(\frac{d}{dt}\right)_D \Gamma^{\nu}_{iK} + \gamma^{\nu}\Gamma^{\nu}_{iK} = \gamma^{\nu} F^D_{iK}, \tag{4.15}$$

and if we apply $(\frac{d}{dt})_D$ to both sides of (4.15) we have

$$\eta^{\nu}\left(\frac{d}{dt}\right)_D \left(\left(\frac{d}{dt}\right)_D \Gamma^{\nu}_{iK}\right) + \gamma^{\nu}\left(\frac{d}{dt}\right)_D \Gamma^{\nu}_{iK} = \gamma^{\nu}\left(\frac{d}{dt}\right)_D F^D_{iK}. \tag{4.16}$$

We then apply (4.12) and (4.16) to obtain

$$\left(\frac{d}{dt}\right)_D Q^{\nu}_{iK} + \frac{1}{\tau^{\nu}} Q^{\nu}_{iK} = \gamma^{\nu}\left(\frac{d}{dt}\right)_D F^D_{iK}, \tag{4.17}$$

where $\tau^\nu = \frac{\eta^\nu}{\gamma^\nu}$.

To reduce the number of terms in the model, we suppose the rates of the internal state variables in the fractal sense are proportional to the local fractional time derivative of deformation as described in Section 4.2.5. We express this assumption as

$$\left(\frac{d}{dt}\right)_D \Gamma^\nu_{iK} = \mu^\nu_L D^{\alpha_\nu}_t F^D_{iK}, \tag{4.18}$$

and by using Eqs. (4.12) and (4.18) we have

$$Q^\nu_{iK} = \eta^\nu_L D^{\alpha_\nu}_t F^D_{iK}, \tag{4.19}$$

where $\eta^\nu_L = \eta^\nu \mu^\nu_L$, and $D^{\alpha_\nu}_t$ is the fractional time derivative of deformation as described in Section 4.2.1. This is the form of the viscoelastic constitutive law analogous to a spring-dashpot model in the one dimension fractional model.

We can see that the Clausius-Duhem inequality from (3.11) is

$$(\eta^\nu_L)^2 (D^{\alpha_\nu}_t F_{iK})^2 = F\left(\left(\frac{d}{dt}\right)_D \Gamma^\nu_{ik}, F^D_{iK}\right) \geq 0 \tag{4.20}$$

such that the second law is always satisfied for $\alpha \geq 0$, however in the experimental results we have chosen $0 \leq \alpha \leq 1$ since we have a fixed rate for the strain and the fractional derivative for $\alpha > 1$ is zero. From (4.19) we can see the fractional case has an explicit expression for Q^ν_{iK} in terms of the deformation gradient.

This linear viscoelastic stress equation will be coupled with the calculation of the hyperelastic stress in (4.10), resulting in the total stress

$$s_{iK} = \frac{\partial \psi_\infty}{\partial F^D_{iK}} - pJH_{iK} + \sum_\nu Q^\nu_{iK} \tag{4.21}$$

since in the linear viscoelastic model we have $Q^\nu_{iK} = \dfrac{\partial \Upsilon}{\partial F^D_{iK}} = -\dfrac{\partial \Upsilon}{\partial \Gamma^\nu_{iK}}$.

4.2.4 Nonlinear Viscoelastic Model for Fractal Media

In the nonlinear case we suppose the energy function has the following form

$$\Upsilon_{NL} = \sum_\nu \left[\frac{1}{2}\gamma^\nu \Gamma^\nu_{iK}\Gamma^\nu_{iK} - \beta^\nu_\infty \frac{\partial \psi_\infty}{\partial F^D_{iK}} \Gamma^\nu_{iK} + \beta^\nu_\infty \psi_\infty\right] \tag{4.22}$$

following prior analysis given in [50]. By using (3.4) we then have the viscoelastic stress function

$$Q^{\nu}_{iK} = -\frac{\partial \hat{\psi}}{\partial \Gamma^{\nu}_{iK}} = -\gamma^{\nu}\Gamma^{\nu}_{iK} + \beta^{\nu}_{\infty}\frac{\partial \psi_{\infty}}{\partial F^{D}_{iK}}. \tag{4.23}$$

Similar to the linear fractional-order model given by (4.18), we suppose here that the rate of internal state variables in the fractal sense is proportional to the local fractional time derivative of the hyperelastic stress. More details describing this assumption are given in Section 4.2.5. By this assumption we have

$$\left(\frac{d}{dt}\right)_{D} \Gamma^{\nu}_{iK} = \mu^{\nu}_{NL} D^{\alpha_{\nu}}_{t} s^{\infty}_{iK}. \tag{4.24}$$

We can re-express this by using (4.12) and (4.24) to give the viscoelastic stress

$$Q^{\nu}_{iK} = \eta^{\nu}_{NL} D^{\alpha_{\nu}}_{t} s^{\infty}_{iK}, \tag{4.25}$$

where $\eta^{\nu}_{NL} = \eta^{\nu}\mu^{\nu}_{NL}$. Similar to the linear case, we also find that the Clausius-Duhem inequality is satisfied for all values $0 \leq \alpha \leq 1$.

The work conjugate variable for Γ^{ν}_{iK} is

$$\frac{\partial \Upsilon_{NL}}{\partial \Gamma^{\nu}_{iK}} = \gamma^{\nu}\Gamma^{\nu}_{iK} - \beta^{\nu}_{\infty} s^{\infty}_{iK}, \tag{4.26}$$

so that by using (4.26) we have

$$\Gamma^{\nu}_{iK} = \frac{1}{\gamma^{\nu}}\left(\frac{\partial \Upsilon_{NL}}{\partial \Gamma^{\nu}_{iK}} + \beta^{\nu}_{\infty} s^{\infty}_{iK}\right). \tag{4.27}$$

The work conjugate variable for F^{D}_{rS} is

$$\frac{\partial \Upsilon_{NL}}{\partial F^{D}_{rS}} = \beta^{\nu}_{\infty} s^{\infty}_{rS} - \beta^{\nu}_{\infty}\frac{\partial s^{\infty}_{iK}}{\partial F^{D}_{rS}}\Gamma^{\nu}_{iK}, \tag{4.28}$$

By using (4.11), (4.25), (4.27) and (4.28) we have

$$\frac{\partial \Upsilon_{NL}}{\partial F^{D}_{rS}} = \beta^{\nu}_{\infty} s^{\infty}_{rS} - \beta^{\nu}_{\infty}\frac{\partial s^{\infty}_{iK}}{\partial F^{D}_{rS}}\Big(\frac{1}{\gamma^{\nu}}(\beta^{\nu}_{\infty} s^{\infty}_{iK} - \eta^{\nu}_{NL} D^{\alpha_{\nu}}_{t} s^{\infty}_{iK})\Big). \tag{4.29}$$

This equation will be coupled with the calculation of the hyperelastic stress which results in the total stress in (4.10).

4.2.5 Internal State Variables and Fractional Derivative of Strain

To reduce the terms in the fractional model of viscoelasticity, as discussed in Sections 4.2.3 and 4.2.4, we have approximated the internal state variables by the fractional derivative of strain in the linear case and the fractional derivative of hyperelastic stress in the nonlinear case. We show numerically why this approximation is implemented in the linear case. A similar analysis can be performed for the nonlinear case.

To show that the assumption in (4.18) is reasonable, we solve (4.15) for the internal state variable by choosing the parameters η and γ which have been reported in [50]. Since the magnitude of the rate of stretch is constant during the experiments, we can find the fractional derivative of strain by using Definition 1 in Section 4.2.1. In Figure 4.1, we show agreement between the internal state variables and the fractional derivative of deformation. This agreement shows the assumption in (4.18) is reasonable.

4.2.6 Summary of Models and Parameters

We summarize here the models and parameters that will be investigated using Bayesian model calibration techniques. We denote calibration parameters by θ to differentiate them from parameters whose values are assumed fixed and known. Note, the viscoelastic model is implemented in conjunction with a nonaffine hyperelastic model which was discussed in Chapter 3.

The linear viscoelastic nonaffine model is given by (4.19) and (3.21) and has the five parameters

$$\theta = [G_c, G_e, \lambda_{\max}, \alpha, \eta_L]. \tag{4.30}$$

From previous discussion of the nonaffine hyperelastic model we know that G_c is the crosslink modulus, G_e is the entanglement modulus, and λ_{max} designates the onset of strain hardening. The two additional parameters from the linear viscoelastic model (4.19) are the order of the fractional derivative (α) and a damping coefficient (η_L). It is assumed that α is material dependent, which is why we include it in our calibration parameter set. We also consider the case when the hyperelastic parameters G_c, G_e and $\lambda_{\max}$ are identified at the slowest stretch rate and fixed since these parameters are independent of the rate. This provides a method to

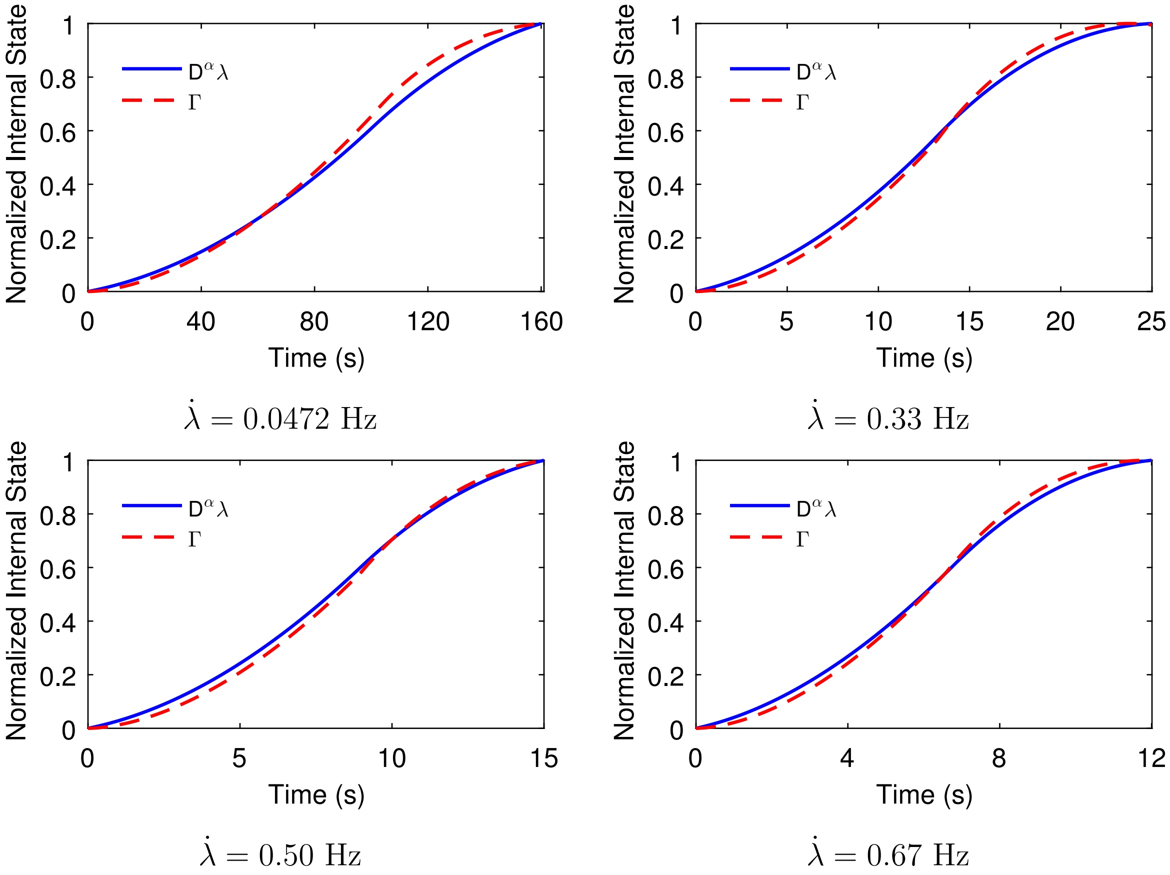

$\dot{\lambda} = 0.0472$ Hz

$\dot{\lambda} = 0.33$ Hz

$\dot{\lambda} = 0.50$ Hz

$\dot{\lambda} = 0.67$ Hz

Figure 4.1: Numerical agreement between internal state variable and fractional derivative of deformation

illustrate the predictive capabilities of the model. The resulting linear viscoelastic nonaffine model has the two viscoelastic parameters

$$\theta = [\alpha, \eta_L]. \tag{4.31}$$

The nonlinear viscoelastic model has seven parameters

$$\theta = [G_c, G_e, \lambda_{\max}, \alpha, \eta_{NL}, \beta, \gamma] \tag{4.32}$$

based on (4.29) and (3.21). The viscoelastic model obtained with fixed hyperelastic parameters has the four calibration parameters

$$\theta = [\alpha, \eta_{NL}, \beta, \gamma]. \tag{4.33}$$

4.3 Uncertainty Analysis

This section summarizes the Bayesian calibration studies done using the Markov Chain Monte Carlo (MCMC) algorithm. For a description of the Bayesian statistical analysis used; see [50]. For a complete description of the theory; see Chapter 8 of [75]. The analysis was guided by the following objectives:

(i) Assess parameter uncertainty using Bayesian analysis and determine the degree to which parameters can be uniquely identified. We consider both the hyperelastic parameters and fractional order viscoelastic parameter sets (4.30),(4.31), (4.32), and (4.33).

(ii) Test the predictive capabilities of the fractional order model in comparison to the integer order model from Chapter 3. This is motivated by the desire to predict constitutive behavior over a broad range of stretch rates as outlined in Section 3.1.

(iii) Determine if fractional order parameters are rate dependent. Accurate prediction at non-trained boundary conditions is important for application and crucial in determining the actual significance of a model using inverse methods.

Our analysis begins by employing the Bayesian methods described in Chapter 2 to construct the densities for the parameter sets in each model. We begin by considering the five-parameters given by (4.30) in the linear viscoelastic model and the seven-parameters given by (4.32) in the nonlinear viscoelastic model. Each parameter set is identified at the slowest stretch rate. Upon analysis of those two results, we consider the two-parameters given by (4.31) in the linear viscoelastic model and the four-parameters given by (4.33) in the nonlinear viscoelastic model. In these two sets, the hyperelastic parameters are held fixed and the fractional derivative viscoelastic parameters are estimated at all the higher rates. The physical reasoning for this procedure is discussed below.

The objective has two components: (1) construct marginal densities for the input parameters, which quantifies the inherent parameter uncertainties, and (2) construct pairwise correlation plots to determine which parameters are uniquely identifiable in light of the data. As the results for the integer order linear and nonlinear viscoelastic model calibrations can be found in Chapter 3, we will focus our attention on the fractional case. Note that for the hyperelastic parameters, the results reported for the crosslink and entanglement moduli (G_c

and G_e) are all in kPa, and λ_{max} is unitless. The linear viscoelastic parameter, η_L, is in kPa · s, and the nonlinear viscoelastic parameters, η_{NL}, γ, and β are in kPa · s, kPa, and unitless, respectively. Finally, the fractional order, α is also a unitless measure.

4.3.1 Model Calibration: Linear Viscoelasticity

From the calibration of the linear viscoelastic fractional order model, we have several means by which to assess the results and quantify the parameter uncertainty. We begin by considering calibration to stress-stretch data for the slowest stretch rate $\dot{\lambda} = 6.7 \times 10^{-5} Hz$. The parameter chains for this case are shown in Figure 4.2. This illustrates the sampling path taking by the MCMC algorithm. At 5×10^5 evaluations we note that the chains are burned-in, meaning they have converged to the fixed posterior densities. Qualitatively this is observed by the appearance of each chain being white noise with no significant jumps in the mean behavior or stagnation regions. A rigorous description of the statistical acceptance and convergence tests used by DRAM and more generally Metropolis algorithms can be found in [21, 26, 27].

With the burned-in parameter chains we can construct marginal posterior densities using a kernel density estimation (KDE) algorithm. As seen in Figure 4.3 all five model parameters have clearly defined peaks and nearly symmetric distributions. Several parameters (η, α, G_e) appear to be slightly skewed in their distributions, but nominally all densities appear to be Gaussian. This is not a requirement using Metropolis algorithms, as non-Gaussian marginal posteriors can also be constructed.

We also consider correlation between parameters as seen in the pairwise plots in Figure 4.4. The relationship observed between the fractional order α and the crosslink modulus G_c indicates a nearly single-valued correlation. This implies that the parameters are not uniquely identifiable by the data as a single value. One parameter can be used to determine the other. These types of relationships can be linear or nonlinear, and they highlight the potentially nontrivial coupling between different aspects of the model. A nearly single-valued linear correlation appears to exist between the fractional order and several of the hyperelastic

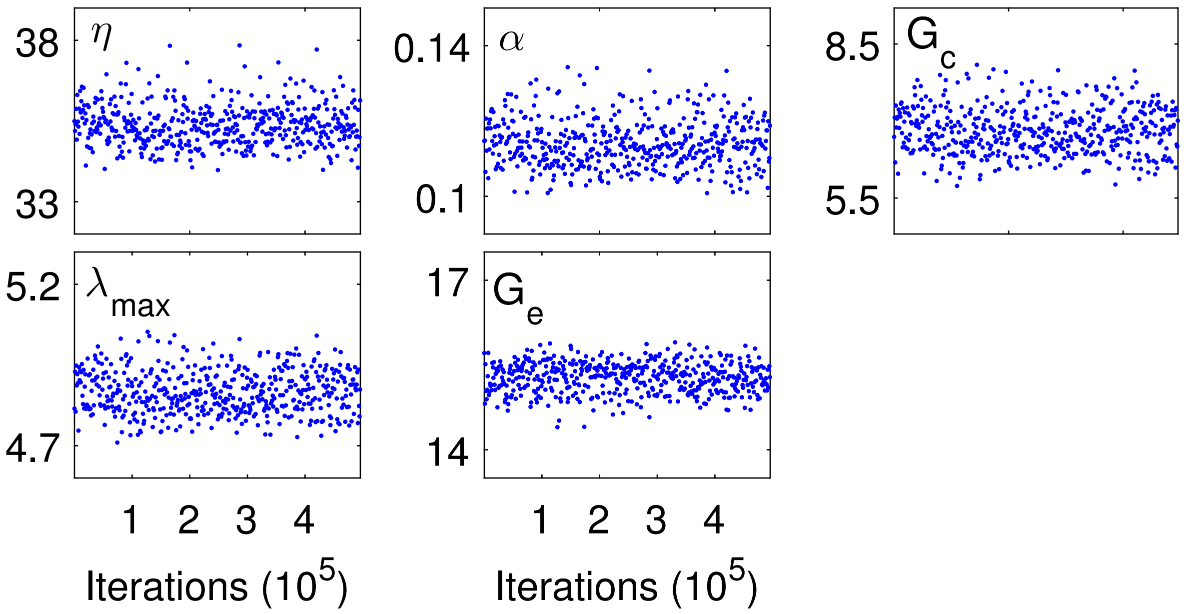

Figure 4.2: Parameter chains for calibration at slowest stretch rate with fractional order, linear viscoelastic model. The marginal posterior densities for each parameter appears to be stable.

parameters. Utilizing this relationship for model reduction requires further study, but it is useful in analyzing the current state of the model.

Bayesian methods are well suited for problems with non-identifiable parameters as standard optimization or frequentist techniques will generally fail as multiple parameters yield the same maximum likelihood. There are several ways to deal with this lack of identifiability. A physical analysis of the model may reveal a means by which to reformulate or reduce the model thereby eliminating the non-identifiable parameters. Often times this cannot be accomplished analytically, so an alternative approach is to choose physically acceptable nominal values for the non-identifiable parameters. We chose the latter approach for the hyperelastic parameters, G_c, λ_{max}, and G_e, by taking the mean value calibrated at the slowest stretch rate. We then used those values for subsequent validation studies at other deformation rates. The physical motivation behind using calibration values from the slowest rate is discussed in [50], but is simply understood by recalling from (3.1) that the hyperelastic energy function

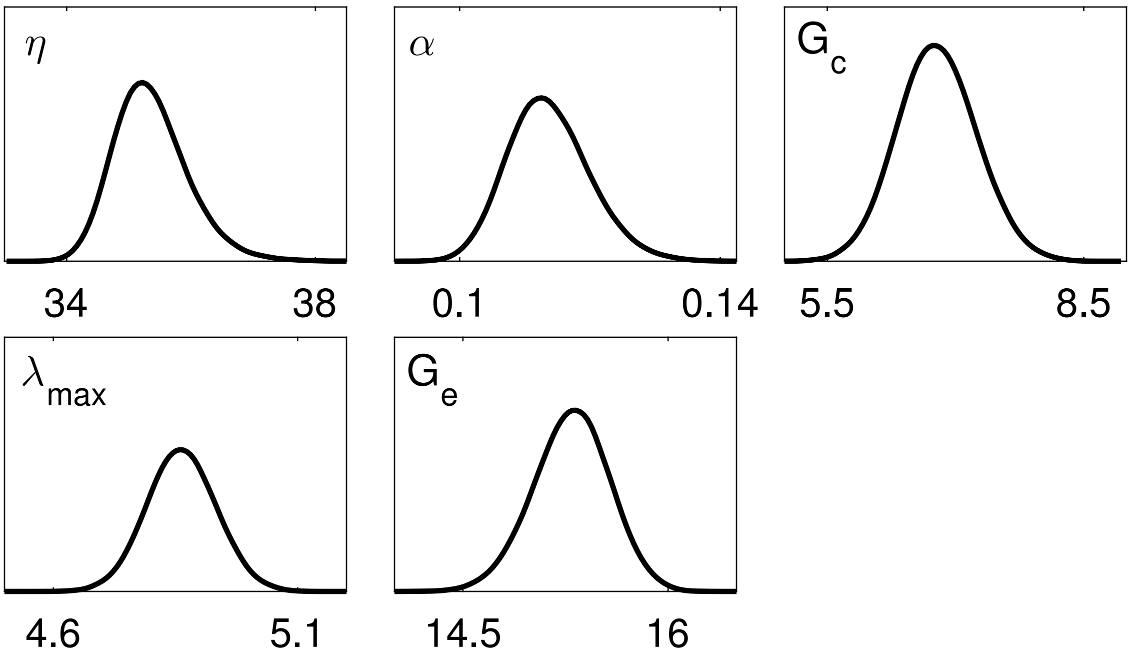

Figure 4.3: Marginal posterior densities for calibration at slowest stretch rate with fractional order, linear viscoelastic model.

should only depend on deformation and not its rate. In the case of the fractional order linear viscoelastic model, taking the nominal value as the mean is a reasonable assumption as the marginal posterior densities are approximately Gaussian as seen in Figure 4.3.

4.3.2 Model Calibration: Nonlinear Viscoelasticity

Similar analysis is performed with regard to the nonlinear viscoelastic model. We first attempted to calibrate the model parameters using the data collected at the slowest stretch rate. As seen in the chains in Figure 4.5, the sampling approach has difficulty identifying a stable posterior distribution. This particular problem involves seven different model parameters, which increases the complexity of the sampling space. Furthermore, at the slowest rate there is very little viscoelastic phenomena in comparison to higher rates. Because of this issue of identifiability, we have chosen nominal values for the hyperelastic parameter

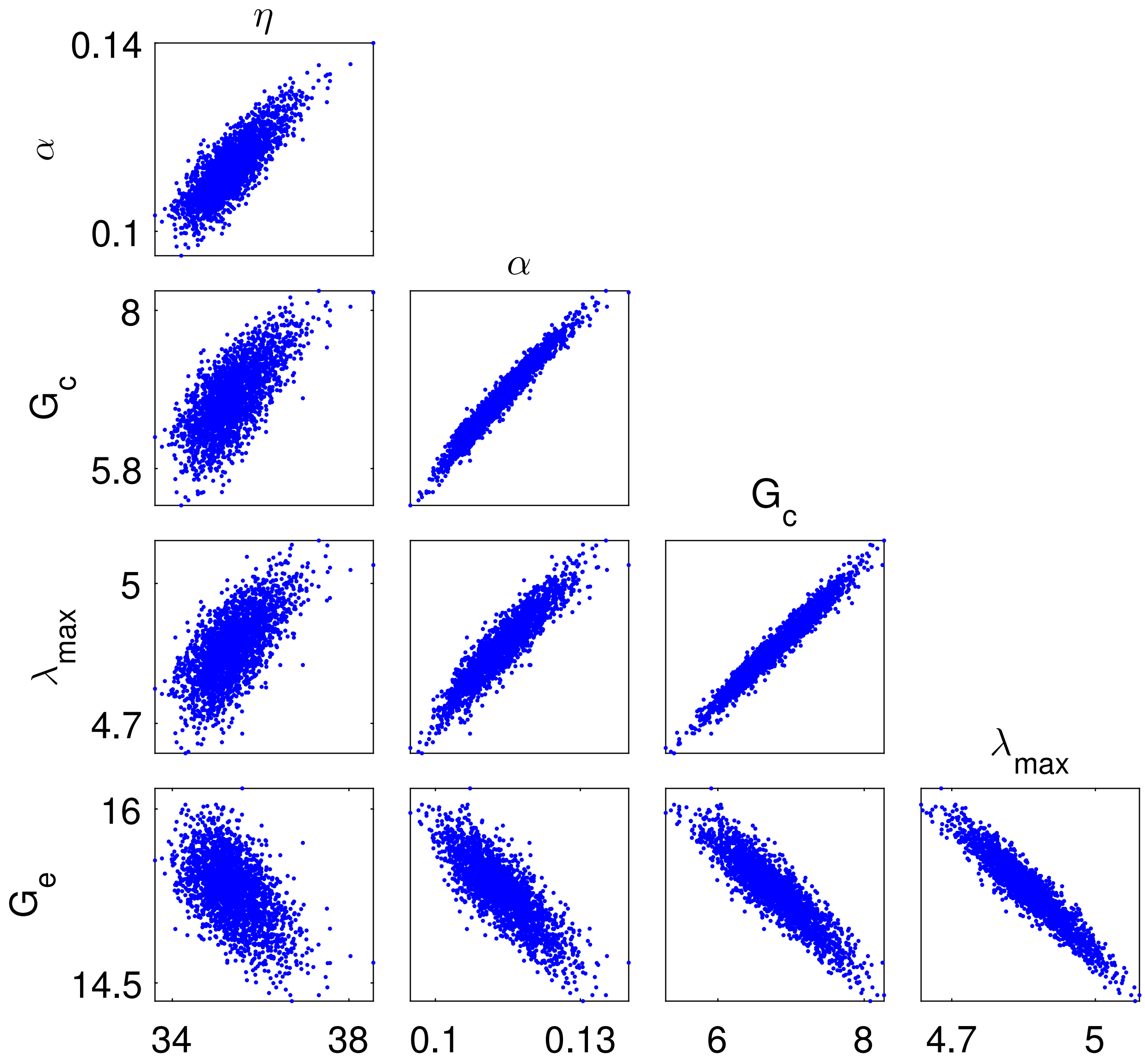

Figure 4.4: Pairwise correlation between each sampled parameter for calibration at the slowest stretch rate using the fractional order, linear viscoelastic model. A linear relationship is observed between several parameters. Every 200 sample points from chain taken for plotting.

values, and subsequently repeated model calibration at each rate to identify the viscoelastic components.

This analysis is very similar to the previous, but we instead consider one of the faster stretch rates. By calibrating at a faster rate, the amount of viscoelastic phenomena has

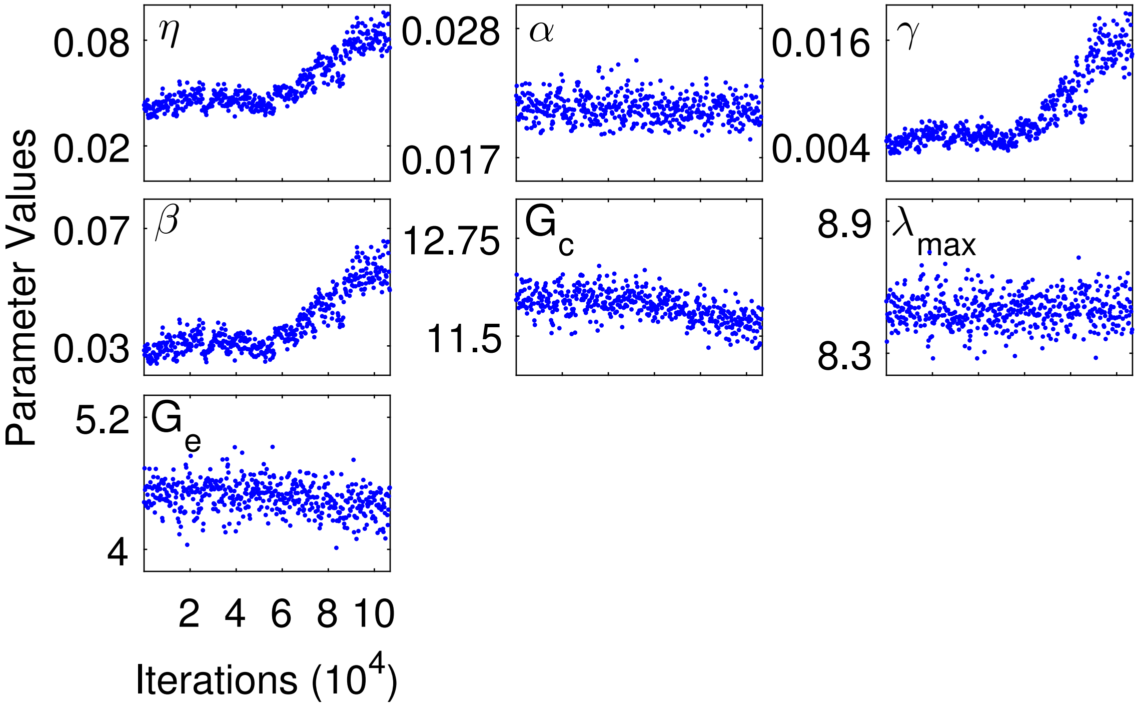

Figure 4.5: Parameter chains from MCMC sampling of $\dot{\lambda} = 6.7 \times 10^{-5}$ Hz data set. All model parameters were considered for this calibration.

increased, thereby making parameter identification easier. The chains as seen in Figure 4.6 have converged to the posterior densities (Figure 4.7). The pairwise correlation plot in Figure 4.8 indicates there may be some relationship between the fractional order, α, and the viscoelastic coefficients, η and γ. A global sensitivity analysis may help determine whether any actual relationship exists.

4.3.3 Model Prediction Procedure

The same procedure as outlined in Section 3.4.3 is used to asses the predictive capabilities of the fractional order viscoelastic model. Several calibration studies were highlighted in Sections 4.3.1 and 4.3.2. A different set of parameter distributions were identified by calibrating the model at each stretch rate separately. Uncertainty was propagated through the model to generate credible and prediction intervals, giving an estimate on the

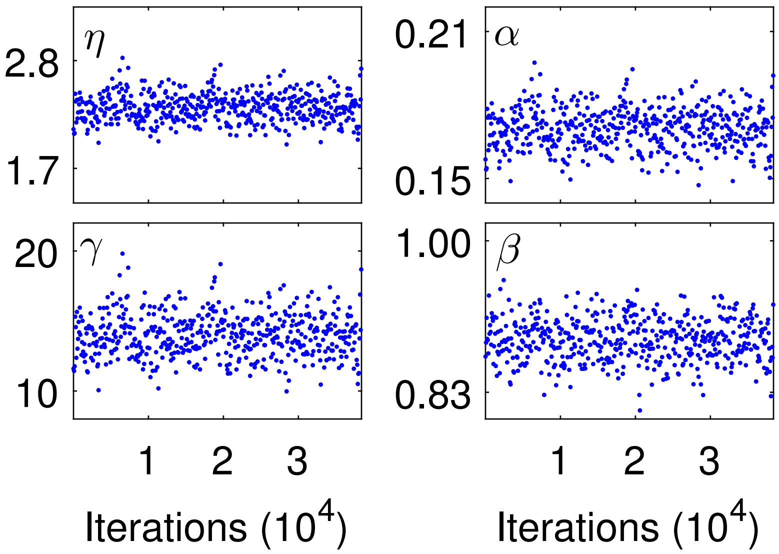

Figure 4.6: Chains from MCMC sampling of $\dot{\lambda} = 0.67$ Hz data set. Note hyperlastic parameters are set to nominal values.

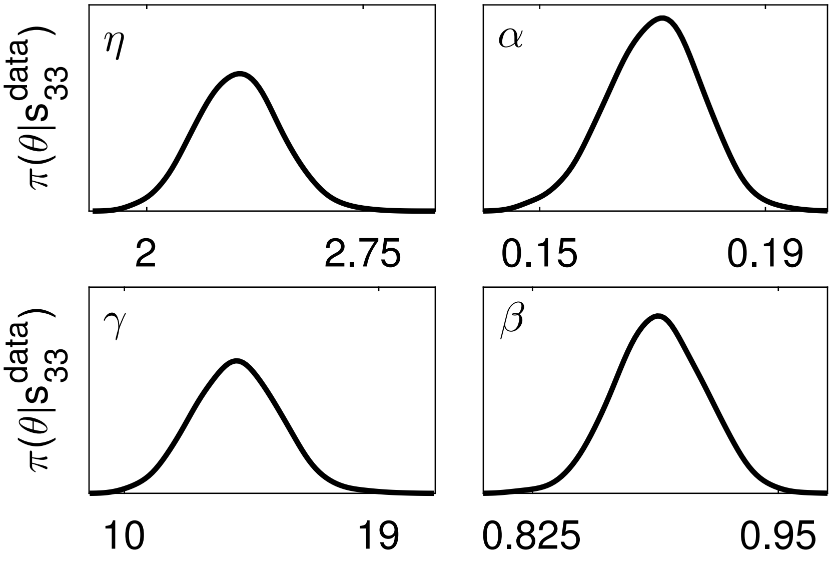

Figure 4.7: Marginal posterior densities from MCMC sampling of the $\dot{\lambda} = 0.67$ Hz data set. Note hyperlastic parameters are set to nominal values. Every 100 sample points from the chain are taken for plotting.

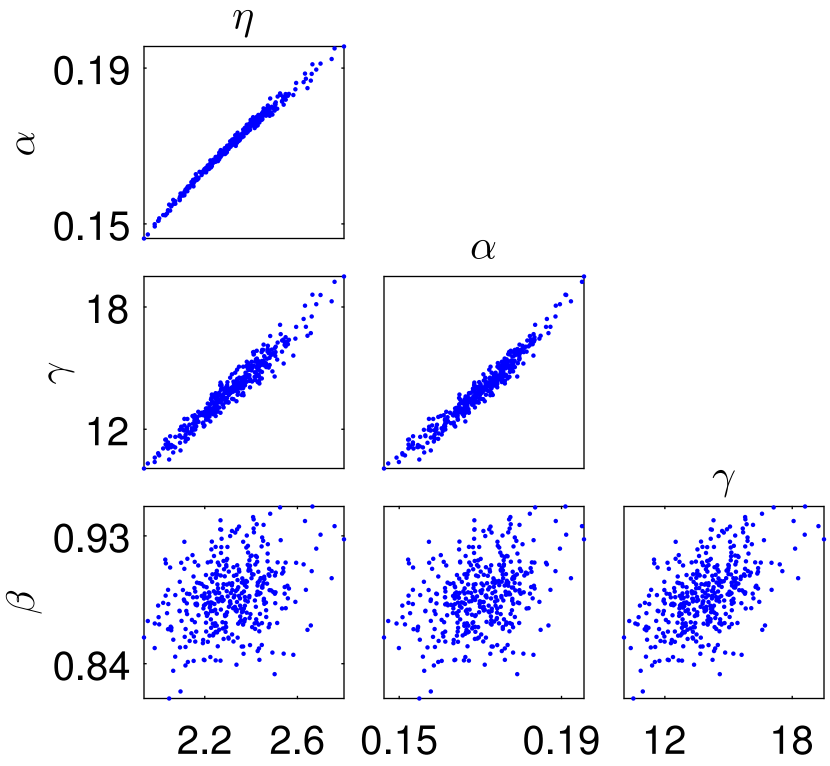

Figure 4.8: Pairwise correlation from MCMC sampling of the $\dot{\lambda} = 0.67$ Hz data set. Note hyperlastic parameters are set to nominal values. Every 100 sample points from the chain are taken for plotting.

amount of uncertainty there is in the output. The same error metric was used as before, $e_{mcmc} = \frac{1}{N}\sum(\sigma^{model} - \sigma^{data})^2$, where N is the number of data points, σ^{model} is the model stress, and σ^{data} is the stress measured experimentally. A summary of the error based on the calibration and predictions is given in Tables 4.1 and 4.2. Also, plots of the predicted model response across the range of rates tested are given for each model.

4.3.4 Model Prediction: Linear Viscoelasticity

The fractional order, linear viscoelastic model produces reasonable model predictions across all stretch rates as seen in Figure 4.9. A summary of the error between the model response and the data for the fractional order approach can be found in Table 4.1.

The first column in the table indicates the stretch rate data used to estimate the model parameters. The behavior at the other stretch rates is then predicted by using the distributions from the estimated parameters. As expected, the error is smallest when predicting the behavior at the stretch rate used to calibrate the parameter values (i.e., smallest error for the values along each column). The total error sums the individual errors along each row. As expected, a smaller error is obtained when calibrating at one of the median stretch rates.

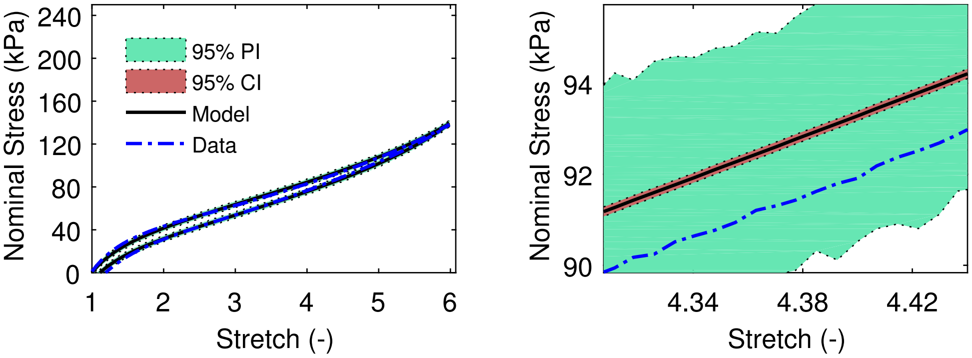

(a) 6.7×10^{-5} Hz (b) 6.7×10^{-5} Hz, Zoomed-In

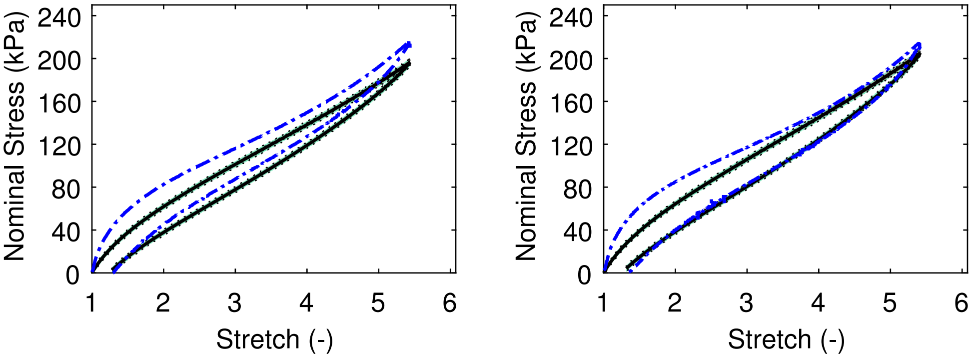

(c) 0.335 Hz (d) 0.67 Hz

Figure 4.9: Prediction of material behavior at nontrained boundary conditions using the fractional order linear viscoelastic model. The model was calibrated using $\dot{\lambda} = 6.7 \times 10^{-5}$ Hz. Error measurements are given in Table 4.1. Results not shown for $\dot{\lambda} = 0.0472, 0.10$ and 0.50 Hz. (b) Highlights 95% prediction (PI) and credible (CI) intervals.

4.3.5 Model Prediction: Nonlinear Viscoelasticity

As discussed in Section 4.3.2, identification of the viscoelastic parameters was easier when calibrating at faster stretch rates due to the sensitivity of the viscoelastic stress. With regard to predicting behavior at other rates, we find that the fractional order, nonlinear viscoelastic model produces reasonable model predictions across all stretch rates as seen in Figure 4.10.

A summary of the error between the model and the data can be found in Table 4.2. The statistics associated with the parameter sampling of the nonlinear model for the fractional order approach can be found in Table 4.3. It is important to observe the modeling errors in conjunction with the prediction plots seen in Figure 4.9 and Figure 4.10. While some of the error measurements are similar, the linear model clearly does not predict some of the nonlinear stress relations, especially in the case of finite deformation. Moreover, the total error is reduced using the fractional order model for all stretch rates considered in comparison with the integer order models presented in Chapter 3.

4.4 Conclusions

We have demonstrated the implementation of several viscoelastic models evaluated using fractional order derivative operations. The models were derived from thermodynamic

Table 4.1: Fractional Order Linear Viscoelastic: Model error (3.24) in units of kPa^2. Model evaluated using parameter distributions calibrated using the data specified in the first column. Mean value of parameter distributions is reported by $\bar{\theta}$. Nominal value of hyperelastic parameters: $G_c = 6.79$ kPa, $\lambda_{max} = 4.86$, and $G_e = 15.3$ kPa.

Calibrated			Predicted Rate ($1/s$)						Total
Rate (1/s):	$\bar{\alpha}$	$\bar{\eta}_L$	6.7×10^{-5}	0.0472	0.10	0.335	0.50	0.67	Error
6.7×10^{-5}	0.12	35.3	2.1	106	250	172	146	95	771
0.0472	0.10	27.3	9.5	11	36	645	640	459	1800
0.10	0.11	26.1	50.4	31	17	852	842	611	2403
0.335	0.12	41.3	14.4	339	618	55	54	130	1210
0.50	0.12	40.7	5.2	275	528	59	50	104	1021
0.67	0.14	39.6	34.4	95	259	131	95	64	678

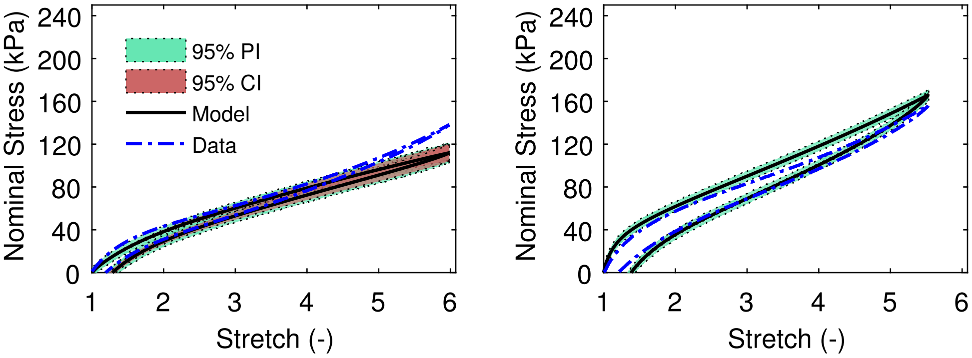

(a) $\dot{\lambda} = 6.7 \times 10^{-5}$ Hz (b) $\dot{\lambda} = 0.0472$ Hz

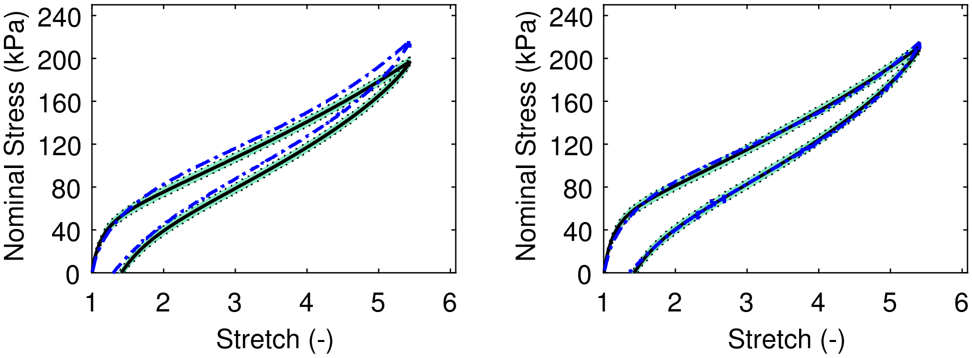

(c) $\dot{\lambda} = 0.335$ Hz (d) $\dot{\lambda} = 0.67$ Hz

Figure 4.10: Prediction of material behavior at nontrained boundary conditions using the fractional order nonlinear viscoelastic model. Model was calibrated using $\dot{\lambda} = 0.67$ Hz. Error measurements are given in Table 4.2.

principles within the context of fractal media [46]. These model formulations reduce to the fractional order representation shown in this chapter when considering non-fractal media. Each model was calibrated using Bayesian statistics, enabling the quantification of uncertainty of viscoelastic constitutive relations and error propagation. The calibration was performed using experimental data from the dielectric elastomer VHB 4910, which demonstrated significant rate-dependent deformation during uniaxial stress measurements.

In Chapter 3 it was shown that the nonlinear viscoelastic model yields better agreements with experimental data; however, the parameters identified during calibration were found to be rate-dependent. In this chapter we present the results of using fractional-order operators

Table 4.2: Fractional Order Nonlinear Viscoelastic: Model error in units of kPa^2. Model evaluated using parameter distributions calibrated using the data specified in the first column. Parameter statistics are given in Table 4.3.

Calibrated	Predicted Rate ($1/s$)						Total
Rate ($1/s$):	6.7×10^{-5}	0.0472	0.10	0.335	0.50	0.67	Error
6.7×10^{-5}	0.5	36.7	104	539	565	439	1685
0.0472	18.2	2.0	26.8	538	519	325	1428
0.10	39.2	20.2	3.3	766	733	454	2016
0.335	17.0	267	552	4.0	17.2	90.2	947
0.50	802	154	411	16.0	6.0	56.5	1445
0.67	88.9	56.2	199	95.6	62.0	5.8	508

Table 4.3: Fractional Order Nonlinear Viscoelastic: Model parameter means ($\bar{\theta}$) and standard deviations (σ_θ). Nominal value of hyperelastic parameters: $G_c =$ 11.88 kPa, $\lambda_{max} = 8.50$, and $G_e = 4.47$ kPa.

Calibrated	η		α	
Rate ($1/s$):	$\bar{\eta}$	σ_η	$\bar{\alpha}$	σ_α
6.7×10^{-5}	5.58×10^{-2}	4.90×10^{-3}	2.11×10^{-2}	8.99×10^{-4}
0.0472	1.98	0.21	0.14	1.27×10^{-2}
0.10	3.06	0.19	0.28	1.29×10^{-2}
0.335	2.48	0.17	0.14	8.25×10^{-3}
0.50	0.50	4.97×10^{-2}	6.64×10^{-2}	5.53×10^{-3}
0.67	2.32	0.14	0.17	8.24×10^{-3}

Calibrated	γ		β	
Rate ($1/s$):	$\bar{\gamma}$	σ_γ	$\bar{\beta}$	σ_β
6.7×10^{-5}	7.48×10^{-3}	1.35×10^{-3}	3.78×10^{-2}	3.22×10^{-3}
0.0472	13.9	2.03	0.66	1.20×10^{-2}
0.10	33.2	2.09	0.84	1.70×10^{-2}
0.335	15.5	1.75	0.96	1.72×10^{-2}
0.50	0.5	0.10	0.26	2.26×10^{-2}
0.67	14.0	1.52	0.89	2.26×10^{-2}

within the model. It was found that the fractional-order approach for both linear and nonlinear viscoelastic models yields parameters that provide better predictions on uncalibrated data. The fractional order, α, represents a scaling on the deformation rate, which is believed to be material dependent. In the future, this analysis could be repeated by collecting experimental data from different materials to provide further insight into the fractal nature of elastomers.

CHAPTER 5

ELECTROMECHANICS OF SOFT ELASTOMERS

5.1 Introduction

The novel electrostrictive properties of dielectric elastomers provide opportunities for development of a broad range of soft actuators, self-sensing systems, and energy harvesting devices [2]. Their constitutive properties afford giant field induced deformation greater than 100% strain [89]. These soft materials can be designed into large deformable membranes that have distinct advantages in the development of a broad range of soft robotic actuators and sensors. One example is the iSPRAWL legged robot which uses passive hyperelastic tubing coupled to actuation mechanisms that produced one of the fastest open-loop controlled hexapod running robots [37]. Dielectric membrane materials offer a route towards novel robotic motion as well as a variety of other soft actuator based devices [43]; however, accurate, robust, and numerically efficient constitutive model predictions are necessary to design and reliably control these active structures.

Once these elastomers are implemented within an adaptive structure, it becomes important to understand how to control various properties of the material. For example, it is often desirable to apply a field through these membranes in order to decrease the pre-tension, as is the case on the iSprawl robotic platform. Using smart materials in the robot construction shows potential for enhancing the performance of the device on multiple terrains [37]. Typical components do not perform optimally from one surface to another, but with dynamic tuning via variable stiffness (via electrostriction) in the robotic legs, this obstacle could be addressed. To accomplish this task, one must understand the electrostrictive response of the material.

Prior research has shown how a non-affine hyperelasticity function provides reasonable prediction of uni-axial deformation of the dielectric elastomer VHB 4910 made by 3M [50,55]. The hyperelastic behavior of this modeling framework assumes only a fraction of the polymer chains move proportional to the macroscopic boundary displacements [15]. In the previous analysis by [50], model comparisons to data were conducted on uniaxial stress-stretch curves over a range of stretch rates at zero electric field. Here, transverse mechanical loading, dielectric behavior, and electrostrictive coupling of a pre-stretched membrane is included in the analysis to gain more insight on the electromechanical constitutive model assumptions, its predictive capability, and the uncertainty of electromechanical model parameters. For the purpose of reduced order modeling, we assume a homogeneous deformation throughout the membrane, which allows for simplification of the model to an algebraic expression. With the mindset of implementing a structural model onto a platform that requires numerically efficient control algorithms, a simple algebraic model is ideal. However, in light of the uncertainty associated with the electromechanical models, it is important to determine whether the assumptions made to simplify the problem neglect important physical and structural properties. This will be addressed in our discussion on future work in Section 5.5.

Considerable research has been done on identifying the dielectric constant for these types of materials [38, 82, 88]. Interpreting the constitutive behavior in light of uncertainty is important and has often been neglected in materials and mechanics research until recently [34, 54]. Testing of the material on the design platform reveals a non-trivial relationship between the material's dielectric properties and the deforming motion of the structure.

The remainder of this chapter will be broken into the following components. Section 5.2 focuses on explaining the experimental setup and procedure, and Section 5.3 introduces the theoretical model development for both phenomena under consideration. The uncertainty analysis is presented in Section 5.4 and concluding remarks are provided in Section 5.5.

5.2 Experimental Setup

The structure used to take advantage of electrostriction consists of a membrane or a set of stacked membranes with a perforated center hole for the "bone" of the leg. As the bone is connected to the soft electroactive elastomer this allows for efficient transmittal of forces to the ground whether walking or running. A schematic of this design can be seen in Figure 5.1. Several different experimental procedures can be performed on this platform. The non-deformed configuration can be seen in Figure 5.2(a). Electrodes are placed on either side of the membrane allowing for application of an electric field. Additionally, a transverse load can be applied to the center ring as seen in Figure 5.2(b), which has been considered previously in a spring loaded configuration [69]. This representation assumes a homogeneous profile through the radius of the membrane, but this is simply an approximation. In reality, the membrane will deform in an inhomogeneous manner, which will be discussed more later. In light of the complexities associated with this structure, the analysis of the loading is broken into several components.

Two different experiments were performed on the same adaptive structure[1]. The first experiment measured the load in response to being transversely displaced in conjunction with electromechanical loading from an applied field. The second experiment placed the undeformed structure in a Sawyer-Tower circuit and measured the electric displacement under different applied fields. Both experiments are described in detail in Sections 5.2.1 and 5.2.2, respectively.

5.2.1 Transverse Load - Displacement

The dielectric elastomer VHB 4910 was bi-axially pre-stretched to three times its original size ($\lambda_{pre} = 3$) and adhered to a circular acrylonitrile butadiene styrene (ABS) plastic ring with a diameter of 20.5 mm (see Figure 5.1). An inner ring with diameter 5.63 mm was placed in the center of the ring for applying transverse loading (F in Figure 5.2b). An MTS load frame was used to monitor changes in the load for a prescribed displacement ranging from 0 to 6 mm. The displacement was applied along a triangular load/unload displacement profile at a constant speed of 1.41 mm/s ($d\delta/dt$).

During the transverse load/unload cycle, the nominal electric field was fixed at values ranging from 0 to 63 MV/m, based on the pre-stretch thickness of 1/9 mm for VHB 4910

---

[1] The experimental data collection for this project was performed by Wei Gao and Adriane Moura.

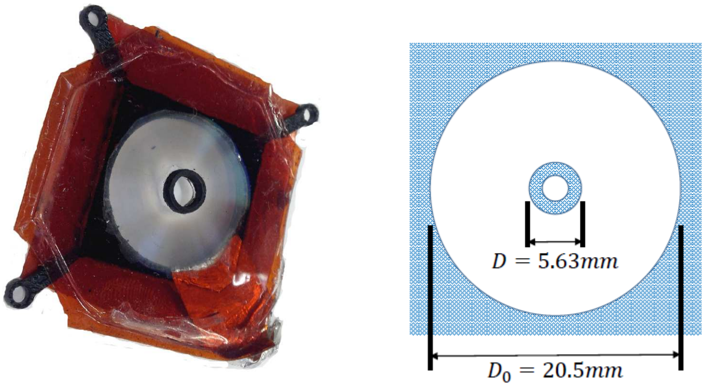

(a) Adaptive structure (b) Overhead view schematic

Figure 5.1: (a) Elastomer is stretched over acrylonitrile butadiene styrene (ABS) plastic frame and electrically isolated for electrode application. (b) Top view of experimental setup.

under a pre-stretch of 3. The nominal electric field is defined in the undeformed configuration where the membrane thickness is 1/9 mm. All electrostatic and quasi-static electrical tests were conducted using a Trek linear amplifier that has a maximum voltage of 10 kV and maximum current of 40 mA. Carbon grease was used as the compliant electrode, which was required in all electrostatic experiments to apply the electrical loads. The increase in electrostatic field results in a reduction of the effective stiffness due to electrostrictive coupling. A representative set of data from this experiment is shown in Figure 5.3(a). Hysteresis is clearly present, which indicates there is some viscoelastic components to the stress response. For the purpose of the analysis presented here, however, we will focus on the loading part of the cycle, as shown in Figure 5.3(b), and ignore viscoelastic effects.

5.2.2 Electric Displacement - Electric Field

Measurement of the dielectric constant is also conducted using electric displacement-electric field cycles (D-E cycles) by applying sinusoidal fields at a frequency of 1 Hz. These experiments were conducted in the same configuration as the un-deformed transverse load/unload experiments. The membranes were again stretched to $\lambda_{pre} = 3$ such that the thickness is approximately 1/9 mm assuming incompressible deformation. The membranes were tested in a Sawyer-Tower circuit and the voltage drop was measured across a known capacitor of

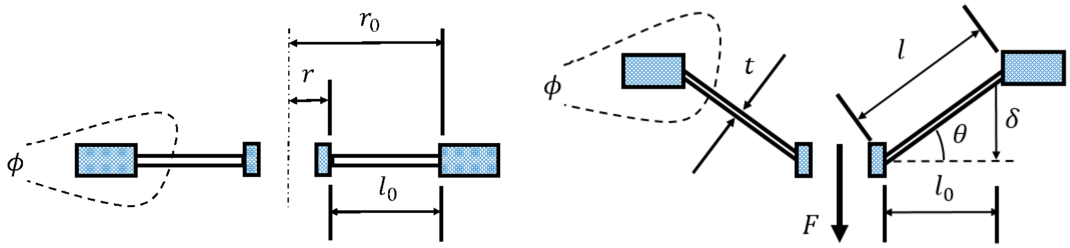

(a) Un-deformed configuration (b) Deformed in transverse direction

Figure 5.2: Cross section illustration of the membrane structure. The structure is loaded along the surface of the center ring. The load is denoted by F and is applied in the transverse direction. Inhomogeneous deformation along l is neglected in the reduced-order model.

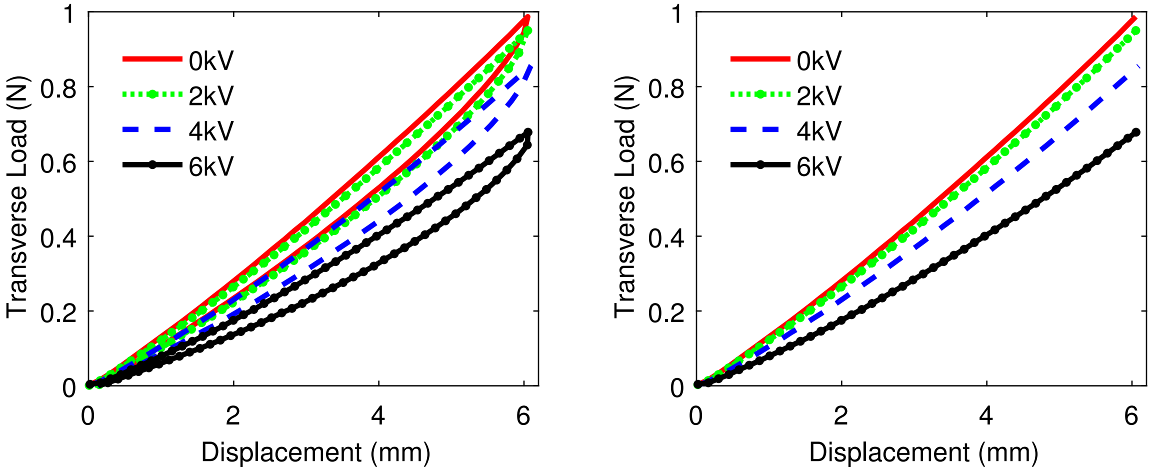

(a) Complete Cycle (b) Loading

Figure 5.3: (a) Measured transverse load during complete experimental cycle under different applied fields. Additional data sets at 1 kV, 3 kV, and 5 kV are not shown for clarity. (b) Measured transverse load during *loading* of specimen.

153 μF [42]. The voltage across the capacitor was monitored using a Keithley 6517A electrometer to determine the charge and electric displacement as a function of the applied field. Each specimen was cycled at least five times such that steady state hysteresis is established, and subsequent analysis is performed on the steady state values. For a pre-stretch of 300%, the range of maximum electric fields tested range from 9 MV/m to 54 MV/m. Note the maximum electric field is based on the amplitude of the applied sinusoidal field, so an amplitutde of 6 kV with 300% pre-stretch corresponds to 54 MV/m. Several example data sets

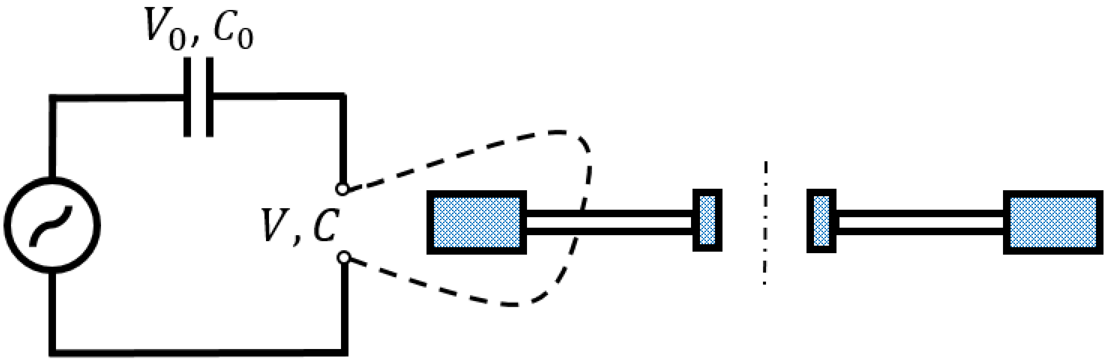

Figure 5.4: Sawyer-Tower circuit with VHB in series with $C_0 = 153\ \mu F$. VHB specimen shown in non-deformed configuration.

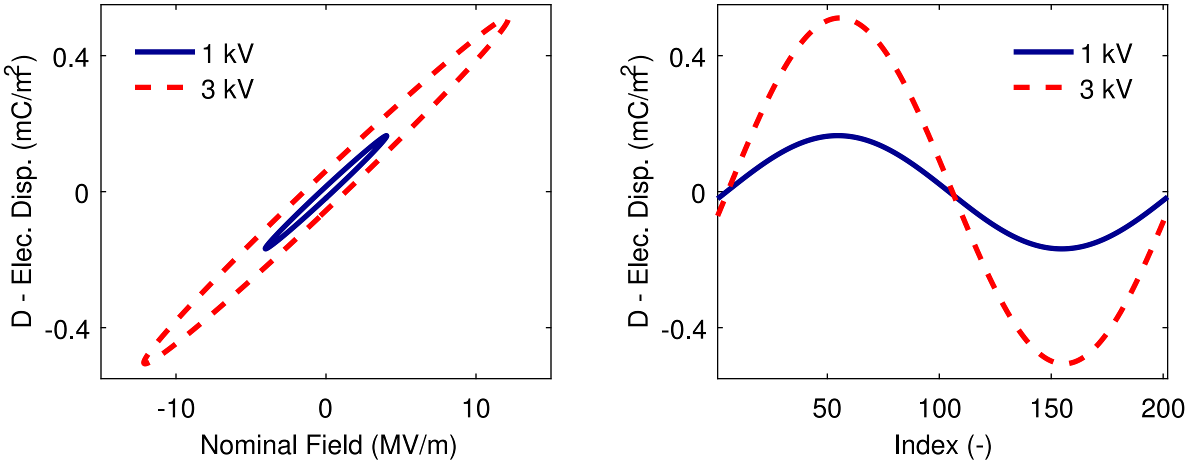

(a) Electric Displacement vs. Electric Field (b) Electric Displacement vs. Index

Figure 5.5: Data collected from Sawyer-Tower circuit. (Left) Electric displacement plotted as a function of the nominal field and (Right) electric displacement as a function of index from a single loop.

are shown in Figure 5.5. This results in a direct measure of the dielectric behavior which will be compared to electrostrictive stresses which are typically proportional to the dielectric constant [47, 88]. The Sawyer-Tower measurements also provide a measure of the dielectric losses due to dielectric hysteresis.

Modeling this behavior is non-trivial, which is highlighted by observing the complex relationship between the different loading components. As seen in Figure 5.6(a), the measured

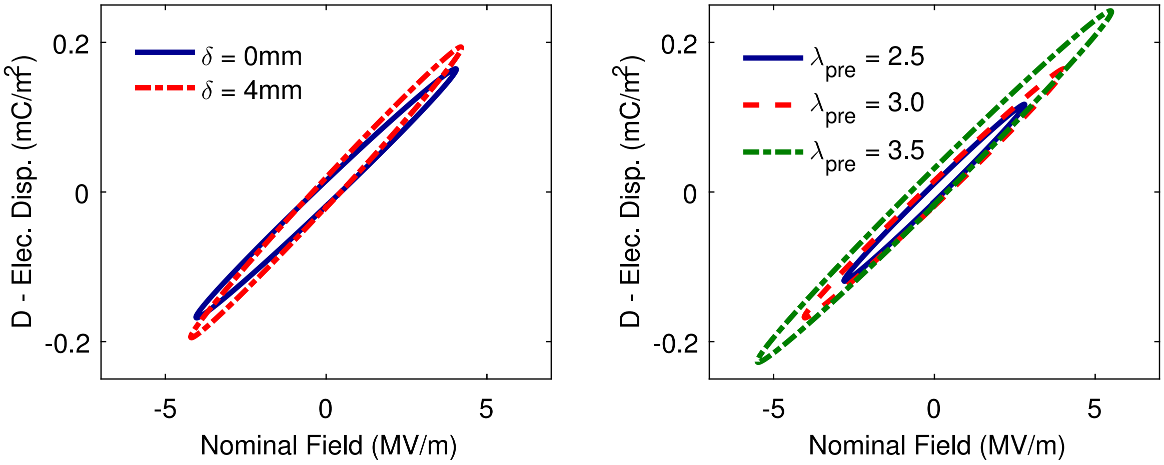

(a) Transverse loading

(b) Pre-stretch

Figure 5.6: (a) Slope of D-E hysteresis cycle has changed due to application of transverse load. (b) Negligible variations in slope are observed by adjusting the amount of pre-stretch.

electric displacement in response to the applied field is affected by the deflection of the robotic leg. Furthermore, the slope of these cycles reflects the material's permittivity, which shows the uncertainty in this property as a result of deformation from transverse loading of the membrane. It is also observed in Figure 5.6(b) that the amount of pre-stretch has a negligible impact on the material's permittivity. Based on these observed experimental responses, we will investigate the affect of transverse displacement on the dielectric permittivity in subsequent analysis.

5.3 Theory

The modeling framework consists of nonlinear membrane electromechanics and a rate-dependent dielectric model that quantifies stored and dissipative electric energy transfer. We first summarize the hyperelastic membrane mechanics and then introduce a dynamic equation that accommodates dielectric hysteresis.

5.3.1 Transverse Load - Displacement

Following Rizzello et al. [69], a simplified force-displacement constitutive relation can be determined from a force balance between the applied load and the forces generated within the dielectric elastomer membrane. Neglecting inhomogenous deformation, the transverse force normal to the undeformed membrane plane is given by

$$F = 2\pi \sin(\theta) r t \sigma_l \tag{5.1}$$

where r is the radius of the inner ring, t is the true thickness of the membrane, and σ_l is the radial Cauchy stress. We focus on quasi-static deformation processes which requires a relation between the transverse displacement and the geometry of the membrane using

$$\begin{aligned} l &= \sqrt{l_0^2 + \delta^2} \\ \sin(\theta) &= \frac{\delta}{l} \end{aligned} \tag{5.2}$$

where the geometric parameters are illustrated in Figure 5.2. The experimentally measured transverse displacement is δ, the radial distance between the inner and outer rings is denoted l_0, and the instantaneous longitudinal length of the membrane is l.

Two deformation processes are considered. First, the membrane is bi-axially pre-stretched. It is then transversely loaded resulting in additional radial stretch and reduction in thickness. For a given direction, the total stretch is divided into the pre-stretch and stretch during transverse loading using the relation

$$\lambda_{i,tot} = \lambda_{i,pre} \lambda_i \tag{5.3}$$

where the subscripts are $i = l, c$ or t for the radial, circumferential, and thickness directions, respectively. The deformation processes are all incompressible, so the following constraints are applied

$$\begin{aligned} \lambda_{l,pre} \lambda_{c,pre} \lambda_{t,pre} &= 1, \quad \text{(Bi-Axial Pre-Stretching)} \\ \lambda_l \lambda_c \lambda_t &= 1, \quad \text{(Transverse Loading)} \\ \lambda_{l,tot} \lambda_{c,tot} \lambda_{t,tot} &= 1. \quad \text{(Total Deformation)} \end{aligned} \tag{5.4}$$

The first process is done by stretching the membrane in the radial and circumferential directions to three times their initial lengths. As stretch is simply a measure of the current length divided by the original length, we can make the following conclusions about the stretches during bi-axial pre-stretching

$$\lambda_{l,pre} = \lambda_{c,pre} = 3 \implies \lambda_{t,pre} = 1/9. \tag{5.5}$$

An additional kinematic constraint is imposed by the axis-symmetric geometry. During transverse loading, the deformation in the circumferential direction is zero requiring $\lambda_c = 1$. The incompressiblity constraint in (5.4) provides the additional relation $\lambda_t = \lambda_l^{-1}$. The stretch in the radial direction can be related to the transverse displacement by substituting (5.2) into the definition for stretch

$$\lambda_l = \frac{l}{l_0} = \frac{\sqrt{l_0^2 + \delta^2}}{l_0} = \sqrt{1 + \left(\frac{\delta}{l_0}\right)^2}. \tag{5.6}$$

The Cauchy stress can be determined from the stretch by introducing a hyperelastic and dielectric energy density function. It is assumed that the membrane can be described by a hyperelastic energy function and a linear dielectric energy density [88]. This energy density function per reference volume is

$$\widetilde{\psi} = \widetilde{\psi}_H + \widetilde{\psi}_D, \tag{5.7}$$

where $\widetilde{\psi}_H$ is the hyperelastic energy function, and $\widetilde{\psi}_D$ is the dielectric energy density. The Cauchy stress is found from (5.7),

$$\sigma_{ij} = J^{-1} F_{jK} \frac{\partial \widetilde{\psi}}{\partial F_{iK}} = J^{-1} F_{jK} \left(\frac{\partial \widetilde{\psi}_H}{\partial F_{iK}} + \frac{\partial \widetilde{\psi}_D}{\partial F_{iK}} \right) = \sigma_{ij}^H + \sigma_{ij}^D. \tag{5.8}$$

where F_{iK} is the deformation gradient [45] and $J = \det F_{iK}$ is the Jacobian. Before evaluating this, we must first define our energy density functions.

A non-affine hyperelastic energy function has shown comparable model predictions relative to a six parameter Odgen model in uni-axial model fits based on prior Bayesian statistical analysis [50]. The non-affine model requires half as many parameters relative to the Ogden model and is therefore implemented here. Details on the theoretical motivation for this model is given by Davidson and Goulbourne [15] and numerical analysis and experimental correlation is given by Miles et al. [50]. The hyperelastic energy function is

$$\widetilde{\psi}_H = \frac{1}{6} G_c I_1 - G_c \lambda_{max}^2 \ln(3\lambda_{max}^2 - I_1) + G_e \sum_j \left(\lambda_j + \frac{1}{\lambda_j} \right) \tag{5.9}$$

where G_c is the crosslinked network modulus, G_e describes the plateau modulus, λ_{max} is the maximum stretch of the effective affine tube, and $I_1 = \lambda_i \lambda_i$ is the first stretch invariant where summation on i is implied. Note the deformation can be described in terms of the principal stretches, so the hyperelastic stress in the principal directions can be found by the relation

$$\sigma_i^H = \lambda_{i,tot} \frac{\partial \widetilde{\psi}_H}{\partial \lambda_{i,tot}}. \tag{5.10}$$

Recall from (5.1) that we are interested in determining the stress along the radial direction, so the hyperelastic stress in the radial direction is found to be

$$\begin{aligned} \sigma_l^H &= J^{-1} F_{jK} \frac{\partial \widetilde{\psi}_H}{\partial F_{iK}} = \lambda_{l,tot} \frac{\partial \widetilde{\psi}_H}{\partial \lambda_{l,tot}} \\ &= \frac{1}{3} G_c \left(\lambda_{l,tot}^2 - \frac{1}{\lambda_{c,pre}^2 \lambda_{l,tot}^2} \right) \left(\frac{9\lambda_{max}^2 - I_1}{3\lambda_{max}^2 - I_1} \right) \\ &+ G_e \left(\lambda_{l,tot} \left(1 + \lambda_{c,pre}\right) - \frac{1 + \lambda_{c,pre}}{\lambda_{c,pre} \lambda_{l,tot}} \right). \end{aligned} \tag{5.11}$$

The last component that we must define is the dielectric energy density. We implement a linear dielectric energy density function of the form

$$\widetilde{\psi}_D = \frac{F_{iK} F_{iL}}{2J\kappa} \widetilde{D}_K \widetilde{D}_L \tag{5.12}$$

where κ is the deformation independent dielectric permittivity constant, and $\widetilde{D}_K$ is the nominal electric displacement [88]. Note the dielectric permittivity is $\kappa = \kappa_r \epsilon_0$, where κ_r is the relative permittivity and ϵ_0 is the permittivity of free space. The nominal electrostrictive stress relates to the energy density function by

$$s_{jB}^D = \frac{\partial \widetilde{\psi}_D}{\partial F_{jB}} = \frac{J^{-1}}{2\kappa} \left(-H_{jB} F_{iK} F_{iL} + \delta_{ij} \delta_{KB} F_{iL} + F_{iK} \delta_{ij} \delta_{LB} \right) \widetilde{D}_K \widetilde{D}_L. \tag{5.13}$$

The true and nominal electric displacement are related by $D_i = J^{-1}F_{iK}\widetilde{D}_K$. The Cauchy electrostrictive stress is found by substituting the relationship between true and nominal electric displacement and also by multiplying by $J^{-1}F_{iK}$, yielding

$$\sigma_{ij}^D = J^{-1}F_{iB}s_{jB}^D = \frac{1}{2\kappa}\left(-\delta_{ij}D_aD_a + 2D_iD_j\right). \tag{5.14}$$

As a final step, we desire to express the model in terms of the true electric field, which is related to the electric displacement by $D_i = \kappa E_i$. This results in the well known electrostrictive stress tensor [47,88]

$$\sigma_{ij}^D = \kappa\Big(E_iE_j - \frac{1}{2}E_kE_k\delta_{ij}\Big). \tag{5.15}$$

For the problem in question, the only nonzero field is in the thickness direction. We can analyze this in terms of principal directions, so we find the radial electrostrictive Cauchy stress is

$$\sigma_l^D = -\frac{\kappa}{2}E_t^2 \tag{5.16}$$

where E_t is the true field in the thickness direction, and κ is the dielectric permittivity constant. The nominal field ($\widetilde{E}_t$) is related to the true field by $E_t = \lambda_{t,tot}^{-1}\widetilde{E}_t$. The coupling is based on nonlinear geometric effects which lead to an electrostrictive stress that is similar to Maxwell's stress in a vacuum except the permittivity coefficient is replaced by the permittivity of the dielectric elastomer [47,88].

In summary, the Cauchy stress in the radial direction is

$$\sigma_l = \sigma_l^H + \sigma_l^D \tag{5.17}$$

where σ_l^H is defined in (5.11) and σ_l^D is defined in (5.16). Note that this model neglects the viscoelastic hysteresis illustrated in Figure 5.3. The additional effect of viscoelasticity is described elsewhere [50]. The Cauchy stress calculated in (5.17) is inserted into the transverse force relation described in (5.1). We can then compare the model with the experimentally measured transverse load (F^{data}).

5.3.2 Electric Displacement - Electric Field

The *D*-*E* loops acquired through low frequency electrometer measurements are compared to a dielectric model to provide additional support for identification of the dielectric constant and comparisons with electrostriction. The model can be derived from a Lagrangian density that takes into account vacuum field energy, conserved electronic structure energy, and dissipation [19, 51]. To simplify the analysis, we relate the true electric displacement and electric field components in the thickness direction since all dielectric measurements are applied from a zero transverse displacement boundary condition. This is because the thickness is constant assuming incompressible deformation.

The rate-dependent dielectric constitutive model is in terms of polarization as the order parameter and given by

$$\ddot{P}_t + \gamma \dot{P}_t + \frac{K}{m} P_t = \frac{Ne^2}{m} E_t \tag{5.18}$$

where P_t is the polarization in the thickness direction in the deformed configuration; see [19, 51]. This model includes photonic bandgap and frequency dependent optical absorption effects by the inclusion of the second order time derivative on polarization in $\ddot{P}_t$. We neglect second order rate effects as all data was collected under quasi-static sinusoidal fields. Dissipation is governed by the material parameter γ while the remaining constitutive parameters K, m, N, and e govern the conserved dynamic behavior and dielectric behavior [19]. These parameters are simplified into a time constant and static dielectric constant using the following methodology.

The true electric displacement is related to the polarization and applied field according to

$$D_t = \epsilon_0 E_t + P_t \Longrightarrow P_t = D_t - \epsilon_0 E_t. \tag{5.19}$$

Applying the assumption that second order rate effects are negligible to (5.18) yields,

$$\gamma \dot{P}_t + \frac{K}{m} P_t = \frac{Ne^2}{m} E_t \ , \tag{5.20}$$

and substituting 5.19 into (5.20) gives

$$\gamma (\dot{D}_t - \epsilon_0 \dot{E}_t) + \frac{K}{m} (D_t - \epsilon_0 E_t) = \frac{Ne^2}{m} E_t. \tag{5.21}$$

We can rearrange the expression such that the true electric displacement is isolated on the left hand side of the equation,

$$\gamma \dot{D}_t + \frac{K}{m} D_t = \gamma \epsilon_0 \dot{E}_t + \Big(\frac{K}{m} \epsilon_0 + \frac{Ne^2}{m} \Big) E_t. \tag{5.22}$$

Dividing both sides by K/m and pulling ϵ_0 out in the final term on the right hand side gives us

$$\frac{\gamma m}{K} \dot{D}_t + D_t = \frac{\gamma m}{K} \epsilon_0 \dot{E}_t + \Big(1 + \frac{Ne^2}{K \epsilon_0} \Big) \epsilon_0 E_t. \tag{5.23}$$

Finally, we can simplify this expression by defining

$$\tau_D = \frac{\gamma m}{K} \; , \qquad \kappa_r = 1 + \frac{Ne^2}{K \epsilon_0} \tag{5.24}$$

where τ_D is a time constant and κ_r is the relative dielectric permittivity. Giving us the final governing equation

$$\tau_D \dot{D}_t + D_t = \tau_D \epsilon_0 \dot{E}_t + \kappa_r \epsilon_0 E_t \tag{5.25}$$

where $\kappa = \kappa_r \epsilon_0$ is the dielectric permittivity as given in (5.12) and κ_r is the relative dielectric permittivity. Note that due to incompressibility and the membrane geometry, the thickness of the membrane is constant during application of the field as long as the membrane does not deform under its own weight and does not wrinkle. The electric field in (5.18) is based on the applied voltage divided by the pre-stretched thickness which is approximately 1/9 mm for VHB 4910 under a pre-stretch of 3. The nominal field is subsequently different when considering other amounts of pre-stretch. It is assumed that the thickness remains constant after pre-stretching.

5.4 Uncertainty Analysis

5.4.1 Electromechanical Parameter Estimation

The theory outlined in Section 5.3 is used to calibrate model parameters associated with hyperelastic and electrostrictive membrane mechanics. To implement the model, we first considered the experimental case in which no voltage was applied to the membrane. This was done in order to calibrate the hyperelastic model parameters found in (5.9). Sampling was performed on the hyperelastic parameters as there was no applied voltage and subsequently no electrical contribution from which to identify the relative permittivity. To highlight the uncertainty associated with experimental variability, we performed the calibration using multiple data sets in which no voltage was applied. The data sets were taken for specimens tested under the same conditions, so in addition to zero voltage, each specimen had the same pre-stretch and no deflection in the transverse direction. This was done in the MCMC algorithm by evaluating $F(i;\theta)$ for each data set, calculating the sum-of-squares, and then adding each of them to find an overall error measure. Each error measure from an individual set was weighted equally so that no experiment was considered more important than another. Using this methodology and this subset of data, our first step required calibrating the following parameters

$$\theta = [G_c, G_e, \lambda_{max}] \ . \tag{5.26}$$

The hyperelastic stress is a function of the deformation and these parameters are assumed independent of the applied field. Therefore, the results found from the initial calibration were used for subsequent analysis, i.e., the mean value of the parameter chain was inserted into the model and assumed to be deterministic. Choosing a nominal value for what was a random variable opens up several questions, which will be discussed later.

With fixed hyperelastic parameters, calibration was subsequently performed on the relative dielectric permittivity,

$$\theta = [\kappa_r] \tag{5.27}$$

to determine electrostrictive coupling. To calibrate this parameter, we considered a different subset of the data. We can use the same specimens from which we calibrated the hyperelastic parameters, but in this instance we will consider data sets in which there was an applied field. Each data set was weighted equally such that no experiment was considered more important than another.

Performing parameter estimation using multiple datasets with different independent variables (i.e., different electrostatic fields) is a challenge. As we have discussed above, one can simply include all the data and weight each case similarly; however, it is of interest to see how much the value of these parameters differ when considering each field level individually. Furthermore, in order to test the predictive capability of one's model, it is beneficial to apply parameter results from one experiment and predict the results of another independent measurement. We calibrated parameters using the same approach described above, except we determined the value of κ_r from only one data set or a smaller data subset, and assessed predictions for other data sets not used in the parameter estimation. An example of this would be to calibrate κ_r using all the non-zero field cases for specimen 1, then use the resulting posterior density in our predictions for the same field cases but for other specimens. This type of analysis can be performed using many different combinations, but a representative study will be discussed below.

5.4.2 Rate-Dependent Dielectric Hysteresis

The model discussed in Section 5.3.2 and the final governing equation given by (5.25) was used to infer model parameter distributions from the electric displacement-electric field data. Model calibration was done using subsets of the experimental data from the Sawyer-Tower circuit. In this case the calibration parameters are

$$\theta = [\kappa_r, \tau]. \tag{5.28}$$

Application of the MCMC algorithm was analogous to the membrane model with respect to calculating the sum-of-squares and weighting different data sets equally. Due to the observed change in permittivity seen in Figure 5.6(a), the analysis will also include a study of how transverse displacement affects the dielectric hysteresis model.

5.4.3 Case Studies

Following the discussion of the different parameter estimation approaches, five different Bayesian calibrations are considered. A discussion of the cases is provided below and a summary is provided in Table 5.2.

Table 5.1: Calibration cases using transverse load-displacement data.

Case Study	Calibration Parameters	Specimens	Percent Pre-Stretch	Applied Voltages (kV)
F1	G_c, G_e, λ_{max}	[1,2,3,4]	300	0
F2	κ_r	[1,2,3,4]	300	1-6
F3(a)	κ_r	[1,2,3,4]	300	1
F3(b)	κ_r	[1,2,3,4]	300	2
F3(c)	κ_r	[1,2,3,4]	300	3
F3(d)	κ_r	[1,2,3,4]	300	4
F3(e)	κ_r	[1,2,3,4]	300	5
F3(f)	κ_r	[1,2,3,4]	300	6

- **F1:** Calibrate non-affine hyperelastic parameters given by (5.26) using transverse load model. Use transverse load data from several specimens in which there is no applied voltage → no electrostriction.

- **F2:** Calibrate the relative permittivity given by (5.27) using transverse load model. Use transverse load data from several specimens in which there is a nonzero applifed voltage. Include data from multiple voltage levels in single calibration.

- **F3(a-f):** Repeat Case F2, but perform analysis on different voltage levels separately. This will show whether any data set may be biasing the fusion process in Case F2.

- **D1:** Calibrate the rate-dependent dielectric parameters from (5.28) the rate-dependent dielectric constitutive model. Use data from Sawyer-Tower experiment and include multiple amplitude voltage levels for a single specimen.

- **D2(a-c):** Repeat Case D1, but consider the effect of transverse displacement. Use individual data sets from the Sawyer-Tower experiment with a maximum amplitude voltage of 3 kV (for 300% pre-stretch, this implies maximum field values of 27 MV/m). Data sets only differ by the amount of transverse displacement.

Unless otherwise listed, units for the non-affine moduli from (5.9) are given in kilopascals (kPa), the dielectric time constant given in (5.25) is in seconds (s), and all other model parameters are unitless.

Table 5.2: Calibration cases using data from Sawyer-Tower experiment.

Case Study	Calibration Parameters	Specimens	Percent Pre-Stretch	Applied Voltages (kV)	Transverse Displacement (mm)
D1	κ_r, τ_D	[1]	300	2-5	0
D2(a)	κ_r, τ_D	[10]	300	3	0
D2(b)	κ_r, τ_D	[10]	300	3	2
D2(c)	κ_r, τ_D	[10]	300	3	4
D2(d)	κ_r, τ_D	[10]	300	3	6

5.4.4 Case F1: Hyperelastic Parameter Estimation

Initial considerations of the model calibration include chain convergence and parameter correlation. In Figure 5.7, we observe the parameter sampling that results in the posteriors seen in Figure 5.8. Based on the relatively static mean value and consistent variance of each chain, it can be reasonably assumed that convergence of the posterior density has been reached. Based on the trend observed in the chain, fewer iterations could have been performed in constructing the marginal densities; however, 5×10^5 realizations were performed due to the low computational cost.

In Figure 5.8 we observe the marginal posterior densities associated with each non-affine parameter which provides insight into the uncertainty associated with each parameter. Lower uncertainty is observed for the crosslink modulus G_c and maximum stretch λ_{max} in comparison to the entanglement modulus. This highlights improved constitutive relations may be needed to more accurately predict entanglement effects on macroscopic hyperelasticity. Note that the numerical method used to build the distribution plots allows the possible values of G_e to go into the negative regime, which is not possible given the model constraints. Analysis of the parameter chain shows only sampling of positive values for the plateau modulus, so the discrepancy seen in the center plot in Figure 5.8 is caused by the numerical approach used in building the densities.

An additional item to consider for the non-affine parameters is whether any relationship can be distinguished between the hyperelastic parameters. The relationships between each parameter are observed in Figure 5.9 where the parameters have been plotted against one

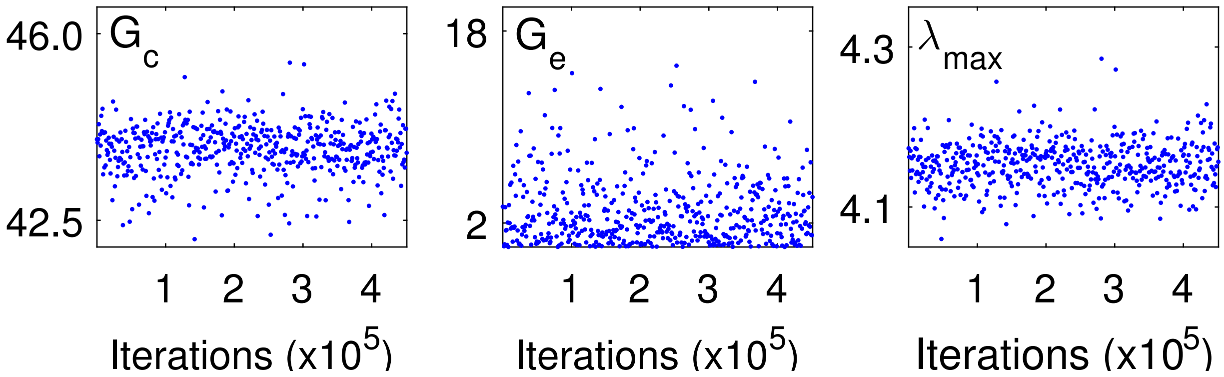

Figure 5.7: Parameter chain obtained with 5×10^5 realizations of the non-affine hyperelastic model to demonstrate convergence.

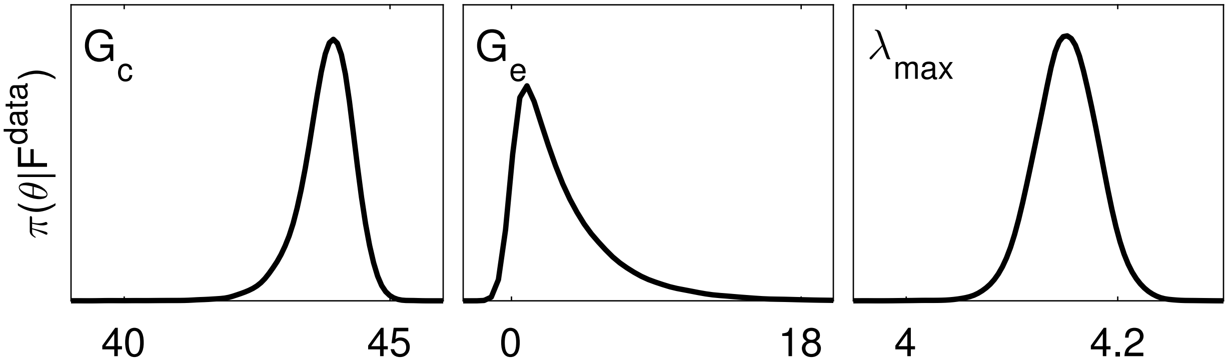

Figure 5.8: Marginal posterior parameter densities for non-affine hyperelastic model at $E_i = 0kV$. Note the units for G_c and G_e are in kPa, and λ_{max} is unitless.

another. These plots serve to quantify the parameter correlation. If two parameters appear to form a straight line when plotted against each other, this would imply a nearly-single value linear correlation. Such relationships indicate a lack of identifiability because a single value for one can be used to define the other. It is also possible to have nearly-single, nonlinear correlations. As seen in Figure 5.9, there is no clear relationship between any of the hyperelastic parameters.

It is also of interest to compare non-affine hyperelastic parameters calibrated for transverse membrane loading to uni-axial stress-stretch calibration [50, 55]. In Chapter 3, the non-affine hyperelastic parameters for uni-axial loading have been found to be on the same

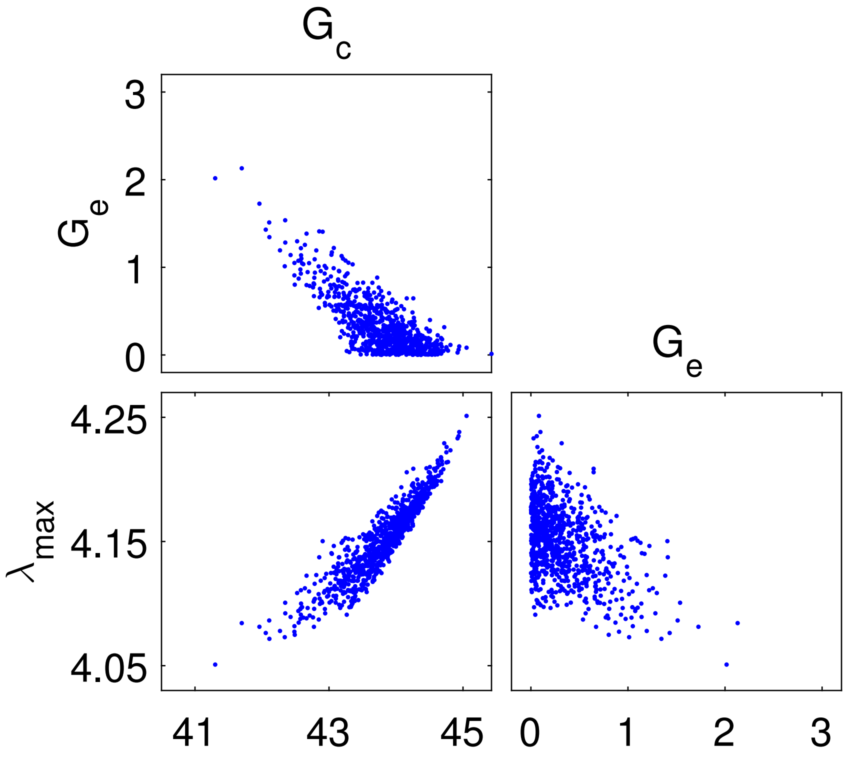

Figure 5.9: Joint sample points of parameter chains.

order of magnitude as those found in this study; however, there are notable differences. The results from previous uni-axial analysis and the current study are summarized in Table 5.3. A comparison of the posterior densities (see Figure 3.4 in Chapter 3) highlights that even the shape of the distributions is altered.

Whereas a direct comparison of these two sets of experiments is challenging, in light of the addition of viscoelastic modeling for the uni-axial study, a few key relations are useful. The nominal crosslink modulus has increased by a factor of 7.4 between the transverse membrane and uni-axial loading cases, while the plateau modulus has decreased by a factor of 2.5. As the elastomer is deformed during transverse membrane loading, the effects of entanglement may be significantly reduced since all deformation occurs from a pre-stretched state unlike in prior uni-axial measurements. However, as polymers are aligned in different directions, it could also potentially increase the number of intersections between polymer chains, thereby increasing the effective modulus associated with crosslink behavior. Additionally, prior uni-

Table 5.3: Comparison of mean non-affine hyperelastic parameters from uni-axial model calibration [50] and current transverse membrane loading conditions. The units for G_c and G_e are in kPa, and λ_{max} is unitless.

θ	Uni-Axial	Transverse
G_c	5.52	40.6
G_e	4.64	1.83
λ_{max}	4.99	4.20

axial model calibration was conducted by identifying viscoelastic properties. Since transverse load data was only taken over one stretch rate, rate effects were ignored. Since modeling was performed and compared to the loading portion of the transverse load/unload cycle, the additional effect of viscoelasticity may bias the parameter estimation.

Further complicating the uncertainty is the non-constant rate of deformation in the radial direction during transverse mechanical loading. Based on the geometry shown in Figure 5.2(b), and the assumption of homogeneous deformation along the membrane radius, we find the radial velocity to be

$$\frac{dl}{dt} = \frac{\delta^2}{(l_0^2 + \delta^2)} \frac{d\delta}{dt} \tag{5.29}$$

where the transverse displacement speed, $d\delta/dt$, is a constant, 1.41 mm/s. As this is a function of the transverse displacement, we consider the max and mean radial velocity and normalize it by the initial radial length, l_0, to give us a stretch rate to compare with the uni-axial load cases.

$$\frac{d\lambda_l}{dt} = \frac{dl}{dt} \frac{1}{l_0}. \tag{5.30}$$

From (5.30) we found the max and mean stretch rate to be 13.2×10^{-3} Hz and 4.73×10^{-3} Hz, respectively. The data from the uni-axial load case was collected at a stretch rate on the order of 6.5×10^{-5} Hz. The higher, non-homogeneous stretch rate may have an effect on the calibrated parameters. The goal of the present work is to characterize the hyperelastic, electrostrictive, and dielectric response of the material. Quantifying the rate-dependent behavior is left for future work.

5.4.5 Cases F2: Electrostrictive Parameter Estimation

The relative permittivity is first identified using the transverse load model based upon electrostrictive coupling. The model was calibrated using experimental data sets for specimens 1-4 in which there was an applied field. We must define nominal values for the hyperelastic parameters, and in this instance it is reasonable to take the mean values from Case F1. A plot of the marginal posterior of κ_r is shown in Figure 5.10. Several results are shown in Figure 5.11 that indicate reasonable model agreement across all test cases. In these plots we have developed credible and prediction intervals to quantify the model uncertainty.

Credible intervals are found by propagating a statistically significant number of parameter values from the posterior densities through the model to provide predictive response distributions. Furthermore, by also propagating observation errors $\varepsilon_i \sim N(0, \sigma^2)$ through the model, one can construct prediction intervals. The variance is inferred through the Bayesian model calibration techniques. Because the prediction intervals include uncertainty from both the parameters and observations, they quantify the probability of observing future numerical predictions or experimental observations, i.e., they quantify the model's predictive capability. For a more detailed discussion on the construction and interpretation of Bayesian intervals see Section 9.4 of [75].

While these results give the impression of being very well defined, it is important to remember that additional parameters in the model also are uncertain and have underlying distributions of their own. So, it is best to interpret these results in light of the limiting case of having taken a nominal value for the hyperelastic non-affine parameters.

5.4.6 Case F3(a-f): Electrostrictive Parameter Estimation - Field Analysis

As described in Case F2, the mean value of the relative permittivity was found to be $\kappa_r = 7.65$, which produced agreeable results with all data sets. However, when performing model calibration it is important to test the model with non-trained boundary conditions. To do this, we consider estimating the relative permittivity again, except based on a single applied voltage level. This results in different values of the permittivity for each field as given

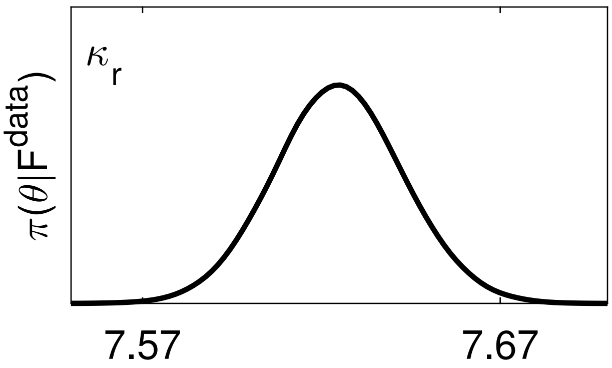

Figure 5.10: Marginal posterior parameter density for the relative permittivity. Calibration performed using transverse load model and data for all voltages applied to membrane.

in Table 5.4. Using this approach, the mean permittivity and its standard deviation inferred from the Bayesian calibration both decrease as the field increases. While the reduction in standard deviation at higher voltage suggests more certainty in its parameter value, it is also shown that calibration at higher fields produces better predictions on uncalibrated data sets. This is found by taking the resulting value of κ_r and applying it to the other voltage cases to observe how well it predicts behavior for cases not trained by the data.

The predictive attributes of the model are shown in Table 5.4. The first and second columns indicates the calibration case study with corresponding applied voltage, respectively. The third and fourth columns reflect the statistics found for κ_r based on the calibration. The remaining columns illustrate the model prediction error for a set of test cases. The last column highlights the total error over all the data tested. The total error is less when κ_r is estimated at higher voltage amplitudes. This is expected since the sensitivity of electrostriction increases with the mean field magnitude.

Given these results, Case F3 is re-assessed with respect to model prediction. In Case F3 all data sets were weighted equally; however, the sensitivity at higher fields due to electrostriction provided better training data to estimate κ_r. As seen in Table 5.4, the relative permittivity at higher fields is very similar to the value reported in Case F2. Furthermore,

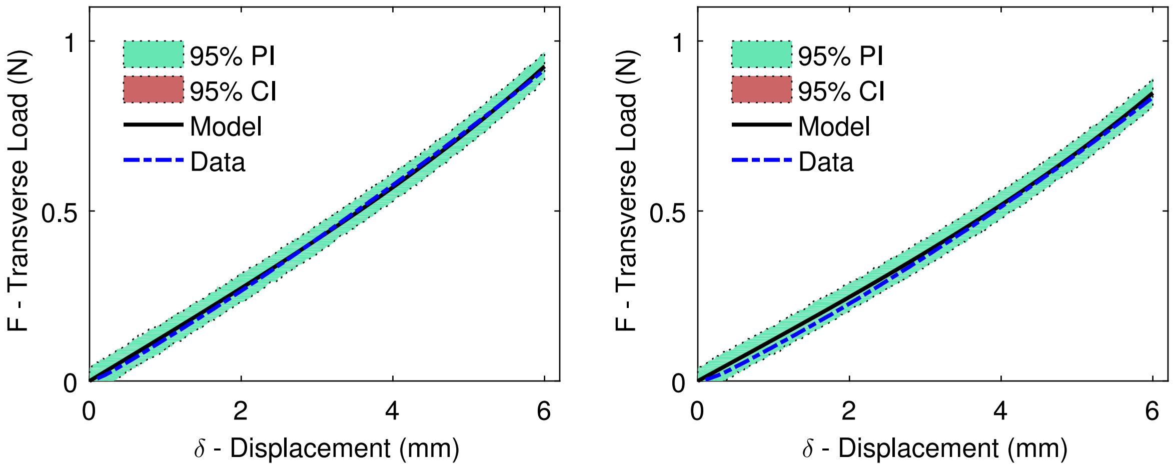

a) Applied Voltage: 0 kV　b) Applied Voltage: 3 kV

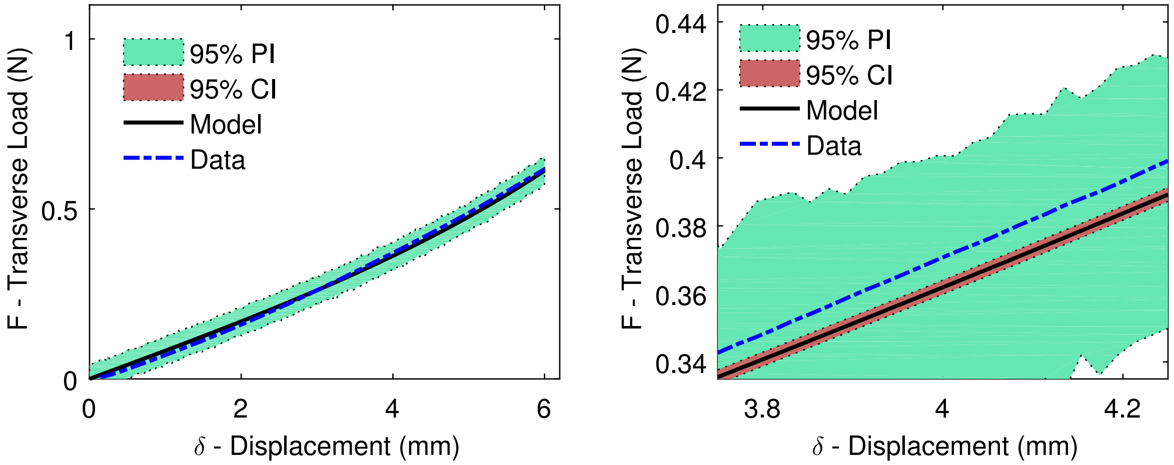

c) Applied Voltage: 6 kV　d) Applied Voltage: 6 kV, Zoomed-In

Figure 5.11: 95% prediction (PI) and credible (CI) intervals for the transverse load data along with median model estimates. Data sets found in Figure 5.3 are included for comparison. (d) Highlights scale of prediction and credible intervals. Results not shown for applied voltages at 2 kV, 4 kV, and 5 kV.

Table 5.4 gives an asymptotic reduction in error as it approaches the largest voltages tested (5-6 kV).

5.4.7 Case D1: Rate-Dependent Dielectric Model

We now consider parameter analysis using the rate-dependent dielectric model given by (5.25) in order to identify the relative permittivity which is common to both models and

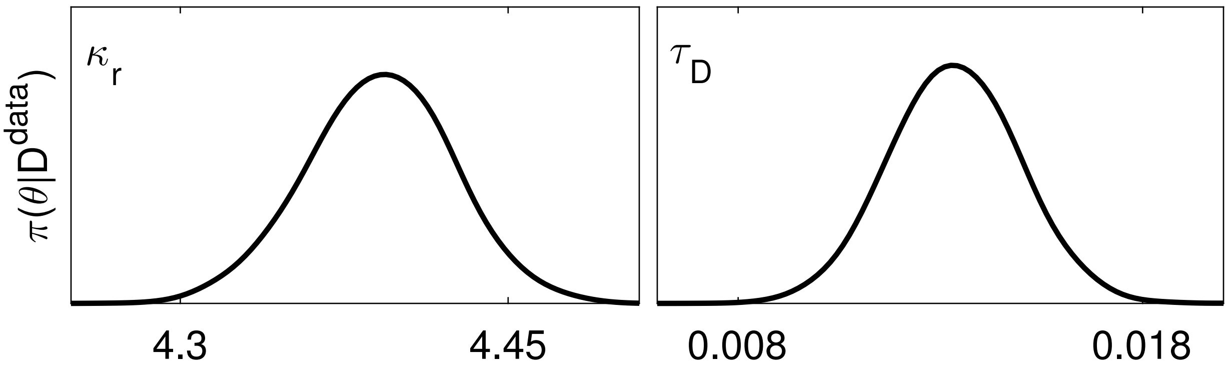

Figure 5.12: Marginal posterior parameter densities for dielectric model. The densities are created using data from the D-E loops for case study D1.

the dielectric time constant. The posterior densities (Figure 5.12) and chains are assessed to gauge parameter convergence. Using 5×10^5 samples of the model, we found the chains to be burned-in resulting in converged posterior densities presented in Figure 5.12. By sampling out of the posteriors from Figure 5.12 we plot the 95% credible and prediction intervals associated with the model and how it compares to data in Figure 5.13. Given the calibrated distribution for the relative permittivity, it is also of interest to propagate this parameter through the transverse load model to see how it compares with data. As seen in Figure 5.14, when using the posterior density calibrated in Case D2, the transverse load model significantly underpredicts the effects of electrostriction. Importantly, the re-

Table 5.4: Parameter statistics are provided in columns 3 (mean - $\bar{\kappa}_r$) and 4 (standard deviation - σ_{κ_r}). Columns 5-10 reflect the model error ($L_2 - norm$) in units of N^2. Error calculated based on model prediction for each voltage level.

Case Study	Calibrated Volt. (kV)	κ_r - Statistics $\bar{\kappa}_r$	σ_{κ_r}	Predicted Voltages (kV) 1	2	3	4	5	6	Total Error
F3(a)	1	11.12	0.82	0.12	0.15	0.30	0.55	0.87	1.28	3.27
F3(b)	2	8.76	0.21	0.12	0.12	0.14	0.20	0.31	0.44	1.33
F3(c)	3	8.13	0.10	0.12	0.12	0.12	0.14	0.18	0.23	0.91
F3(d)	4	7.77	0.05	0.12	0.13	0.13	0.12	0.13	0.13	0.76
F3(e)	5	7.57	0.03	0.12	0.13	0.13	0.13	0.12	0.11	0.75
F3(f)	6	7.57	0.02	0.12	0.13	0.13	0.13	0.12	0.11	0.75

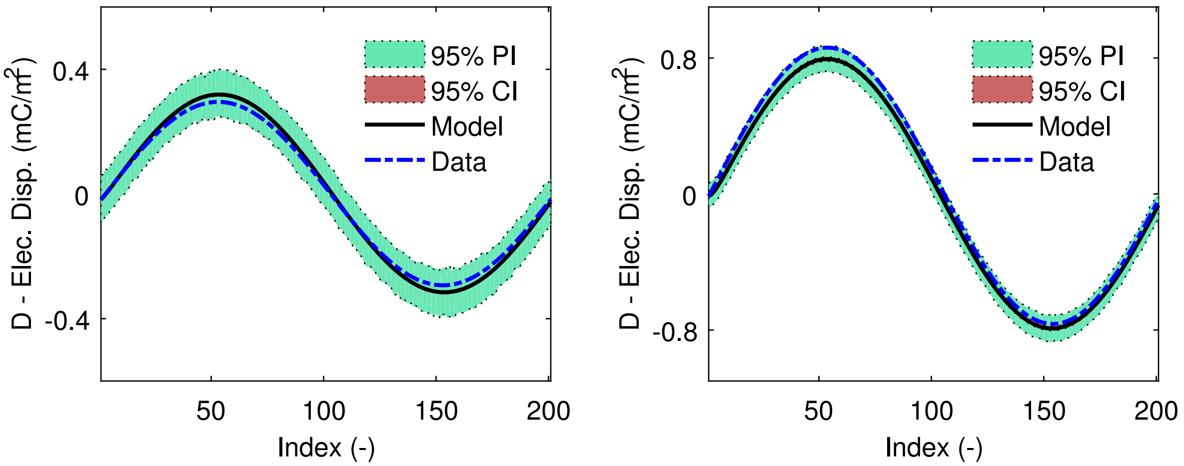

a) Field: 2 kV b) Field: 5 kV

Figure 5.13: 95% credible and prediction intervals for the $D-E$ loops along with median model estimates. Data sets found in Figure 5.5 are included for comparison. Note the data has been plotted with respect to index to more clearly represent the 95% prediction (PI) and credible (CI) intervals.

sults show a significant discrepancy between the dielectric constant measured from electric displacement-electric field (D-E) loops versus inferring the dielectric constant based on an electrostrictive constitutive relation from the energy function given by (5.7). Since the D-E loop data was conducted at fixed strain conditions, it suggests that electrostriction may be described by a deformation dependent permittivity such that the force-displacement data may also be consistent with the model. To assess this hypothesis, we must consider inhomogeneous deformation along the radius of the membrane to more accurately accommodate the underlying electromechanical coupling. This is left as future work.

5.4.8 Case D2(a-c): Rate-Dependent Dielectric Model - Effect of Transverse Displacement

The motivation for considering Case D2 stems from the experimental observation that the slope of the dielectric hysteresis changed with the addition of transverse displacement as shown in Figure 5.6(a). The membrane was deformed to a fixed amount of transverse displacement, and then the Sawyer-Tower experiment was repeated at that position. So, the transverse displacement resulted in a decrease in thickness which affects the applied field.

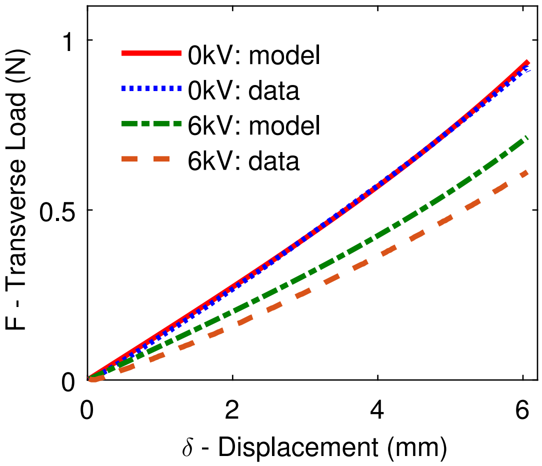

Figure 5.14: Model underpredicts effects of electrostriction at higher fields when using parameters calibrated from electric displacement-electric field (DE) hysteresis cycles (Case D1).

We perform calibration for data sets collected using specimen 10 in which the experiment was varied by being performed at $\delta = 0, 2,$ and 4 mm of transverse displacement.

There are many variations of numerical experiments we can perform by analyzing different data sets. The goal of this case study is to note how transverse displacement introduces uncertainty into the parameters of the dielectric hysteresis model. To demonstrate this uncertainty we will show the resulting posterior densities from a representative set of calibration studies. As seen in Figure 5.15, the relative permittivity found for each subset of data is quite distinct. This result agrees with the observation made of the data in Figure 5.6(a), that the slope of the dielectric hysteresis curve changes with the addition of transverse displacement. The mechanism which causes this change is yet to be determined.

5.5 Concluding Remarks

The stresses within the membrane are caused by three distinct aspects of the design: 1) bi-axial pre-stretching, 2) transverse mechanical loading, and 3) application of electrostatic fields. Loading of this nature has been considered previously but in a spring loaded configuration [69], which has been used in a family of commercial devices known as universal

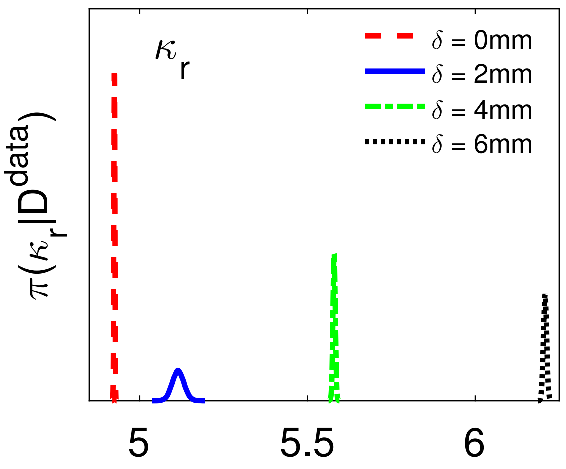

Figure 5.15: Comparison of marginal posterior densities for the relative permittivity in the dielectric hysteresis model. These densities represent the distributions identified for case studies D2(a-c). It is clearly seen that the addition of transverse displacement significantly affects the calibrated density of κ_r.

muscle actuators UMA's, marketed by Artifical Muscle, Inc. In this model, the applied forces must be balanced with the nonlinear geometric effects of finite deformation, nonlinear constitutive relations. Previous modeling has been done implementing an Ogden hyperelastic constitutive relation along with linear viscoelasticity [32].

In the current study, we proposed the use of a nonaffine hyperelastic constitutive model [15]. This was combined with an appropriate model to capture the electrostrictive behavior of the material. A nonaffine hyperelastic model has yielded comparable results to a higher order Ogden constitutive relation in previous work [50]. The nonaffine model is advantageous because it reduces the number of model parameters and is less phenomenological. The hyperelastic model was embedded within the overall structural model. While it is known that the true deformation profile is inhomogeneous, it is important to determine whether a simpler homogeneous model can still yield sufficiently accurate results for certain adaptive structure applications. In light of the desired implementation on a robotic platform, a numerically efficient algorithm is desired for model-based feedback control, thus making the homogeneous model relevant.

Uncertainty analysis has been used in assessing the homogeneous deformation model, revealing the potential existence of deformation dependent permittivity within the material [49]. Bayesian methods worked well for identifying the unknown model parameters, but this study reveals the importance of testing calibrated model parameters with non-trained data. The calibration was performed by using data from one experiment (electric displacement-electric field (D-E) hysteresis cycles). The calibrated parameters were then used to predict the behavior of a completely different experiment (transverse deformation with electrostatic field), yielding results that did not agree well with data (see Figure 5.14). This discrepancy indicates the potential dependence that permittivity has with respect to deformation.

In order to confirm these results, an assessment of an inhomogeneous deformation model [88] must be performed to determine if the simplifying assumptions within the homogeneous model created the appearance of deformation dependent permittivity. Analysis in light of uncertainty is non-trivial as the inhomogeneous model is not currently amenable to Bayesian methods. Simple optimization studies have revealed a similar dependence between the permittivity and transverse deformation, but further analysis is required to confirm this behavior. It may also prove necessary to consider the viscoelastic nature of the material in the context of determining the electrostrictive characteristics.

CHAPTER 6

FERROELECTRIC DOMAIN STRUCTURE EVOLUTION: THEORY

6.1 Introduction

Modeling domain structure evolution at the atomic and electronic scale remains a significant challenge in many active materials (e.g., ferroelectric, ferromagnetic, shape memory alloys). Density functional theory (DFT) provides an accurate means by which to quantify many structure-property relations in solids [23, 59], but it is not necessarily conducive to the large scale computations required to solve these problems [72]. Other methods provide the means to simulate the length scale gap between nano- to microscale domain structure evolution, typically by introducing a phase field polarization order parameter [10, 25, 47, 87]. These methods are computationally feasible by using coarser grids in regions of uniform polarization (i.e., domains). Such regions are separated by nanoscale twinned domain walls. These domain walls make continuum approximations of the electronic behavior non-trivial and introduce uncertainty. Polarization evolves along different thermodynamic paths due to applied electric fields as well as stress caused by local effects on domain walls [20, 34, 54, 75]. This results in parameter uncertainty when approximating the electronic behavior in uniform domain regions and across domain walls.

The phase field model includes various phenomenological parameters which require the computation of energy and stress over a range of polarization values in the three dimensional polarization space [78]. We determine the equilibrium atomic positions for different uniaxial and shear deformation states in order to predict the atomic displacements in ferroelectric unit cells. For certain atomic structures it is acceptable to assume that the atoms in the crystal structure linearly follow the overall motion of the solid. This assumption is known as the Cauchy-Born rule; however, the complexities of the current calculations preclude the use of the Cauchy-Born rule for accurate predictions. Atoms are incremented about a fixed strain state which yields a non-convex energy surface in polarization space. We use DFT to calculate the low energy atomic states based on these different fixed atomic positions, leading to our estimate of the non-convex free energy surface. The assumed zero strain state for estimating the Landau energy is based on a cubic state. The results from the phase field model and DFT calculations are useful in understanding each method's predictive capability as well as quantifying the uncertainty between the two methods.

The uncertainty analysis will focus on quantifying model parameter probabilities of the phase field model in light of the DFT calculations. Both monodomain and polydomain structures will be considered within the Bayesian uncertainty analysis of domain structure characteristics. Ongoing research in our group has questioned the self-consistency in identifying monodomain parameters including the effects of twinned domain structures.

The rest of the chapter is broken into the following sections. The DFT calculations and methodology behind them are discussed in Section 6.2. The theory associated with monodomains and twinned domain structures will be presented in Section 6.3. Finally, the uncertainty analysis is discussed in Section 7.1.

6.2 Density Functional Theory Calculations

The goal of performing the density functional theory (DFT) calculations is to quantify the continuum scale Landau energy and electrostrictive stresses associated with uniform polarization states. The DFT calculations were performed using ABINIT[1]. The simulations were performed on a $10 \times 10 \times 10$ k-point grid for a five atom lead titanate ($PbTiO_3$) unit cell with a cut-off energy of 60 Hz (1633 eV). All calculations make use of the local density approximation (LDA). We combine these energy calculations with prior one dimensional results on lead titanate [54] in order to estimate the stored energy for a broader range of polarization states. Previous development identified pseudopotentials which were used to approximate electron density.

---

[1] The DFT calculations for this project were performed by Justin Collins.

The first part of the DFT calculation was to identify equilibrium atomic positions in the fully relaxed equilibrium lattice configuration in the tetragonal state. The atoms were subsequently incremented in the cubic state with lattice dimensions $a \times a \times a = 57.4$ Å^3. Starting from the centrosymmmetric atomic configuration, the atoms were linearly incremented through the equilibrium tetragonal state, resulting in a double well potential energy function. In order to quantify the stored energy surface caused by polarizations not aligned with the spontaneous polarization direction, atomic displacements under internal atomic shearing are used to estimate the full three dimensional energy surface. Crystal symmetry in lead titanate requires incrementing the polarization by an angle ranging from 0° to 45° for different polarization magnitudes. The atoms will move during the polarization reorientation. The reorientation will start with full alignment in the x_3-direction, followed by 45° rotation towards the x_2-direction. The atomic motion is estimated by conducting a series of *ab initio* molecular dynamic simulations about several fixed unit cell shear deformation states and simultaneously determining the equilibrium atomic positions and electron density. Entropic effects are neglected by computing energy, stress and polarization in the limit of zero Kelvin.

The molecular dynamic simulations use the minimization method based on the Broyden-Fletcher-Goldfard-Shanno method contained within ABINIT 7.0.5 [23]. The deformation gradient component $F_{23} = \frac{\partial x_2}{\partial X_3}$, based on conventional deformation notation [45], is incremented from zero up to 0.17 while holding all other deformation gradient components fixed. The Berry phase approach [68] is used to find the polarization once the equilibrium configurations are known. The atomic and electronic structures differ from the undeformed reference state and the shear deformed state as shown in Figure 6.4.

At each increment of the deformation gradient, the atomic displacements are determined. We have implemented a linear fit for the titanium atom positions in the $x_2 - x_3$ plane with respect to the different F_{23} values as shown in Figure 6.1(a). In Figure 6.1(b) it is observed that the polarization changes as the titanium atom displaces in shear. All the atoms in lead titanate have similar characteristics, which we approximate as linear with respect to polarization for estimating the atomic evolution during polarization rotation, $P_3 \rightarrow P_2$.

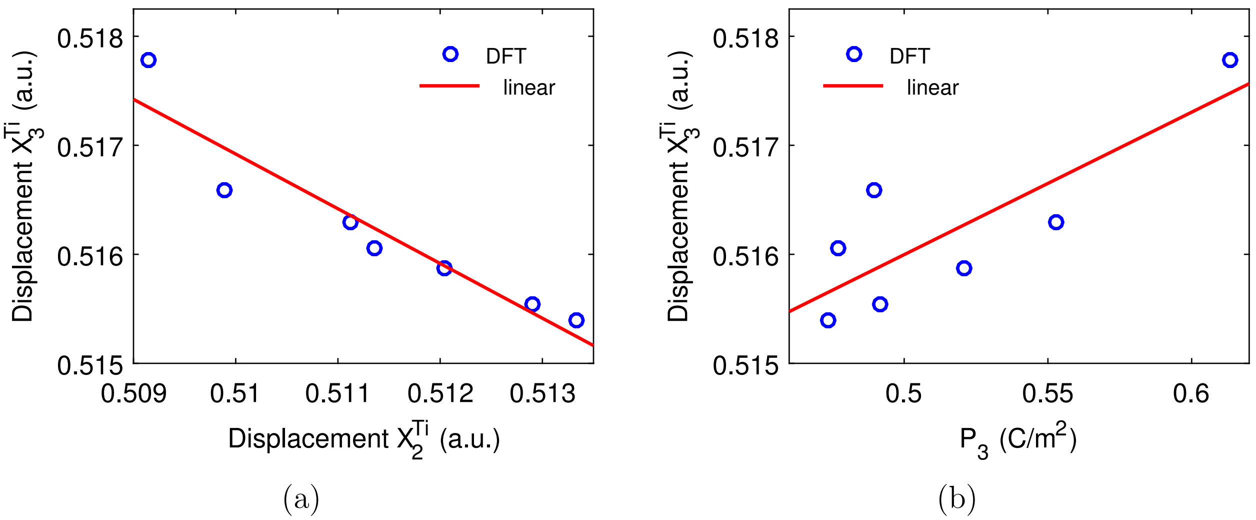

Figure 6.1: (a) Atomic displacement showing the relationship between the position of the titanium atom in the x_2 and x_3 directions as the deformation component F_{23} varies between 0 and 0.17. (b) Relationship between the atomic position (titanium atom) and polarization in the x_3 direction as the deformation gradient component F_{23} varies between 0 and 0.17.

The linear approximation is extremely important for the rest of our analysis. Approximate linear displacements of the atomic nuclei during shear deformation and polarization rotation serve as a guide in determining the energy surface as a function of polarization at zero strain. The changes in stored energy as a function of atomic displacements are computed using DFT calculations while holding the unit cell fixed at a reference cubic state using the same unit cell geometry as prior uniaxial results [54]. The process of combining these new calculations with previous research is simplified by the linear approximation; however, uncertainty is introduced between the atomic positions and resulting polarization when using the cubic state as the reference configuration. This is clearly seen in Figure 6.1(b), where the linear assumption only nominally agrees with the calculated displacement. Although the thermodynamic path during shear deformation is not necessarily unique, the calculated energy is unique for the particular unit cell shape and atomic positions used in our analysis.

As mentioned earlier, the atoms were linearly incremented from different atomic positions starting near the centrosymmetric state through the equilibrium tetragonal state. Five different starting P_3 values with $P_2 = 0$ were used for polarization rotation, $P_3 \rightarrow P_2$,

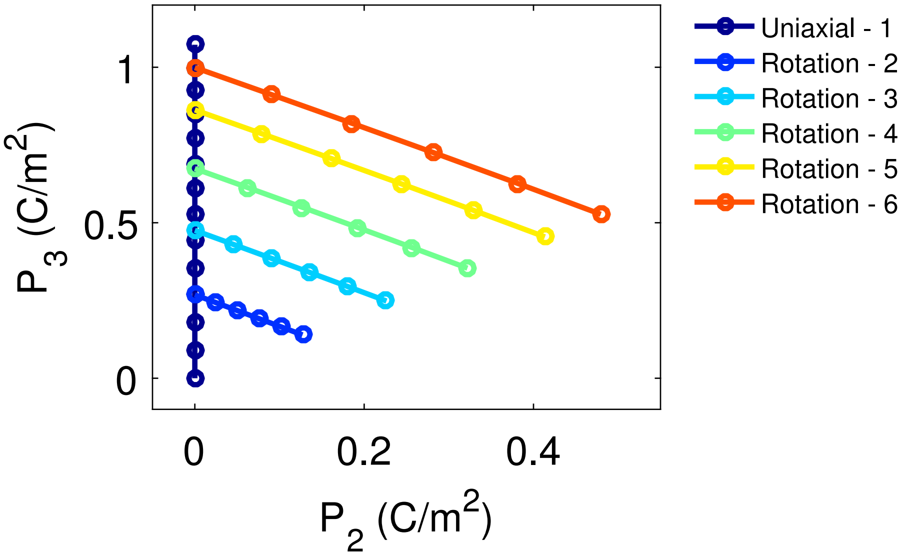

Figure 6.2: Polarization states at which energy and stress tensor were calculated. Six different polarization studies were performed.

as shown in Figure 6.2. The additional polarization points along the P_3-axis come from uniaxial analysis as discussed in [54]. For the five starting points, the atoms were moved along the directions estimated from the shear deformation (F_{23}) states to generate positive P_2 values while decreasing P_3. At each point shown in Figure 6.2 the energy and stresses are measured. The total energy can be seen in Figure 6.3(a), and the shear stress component of the stress tensor, σ_{23}, is shown as a function of polarization in Figure 6.3(b). The key results observed in these plots is that both the energy and stress change due to polarization rotation, which stems from the displacement of the atoms. In Section 7.1 we will demonstrate how uncertainty analysis can be used to estimate parameters associated with the phase field continuum model.

Up to this point all of our DFT calculations have focused on monodomain structures, i.e., structues with uniform polarization in the entire domain. We will also consider DFT domain wall calculations for an 180° polydomain structure in lead titanate. The domains within these structures are divided by a nanoscale wall which adds energy to the system. For 180° domain wall structures the reported energy is $E_{180^\circ} = 132$ mJ/m^2 and the domain wall width is on the order of the lattice constant, a [48]. Note, the domain wall size is most

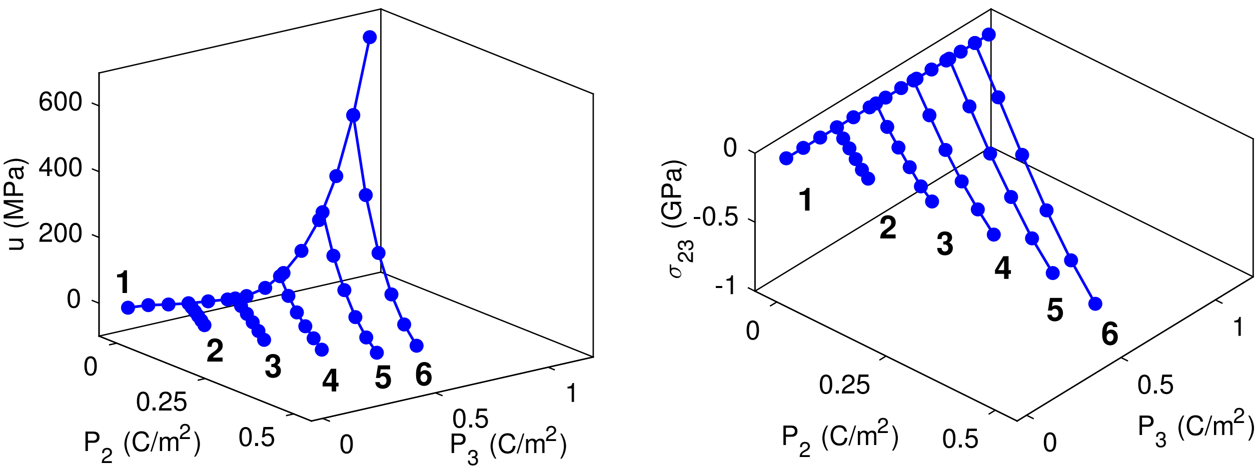

(a) DFT Energy Density (b) DFT Stress σ_{23}

Figure 6.3: Plots of (a) total energy and (b) shear stress (σ_{23}) as a function of P_2 and P_3. Lines are numbered for reference in later discussion.

likely underestimated as the DFT calculations were performed for the limiting case of zero Kelvin using a relatively small supercell. This has been pointed out through domain wall calculations of barium titanate [86]. Before we can analyze this polydomain structure we must first define our phase field continuum model and characterize it with respect to our monodomain DFT calculations.

6.3 Continuum Phase Field Model

The general form of the continuum phase field model is defined by the free energy density function

$$u(P_i, P_{i,j}, \Delta\varepsilon_{ij}) = u_M(\Delta\varepsilon_{ij}) + u_L(P_i) + u_C(P_i, \Delta\varepsilon_{ij}) + u_G(P_{i,j}), \tag{6.1}$$

where P_i is the polarization in the i^{th}-direction, $P_{i,j}$ is the polarization gradient, and $\Delta\varepsilon_{ij}$ is the strain. The energy densities include u_M as the elastic energy of the system, u_L as the Landau energy, u_C as the electrostrictive energy, and u_G as the polarization gradient energy. This analysis is non-trivial due to coupling between the Landau energy, electrostrictive energy, and energy associated with polarization gradients [8]. Note that in the case of a monodomain, the energy terms in (6.1) can be simplified. There are no polarization gradients in a monodomain structure, and the strain and polarization can be determined in closed-form from energy minimization.

The form of these energy functions in standard cartesian coordinates are as follows. The mechanical energy is defined as

$$\begin{aligned} u_M(\Delta\varepsilon_{kl}) = &\frac{c_{11}}{2}(\Delta\varepsilon_{11}^2 + \Delta\varepsilon_{22}^2 + \Delta\varepsilon_{33}^2) + c_{12}(\Delta\varepsilon_{11}\Delta\varepsilon_{22} + \Delta\varepsilon_{11}\Delta\varepsilon_{33} + \Delta\varepsilon_{22}\Delta\varepsilon_{33}) \\ &+ 2c_{44}(\Delta\varepsilon_{12}^2 + \Delta\varepsilon_{13}^2 + \Delta\varepsilon_{23}^2) \end{aligned} \tag{6.2}$$

where c_{11}, c_{12}, and c_{44} are elastic coefficients. The strain components are defined by $\Delta\varepsilon_{ij} = \varepsilon_{ij} - \varepsilon_{ij}^S$ where ε_{ij}^S is the spontaneous strain due to transition from the reference cubic state to the relaxed tetragonal state. In all numerical analysis, we restrict the spontaneous strain to be defined for a spontaneous polarization aligned in the x_3 direction. This results in non-zero $\varepsilon_{11}^S = \varepsilon_{22}^S$ and ε_{33}^S spontaneous strain components and all others zero. The Landau energy is given here by

$$\begin{aligned} u_L(P_i) = &\alpha_1(P_1^2 + P_2^2 + P_3^2) + \alpha_{11}(P_1^2 + P_2^2 + P_3^2)^2 \\ &+ \alpha_{12}(P_1^2P_2^2 + P_2^2P_3^2 + P_1^2P_3^2) + \alpha_{111}(P_1^6 + P_2^6 + P_3^6) \\ &+ \alpha_{112}[P_1^4(P_2^2 + P_3^2) + P_2^4(P_1^2 + P_3^2) + P_3^4(P_1^2 + P_2^2)] \\ &+ \alpha_{123}P_1^2P_2^2P_3^2 \end{aligned} \tag{6.3}$$

where the phenomenological constants are denoted by $\alpha_1, \alpha_{11}, \alpha_{12}, \alpha_{111}, \alpha_{112}$, and α_{123}. Coupling between the strain and polarization occurs in the electrostrictive energy function, which is

$$\begin{aligned} u_C(P_i, \Delta\varepsilon_{kl}) = &- q_{11}(\Delta\varepsilon_{11}P_1^2 + \Delta\varepsilon_{22}P_2^2 + \Delta\varepsilon_{33}P_3^2) \\ &- q_{12}[\Delta\varepsilon_{11}(P_2^2 + P_3^2) + \Delta\varepsilon_{22}(P_1^2 + P_3^2) + \Delta\varepsilon_{33}(P_1^2 + P_2^2)] \\ &- 2q_{44}(\Delta\varepsilon_{12}P_1P_2 + \Delta\varepsilon_{13}P_1P_3 + \Delta\varepsilon_{23}P_2P_3) \end{aligned} \tag{6.4}$$

where q_{11}, q_{12}, and q_{44} are the electrostrictive parameters. Finally, the gradient energy function is

$$\begin{aligned} u_G(P_{i,j}) = &\frac{g_{11}}{2}(P_{1,1}^2 + P_{2,2}^2 + P_{3,3}^2) \\ &+ g_{12}(P_{1,1}P_{2,2} + P_{1,1}P_{3,3} + P_{2,2}P_{3,3}) \\ &+ \frac{g_{44}}{2}[(P_{1,2} + P_{2,1})^2 + (P_{1,3} + P_{3,1})^2 + (P_{2,3} + P_{3,2})^2] \end{aligned} \tag{6.5}$$

where the exchange parameters are denoted as g_{11}, g_{12}, and g_{44}.

Bayesian statistical methods are ideal for this type of analysis where unknown phenomenological parameters are assumed to be random variables with underlying uncertainty. Our analysis then becomes a study of determining these parameter distributions rather than optimization of a fixed set of parameter values. For the cases we wish to investigate, the uncertainty is associated with the homogenization of DFT energy and stress calculations necessary to develop the three dimensional energy landscape and electrostrictive stress tensor.

Approximation via the continuum model yields a reduction of the internal degrees of freedom for the atomic position as well as changes in the surrounding electron density in a unit cell (see Figure 6.4). The position for each atomic nuclei in a unit cell has three degrees of freedom. For lead titanate ($PbTiO_3$), which contains five atoms per unit cell, this results in $5 \times 3 = 15$ total degrees of freedom. As a result of the atomic motion, the electron density changes. Due to the positive charge associated with the atomic nuclei and the distribution of electron density, this allows for measurement of polarization, which can be directly determined via DFT calculations using the Berry phase approach [68]. Polarization serves as the order parameter in determining changes in stress and energy as a result of changes in the atomic configurations. The 15 degrees of freedom for lead titanate has been approximated with a single polarization vector parameter. Research has been done with regard to the monodomain atomic structure of lead titantate ($PbTiO_3$). The Landau $(\alpha_1, ..., \alpha_{123})$ and electrostrictive (q_{ij}) parameters were calibrated with regard to DFT energy, stress, and polarization calculations. The uncertainty with these parameters was quantified using Bayesian statistical analysis as discussed in Chapter 2. A discussion of the results for the monodomain analysis is given in Sections 7.2.1 and 7.2.2. Examples of model predictions with respect to DFT calculations for energy along with parameter statistics will be presented in Section 7.1. Consideration of these parameters is not as easily obtained with regard to polydomain analysis.

The free energy described by (6.1) is then used to derive the Euler equations for the primary and secondary order parameters. Expansion of the free energy via variational methods

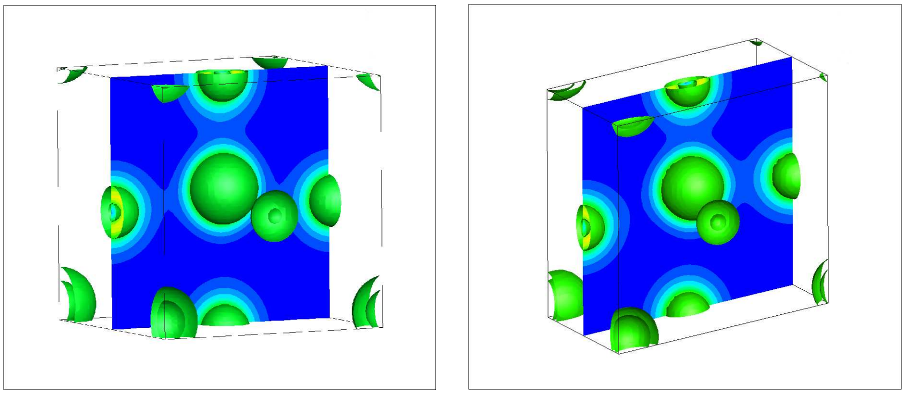
(a) (b)

Figure 6.4: Example of the electron density solutions for (a) the reference undeformed cubic structure and (b) shear deformed state where the unit cell has been sheared such that the deformation gradient component F_{23} is non-zero.

gives rise to the static equilibrium conditions with respect to polarization and strain. The condition for static equilibrium with regard to polarization is

$$\frac{\partial}{\partial x_j}\left(\frac{\partial u}{\partial P_{i,j}}\right) - \frac{\partial u}{\partial P_i} = 0 \quad (i, j = 1, 2, 3). \tag{6.6}$$

The stress in the material is found by taking the derivative of the energy function with respect to strain, and so the equilibrium constraint is

$$\sigma^{tot}_{ij,j} = \frac{\partial}{\partial x_j}\left(\frac{\partial u}{\partial \Delta\varepsilon_{ij}}\right) = 0 \quad (i, j = 1, 2, 3). \tag{6.7}$$

The divergence of stress should be zero for systems at static equilibrium. These definitions are important for understanding the application to both monodomain and polydomain ferroelectric structions. First, let us describe how these equations are evaluated for monodomain structures.

6.4 Monodomain Structures

The Euler equations given in (6.6) and (6.7) can be simplified when considering monodomain structures. Firstly, there are no polarization gradients as by definition the polarization is homogeneous in the entire domain, yielding the reduced form

$$\frac{\partial u}{\partial P_i} = 0 \quad (i, j = 1, 2, 3). \tag{6.8}$$

Also, we would expect no spatial variation in the stress, so the divergence of stress is zero. This leaves us with the continuum stress

$$\sigma_{ij}^{tot} = \frac{\partial u}{\partial \Delta\varepsilon_{ij}} = c_{ijkl}\Delta\varepsilon_{kl} - q_{ijkl}P_k P_l, \tag{6.9}$$

where c_{ijkl} are the elastic coefficients and q_{ijkl} are the electrostrictive coefficients. Recall that $\Delta\varepsilon_{ij} = \varepsilon_{ij} - \varepsilon_{ij}^S$. There is a residual stress associated with the spontaneous strain, ε_{ij}^S, which we define to be $\sigma_{ij}^R = -c_{ijkl}\varepsilon_{kl}^S$. As the polarization is constrained to move from P_3 to P_2, we expect $\sigma_{11}^R = \sigma_{22}^R$ and $\sigma_{12}^R = \sigma_{13}^R = 0$. Evaluating (6.9) yields the following stress components

$$\begin{aligned}
\sigma_{11} &= c_{11}\varepsilon_{11} + c_{12}(\varepsilon_{22} + \varepsilon_{33}) - q_{11}P_1^2 - q_{12}(P_2^2 + P_3^2) + \sigma_{11}^R, \\
\sigma_{22} &= c_{11}\varepsilon_{22} + c_{12}(\varepsilon_{11} + \varepsilon_{33}) - q_{11}P_2^2 - q_{12}(P_1^2 + P_3^2) + \sigma_{22}^R, \\
\sigma_{33} &= c_{11}\varepsilon_{11} + c_{12}(\varepsilon_{11} + \varepsilon_{22}) - q_{11}P_3^2 - q_{12}(P_1^2 + P_2^2) + \sigma_{33}^R, \\
\sigma_{23} &= 4c_{44}\varepsilon_{23} - 2q_{44}P_2P_3 + \sigma_{23}^R.
\end{aligned} \tag{6.10}$$

These theoretical models can be directly compared with the DFT calculations described in Section 6.2. Next, we will discuss the continuum approximation for monodomains within polydomain structures.

6.5 Polydomain Structures

6.5.1 Uniform Domain Regions

When considering polydomain crystal structures, we must first have an accurate model for the energy associated with the uniform domain regions. This will allow us to distinguish the energy related to domain walls from the energy of the entire structure. The monodomain (i.e., region of uniform polarization) energy is simply a function of temperature, and as such can be purely described by the phenomenological parameters in (6.2), (6.3), and (6.4). We implemented the same methodology described by Cao and Cross in [8]; however, several discrepancies were observed in their solution. Our corrected solution is presented below. All physical quantities are uniform in space, so the Euler equations, (6.6) and (6.7), reduce to

$$\begin{aligned}
\frac{\partial u}{\partial P_i} &= 0, \\
\sigma_{ij}^{tot} &= 0.
\end{aligned} \tag{6.11}$$

Note that the condition on stress assumes that no external stresses are being applied. Assuming all the polarization is oriented in the x_3-direction, then we are left with the following system of equations to solve,

$$\begin{cases} \frac{\partial u}{\partial P_3} = 2[\alpha_1 - q_{11}\Delta\varepsilon_{33} - q_{12}(\Delta\varepsilon_{11} + \Delta\varepsilon_{22})]P_3 + 4\alpha_{11}P_3^3 + 6\alpha_{111}P_3^5 = 0 \\ \frac{\partial u}{\partial \Delta\varepsilon_{11}} = c_{11}\Delta\varepsilon_{11} + c_{12}(\Delta\varepsilon_{22} + \Delta\varepsilon_{33}) - q_{12}P_3^2 = 0 \\ \frac{\partial u}{\partial \Delta\varepsilon_{22}} = c_{11}\Delta\varepsilon_{22} + c_{12}(\Delta\varepsilon_{11} + \Delta\varepsilon_{33}) - q_{12}P_3^2 = 0 \\ \frac{\partial u}{\partial \Delta\varepsilon_{33}} = c_{11}\Delta\varepsilon_{33} + c_{12}(\Delta\varepsilon_{11} + \Delta\varepsilon_{22}) - q_{11}P_3^2 = 0. \end{cases} \tag{6.12}$$

For temperatures well below the Curie temperature, the solution for polarization and strain in monodomains are found to be

$$P_3 = P_0 = \Big(\frac{-\alpha_{11}^{'} + (\alpha_{11}^{'2} - 3\alpha_1\alpha_{111})^{1/2}}{3\alpha_{111}}\Big)^{1/2} \tag{6.13}$$

$$\begin{aligned} \Delta\varepsilon_{11} = \Delta\varepsilon_{22} = \Delta\varepsilon_{\perp} &= \frac{P_0^2}{3}\Big[\frac{\hat{q}_{11}}{\hat{c}_{11}} - \frac{\hat{q}_{22}}{\hat{c}_{22}}\Big] \\ \Delta\varepsilon_{33} = \Delta\varepsilon_{\parallel} &= \frac{P_0^2}{3}\Big[\frac{\hat{q}_{11}}{\hat{c}_{11}} + \frac{2\hat{q}_{22}}{\hat{c}_{22}}\Big] \end{aligned} \tag{6.14}$$

where $\Delta\varepsilon_{ij} = 0$ for $i \neq j$, and $\alpha_{11}^{'}$ is

$$\alpha_{11}^{'} = \alpha_{11} + \frac{4c_{12}q_{11}q_{12} - q_{11}^2(c_{11} + c_{12}) - 2c_{11}q_{12}^2}{2\hat{c}_{11}\hat{c}_{22}} \tag{6.15}$$

The following set of parameters were used for convenience in the definitions given in (6.13), (6.14) and (6.15).

$$\begin{aligned} \hat{c}_{11} &= c_{11} + 2c_{12}, \quad \hat{c}_{22} = c_{11} - c_{12}, \\ \hat{q}_{11} &= q_{11} + 2q_{12}, \quad \hat{q}_{22} = q_{11} - q_{12}. \end{aligned} \tag{6.16}$$

The monodomain energy density, u_0, is found by substituting $\mathbf{P} = (0, 0, \pm P_0)$ along with the solution for $\Delta\varepsilon_{ij}$ into (6.1). As the polarization and strain are only temperature dependent, the energy density is constant throughout the entire domain.

6.5.2 180° Domain Wall

The basic principle of a 180° domain wall structure is that two regions have the same magnitude polarization but in opposition directions, and the dividing section between the two regions is the domain wall. For the purpose of our discussion, we will define the problem with the following coordinate system. In the two uniform regions, far from the domain wall, all of the polarization will be oriented in the positive or negative x_3-direction. To support the theoretical model development, we also analyzed the problem using a fully coupled (mechanics, Gauss' law, Ginzburg-Landau eqs.) finite element analysis (FEA). The analysis is performed on a block whose center is located at $(0, 0, 0)$ with lengths L_1, L_2 and L_3 in the x_1-, x_2-, and x_3-directions, respectively. As shown in Figure 6.5, results from the FEA show the transition from negative to positive polarization in the x_3-direction occurs as one moves along the x_1-coordinate. There is no change in polarization as one moves in the x_2-direction. Therefore, the only gradient terms of interest will be the gradient with respect to the x_1-direction. A summary of the mechanical boundary conditions used as part of the FEA are given in Table 6.1.

Mathematically, we can describe the polarization as

$$\mathbf{P} = (0, 0, P_3(x_1)), \tag{6.17}$$

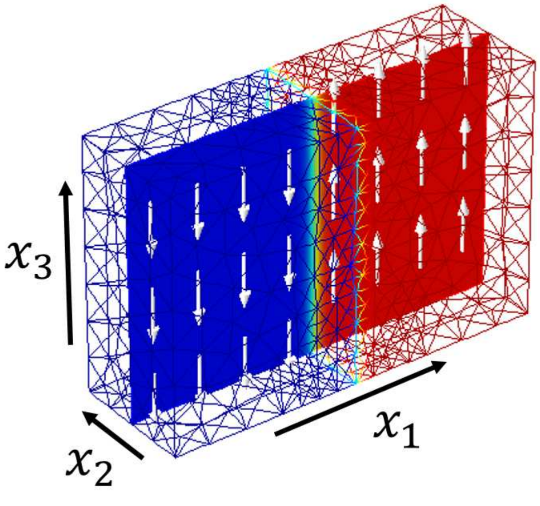

Figure 6.5: Polarization field in 180° domain wall structure.

Table 6.1: Displacement boundary conditions for finite element model of 180° domain wall structure.

Displacement Boundary Conditions	
$u_1(-L_1/2) = 0$	
$u_2(-L_2/2) = 0$	$u_2(L_2/2) = \eta_\perp L_2$
$u_3(-L_3/2) = 0$	$u_3(L_3/2) = \eta_\parallel L_3$

where all the polarization is in the x_3-direction. The boundary conditions for this problem are

$$\begin{aligned} &\lim_{x_1\to\pm\infty} \mathbf{P} = (0, 0, \pm P_0), \\ &\lim_{x_1\to\pm\infty} \sigma_{ij}^{tot}(x_1) = 0 \quad \text{for} \quad ij = 11, 22, 33, \\ &\sigma_{ij}^{tot}(x_1) = 0 \quad \text{for} \quad ij = 23, 13, 12, \end{aligned} \tag{6.18}$$

where P_0 is the magnitude of the polarization in the uniform domain regions, as discussed in Section 6.5.1.

Assuming $\mathbf{P} = (0, 0, \pm P_3(x_1))$, the static equilibrium conditions given in (6.6) and (6.7) reduce to the second-order nonlinear differential equation

$$\left(\frac{\partial u}{\partial P_{3,1}}\right)_1 - \frac{\partial u}{\partial P_3} = 0 \to 2\alpha_1^+ P_3 + 4\alpha_{11} P_3^3 + 6\alpha_{111} P_3^5 - g_{44} P_{3,11} = 0. \tag{6.19}$$

Here $\alpha_1^+ = \alpha_1 - q_{11}\Delta\varepsilon_{33} - q_{12}(\Delta\varepsilon_{11} + \Delta\varepsilon_{22})$, and the momentum constraint,

$$\sigma_{11,1} = 0 = c_{11}\Delta\varepsilon_{11,1} + c_{12}(\Delta\varepsilon_{22,1} + \Delta\varepsilon_{33,1}) - 2q_{12}P_3P_{3,1}. \tag{6.20}$$

From the boundary conditions in (6.18) one will find that all other strain components are zero. A numerical procedure is implemented to solve for $P_3(x_1)$ and $\Delta\varepsilon_{11}(x_1)$ simultaneously.

Numerical Solution: 180°. We numerically solve (6.19) and (6.20) using finite difference methods by introducing a time-dependent term with a damping parameter. The solution is iteratively updated until we reach a steady state solution. Once the system is at equilibrium, we are back to the original differential equations given by (6.19) and (6.20). When solving the second equation, it is beneficial to replace the strain component, $\Delta\varepsilon_{11}$, with the displacement gradient ($\Delta\varepsilon_{11} = u_{1,1}$). This ensures that compatibility constraints are automatically met, and makes comparison with FEA results simpler as the boundary conditions are in terms of displacement for both methods. Furthermore, by considering the solution along the x_1-axis, we can assume that the displacements in the x_2- and x_3-directions are zero. This leaves us with the time-dependent equations

$$\begin{aligned}\omega\frac{\partial P_3}{\partial t} &= g_{44}P_{3,11} - \Big[2\Big(\alpha_1 - q_{11}\Delta\varepsilon_{33} - q_{12}(u_{1,1} + \Delta\varepsilon_{22})\Big)P_3 + 4\alpha_{11}P_3^3 + 6\alpha_{111}P_3^5\Big],\\ \omega\frac{\partial u_1}{\partial t} &= c_{11}u_{1,11} - 2q_{12}P_3P_{3,1} = 0,\end{aligned} \tag{6.21}$$

where ω is a damping parameter. We use an implicit time integrator as part of the iterative procedure. A central-difference method is used to approximate the first and second order spatial derivatives. The boundaries are approximated using forward- and backward-Euler differencing schemes. The subscript, i, refers to the spatial point and the superscript, n, refers to the temporal step. To simplify the representation the following operators has been defined to represent the central difference approximation

$$\begin{aligned}\frac{\partial w}{\partial x} &\approx \delta_0 w_i = \frac{w_{i+1} - w_{i-1}}{2\Delta x},\\ \frac{\partial^2 w}{\partial x^2} &\approx \delta^2 w_i = \frac{w_{i+1} - 2w_i + w_{i-1}}{\Delta x^2}.\end{aligned} \tag{6.22}$$

for first and second order derivatives.

We will use the variable u_i to represent $P_3(x)$ and v to represent $u_1(x)$, which yields the discretized form

$$\begin{aligned}\omega\frac{u_i^n - u_i^{n-1}}{\Delta t} \approx\; & g_{44}\delta^2 u_i^n - 2(\alpha_1 - q_{11}\Delta\varepsilon_{33} - q_{12}\Delta\varepsilon_{22})u_i^n\\ & - 4\alpha_{11}(u_i^{n-1})^3 - 6\alpha_{111}(u_i^{n-1})^5\\ & + 2q_{12}u_i^{n-1}\delta_0 v_i^{n-1}\end{aligned} \tag{6.23}$$

and

$$\omega\frac{v_i^n - v_i^{n-1}}{\Delta t} \approx c_{11}\delta^2 v_i - 2q_{12}u_i^n\delta_0 u_i^n. \tag{6.24}$$

of (6.21). After rearranging (6.23) and (6.24), one finds that the numerical procedure results in a matrix problem, $Kw^n = d$, with the form

$$\begin{bmatrix} b_1 & c_1 & 0 & \dots & \dots & 0 \\ a_2 & b_2 & c_2 & \ddots & \ddots & \vdots \\ 0 & a_3 & b_3 & c_3 & \ddots & \vdots \\ \vdots & \ddots & \ddots & \ddots & \ddots & 0 \\ \vdots & \ddots & \ddots & a_{N-1} & b_{N-1} & c_{N-1} \\ 0 & \dots & \dots & 0 & a_N & b_N \end{bmatrix} \begin{pmatrix} w_0^n \\ w_1^n \\ \vdots \\ \vdots \\ w_{N-1}^n \\ w_N^n \end{pmatrix} = \begin{pmatrix} d_0 \\ d_1 \\ \vdots \\ \vdots \\ d_{N-1} \\ d_N \end{pmatrix}. \tag{6.25}$$

To solve (6.23), the components of (6.25) are

$$\begin{aligned} a_i &= c_i = -\frac{\Delta t}{\omega}\frac{g_{44}}{\Delta x^2}, \\ b_i &= 1 + \frac{2\Delta t}{\omega}\frac{g_{44}}{\Delta x^2} + \frac{2\Delta t}{\omega}(\alpha_1 - q_{11}\Delta\varepsilon_{33} - q_{12}\Delta\varepsilon_{22}), \\ d_i &= h(x,y) = x + \frac{\Delta t}{\omega}\Big[2q_{12}xy - 4\alpha_{11}x^3 - 6\alpha_{111}x^5\Big], \\ x &= u_i^{n-1}, \quad y = \delta_0 v_i^{n-1}, \end{aligned} \tag{6.26}$$

for $i = 2, N-1$, and $w_i^n = u_i^n$ for all i. To satisfy the boundary conditions for P_3 in (6.18), we define:

$$\begin{aligned} b_1 &= 1, \quad c_1 = 0, \quad d_1 = u_0^{n-1} \\ a_N &= 0, \quad b_N = 1, \quad d_N = u_N^{n-1}. \end{aligned} \tag{6.27}$$

Since the matrix is tridiagonal, we can easily solve it using the Thomas algorithm.

Turning our attention to (6.24), one finds that is is also a tridiagonal system, with the terms

$$\begin{aligned} a_i &= c_i = -\frac{\Delta t}{\omega}\frac{c_{11}}{\Delta x^2}, \\ b_i &= 1 - \frac{2\Delta t}{\omega}\frac{c_{11}}{\Delta x^2}, \\ d_i &= h(x,y,z) = x - \frac{2q_{12}\Delta t}{\omega}yz, \\ x &= v_i^{n-1}, \quad y = u_i^n, \quad z = \delta_0 u_i^n, \end{aligned} \tag{6.28}$$

for $i = 2, N-1$, and $w_i^n = v_i^n$ for all i. This system is updated by applying the new solution from (6.23) to the right-hand side. The boundary conditions for displacement result from the stress conditions in (6.18). For the u_1-displacement, we enforce the Dirichlet boundary condition $u_1(-L_1/2) = 0$ and the Neumann boundary condition $du_1/dx|_{x=L_1/2} = \eta_\perp$. This is accomplished by defining

$$\begin{aligned} b_1 = 1, \quad c_1 = 0, \quad d_1 = u_0^{n-1} \\ a_N = -1, \quad b_N = 1, \quad d_N = \eta_\perp \Delta x. \end{aligned} \tag{6.29}$$

A representative solution, found using this numerical procedure, is presented in Figure 6.6. The polarization in the x_3-direction is initialized using a hyperbolic tangent function where the solution asymptotes to the required boundary conditions. Recall that the numerical routine solved for the displacement in the x_1-direction, and the relationship between displacement and the strain component plotted in Figure 6.6 is $\Delta\varepsilon_{11} = u_{1,1}$. To satisfy the boundary conditions for strain, the displacement was prescribed to have a Dirichlet boundary condition on the left end such that $u_1(-L_1/2) = 0$, and a Neumann boundary condition on the right end such that $du_1/dx|_{x=L_1/2} = \eta_\perp$, where L_1 is the length of the domain in the x_1-direction. The initial condition for displacement was simply a line from $u_1(-L_1/2) = 0$ to $u_1(L_1/2) = L_1\eta_\perp$. For a given set of parameters, the number of iterations required to reach equilbrium may change. The convergence criteria for equilibrium was when the sum of the L_2-norm measures $(||\vec{a}^n - \vec{a}^{n-1}||_2)$ were less than 10^{-10}. Results are in good agreement with solutions found using finite element analysis.

Comparison with Finite Element Analysis. From literature, it has been reported that the energy through the 180° domain wall is $E_{180^\circ}^{DFT} = 132$ mJ/m^2 [48]. We measure the domain wall energy by integrating through the density,

$$E_{180^\circ} = \int_{-\infty}^{\infty} (u - u_0) dx_1. \tag{6.30}$$

Evaluation of (6.30) requires numerically approximating over an interval that includes the domain wall. The energy density away from the domain wall will be zero as we have subtracted the homogeneous energy solution. The remaining energy density should just be that associated with the domain wall. By using the domain wall energy reported in literature, we can analyze the uncertainty associated with the continuum approximation for the 180° domain wall structure. The results from the uncertainty analysis are presented in

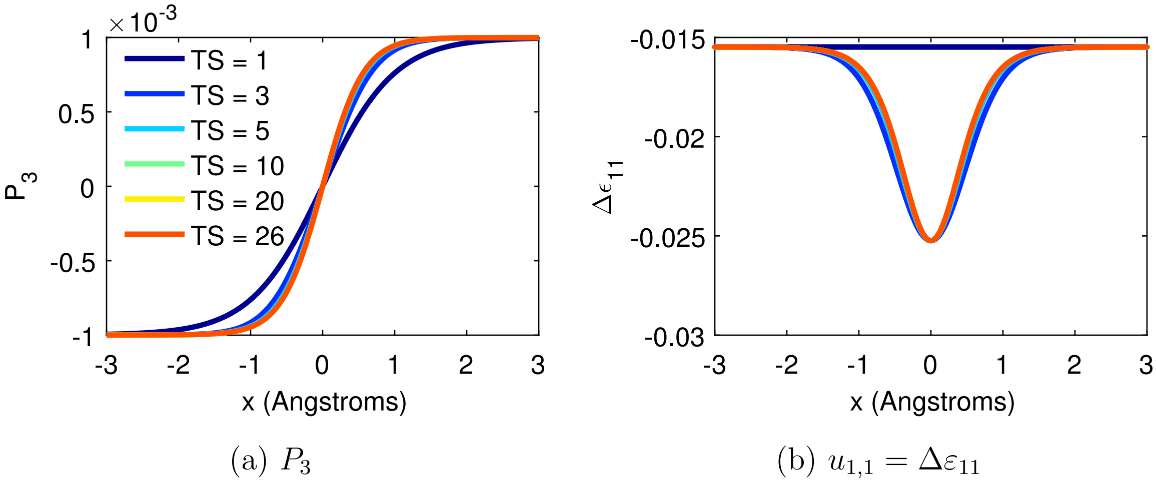

(a) P_3 (b) $u_{1,1} = \Delta\varepsilon_{11}$

Figure 6.6: Numerical solution for 180° domain wall polarization in the P_3-direction and the strain component, $\Delta\varepsilon_{11}$. Note, for a given set of parameters it took 26 time steps (TS) to meet convergence requirements.

Section 7.3.1. Before performing the uncertainty analysis it is important to test whether our finite-difference approximation is accurately modeling the physics. To do this we compare the algorithm presented above with the solution found from Finite Element Analysis (FEA).

The energy associated with the domain wall structure can be found by taking the difference between the polydomain u and the homogeneous energy solutions u_0. As seen in Figure 6.7(a), the finite-difference approach for $u - u_0$ is qualitatively in agreement with the finite element analysis solution for a consistent set of parameters. This comparison can also be made with regard to the different components of the energy density, so the Landau energy is shown in Figure 6.7(b) as a representative comparison. Furthermore, we can evaluate (6.30) for each energy component, and we find that the Landau, elastic, electrostrictive, and gradient energy for the finite-difference and finite element approach are in good agreement as seen in Table 6.2. The strength of this agreement is a good indication that the finite-difference model is a reasonable approximation for the 180° domain wall structure.

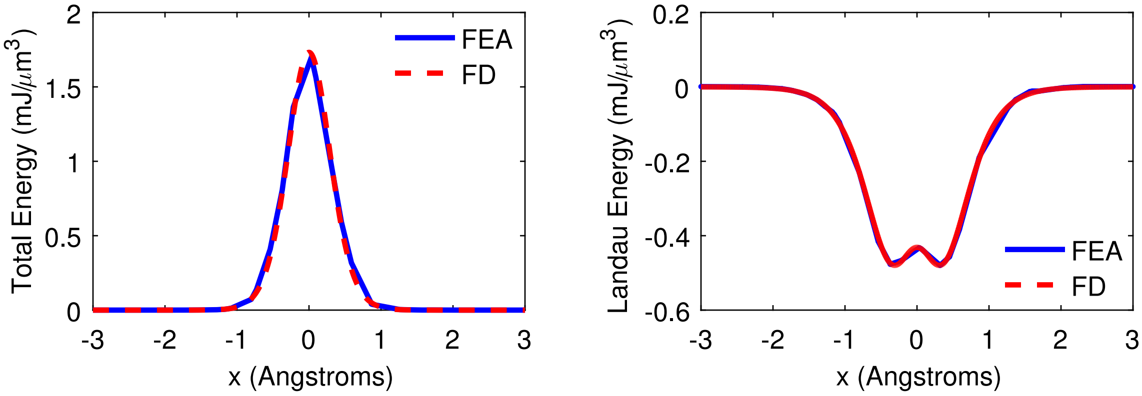

(a) Total Energy (u) (b) Landau Energy (u_L)

Figure 6.7: Energy density over 180° domain wall. Results from finite-difference (FD) approach agree well with finite element (FEA) solution using a consistent set of parameters.

Table 6.2: This table summarizes the energy contributions as calculated via (6.30) for each energy component for both finite element (FEA) and finite-difference (FD) approximations of the 180° domain wall structure. All units for energy are in mJ/m^2.

Energy Component		Method FEA	FD	Difference FEA-FD
Elastic	u_M	1.39	-2.28	3.673
Landau	u_L	-79.32	-80.10	0.775
Electrostrictive	u_C	146.22	148.37	-2.151
Gradient	u_G	64.96	65.99	-1.038
Total	u	133.40	131.99	1.412

6.6 Concluding Remarks

In this chapter we have shown the basic theory associated with the continuum phase field model. This theory has covered the calculation of energy and stress in monodomain structures, and also introduced numerical algorithms for solving 180° domain wall structures. The phase field model contains many unknown phenomenological parameters, which we can infer using the Bayesian calibration methods discussed in Chapter 2. We discuss the application of uncertainty analysis to ferroelectric domain structures in Chapter 7.

CHAPTER 7

FERROELECTRIC DOMAIN STRUCTURE EVOLUTION: UNCERTAINTY ANALYSIS

7.1 Introduction

The atomic structure of lead titantate ($PbTiO_3$) is nontrivial to analyze. It is beneficial to break the analysis into different parts. The physical contraints of the problem allow us to perform the uncertainty analysis in four distinct sections. First, in Sections 7.2.1 and 7.2.2 we will consider the energy and stress associated with monodomain structures, from which we can quantify the uncertainty associated with the Landau as well as electrostrictive parameters. The exchange parameters can only be identified in the presence of polydomain structures which introduce polarization gradients. The uncertainty analysis associated with the 180° domain structure is presented in Section 7.3.1.

7.2 Monodomain Structures

7.2.1 Model Calibration: Energy

In Section 6.3 we discussed the theory behind modeling domain structure evolution, and here we will highlight the work that has been done on quantifying the uncertainty associated with monodomain structures. The phenomenological parameters associated with the Landau energy, seen in Equation (6.3), are calibrated using Bayesian statistical methods outlined in Chapter 2. The physics associated with monodomain energy and stress can be decoupled because the electrostrictive energy is zero since the strain is set to zero in the reference cubic state. This allows us to analyze the parameter uncertainty associated with the Landau energy and electrostrictive stresses separately. The parameter set under consideration for the monodomain energy analysis is

$$\theta_u = [\alpha_1, \alpha_{11}, \alpha_{12}, \alpha_{111}, \alpha_{112}]. \tag{7.1}$$

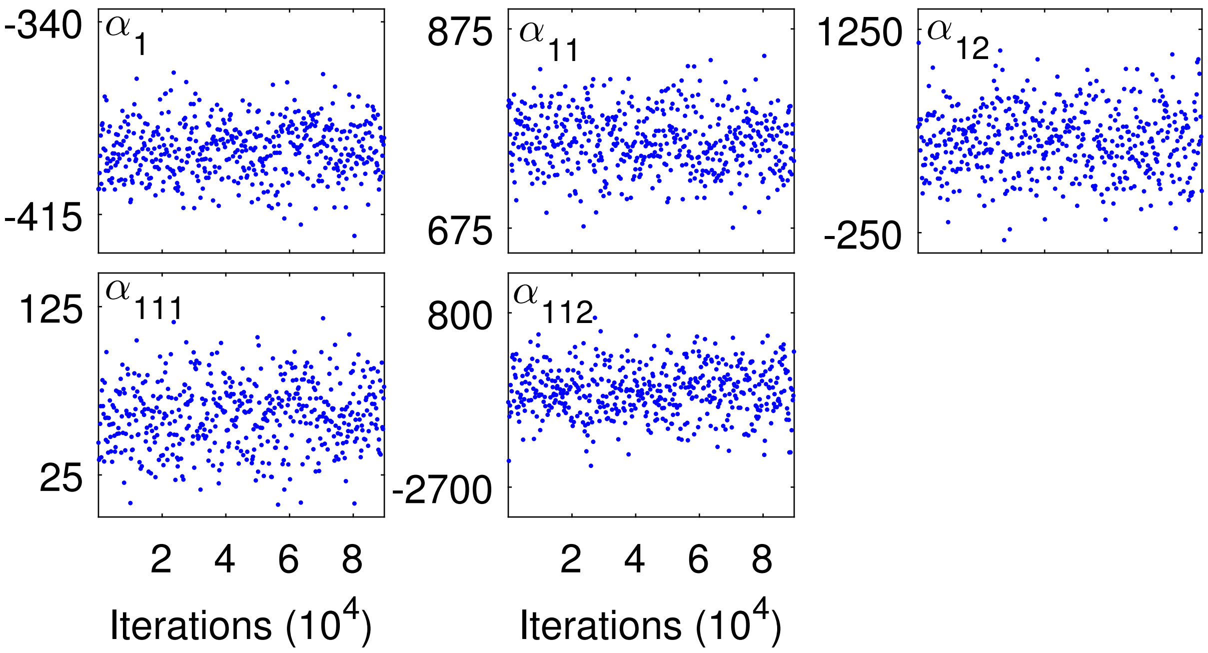

Figure 7.1: Parameter chains for calibration of phase field model parameters with respect to DFT energy measurements for monodomain structures.

The set, θ_u, is the Landau energy parameters, which are calibrated by comparison with DFT calculations of the monodomain energy for different polarization states. Note that the polarization was constrained to move from the P_3 to the P_2 direction and that there was no polarization in the x_1-direction (making α_{123} unidentifiable).

We performed MCMC sampling on the energy model with the parameter set, θ_u, and successfully quantified the uncertainty associated with the Landau energy parameters. The sampling history for each parameter chain is seen in Figure 7.1. The Landau parameters clearly have the appearance of white noise and have burned-in to the posterior densities shown in Figure 7.2. All posterior distributions appear to be Gaussian, so taking the mean as the nominal value when considering polydomain structures is a reasonable assumption. Finally, several nearly single-valued linear relationships can be seen in Figure 7.3. The strongest relationships are observed between the pairs, (α_1, α_{11}), (α_{11}, α_{111}), and (α_{12}, α_{112}). These relationships are not surprising given the definition of the Landau energy given in (6.3). A summary of the Landau parameter statistics is reported in Table 7.1.

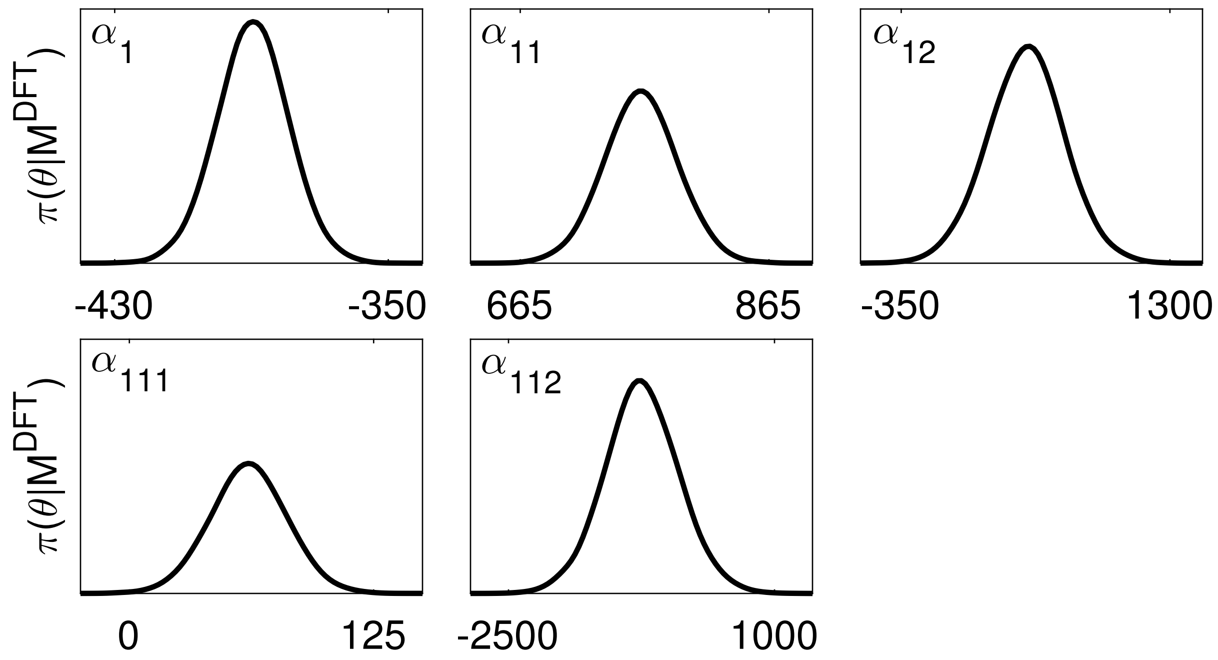

Figure 7.2: Marginal posterior densities for calibration of phase field model parameters with respect to DFT energy measurements for monodomain structures.

In the case of the monodomain energy measurements, there is a relatively small amount of uncertainty associated with the Landau parameters. By propagating the uncertainty seen in Figure 7.2 through the model, we can generate 95% prediction and credible intervals to highlight the amount of uncertainty in the output, as seen in Figure 7.4(a). It can be somewhat challenging to distinguish the uncertainty in the energy density in the plot across the entire polarization space. To highlight the uncertainty, Figures 7.4(b) and 7.4(c) show

Table 7.1: A summary of the continuum material parameters determined using Bayesian statistics and the MCMC/DRAM methods.

Parameter	Mean Value	Standard Deviation	Units
α_1	-389.4	10.49	MV·m/C
α_{11}	761.3	30.01	MV·m^5/C^3
α_{12}	414.1	241.6	MV·m^5/C^3
α_{111}	61.46	19.98	MV·m^9/C^5
α_{112}	-740.8	499.4	MV·m^9/C^5

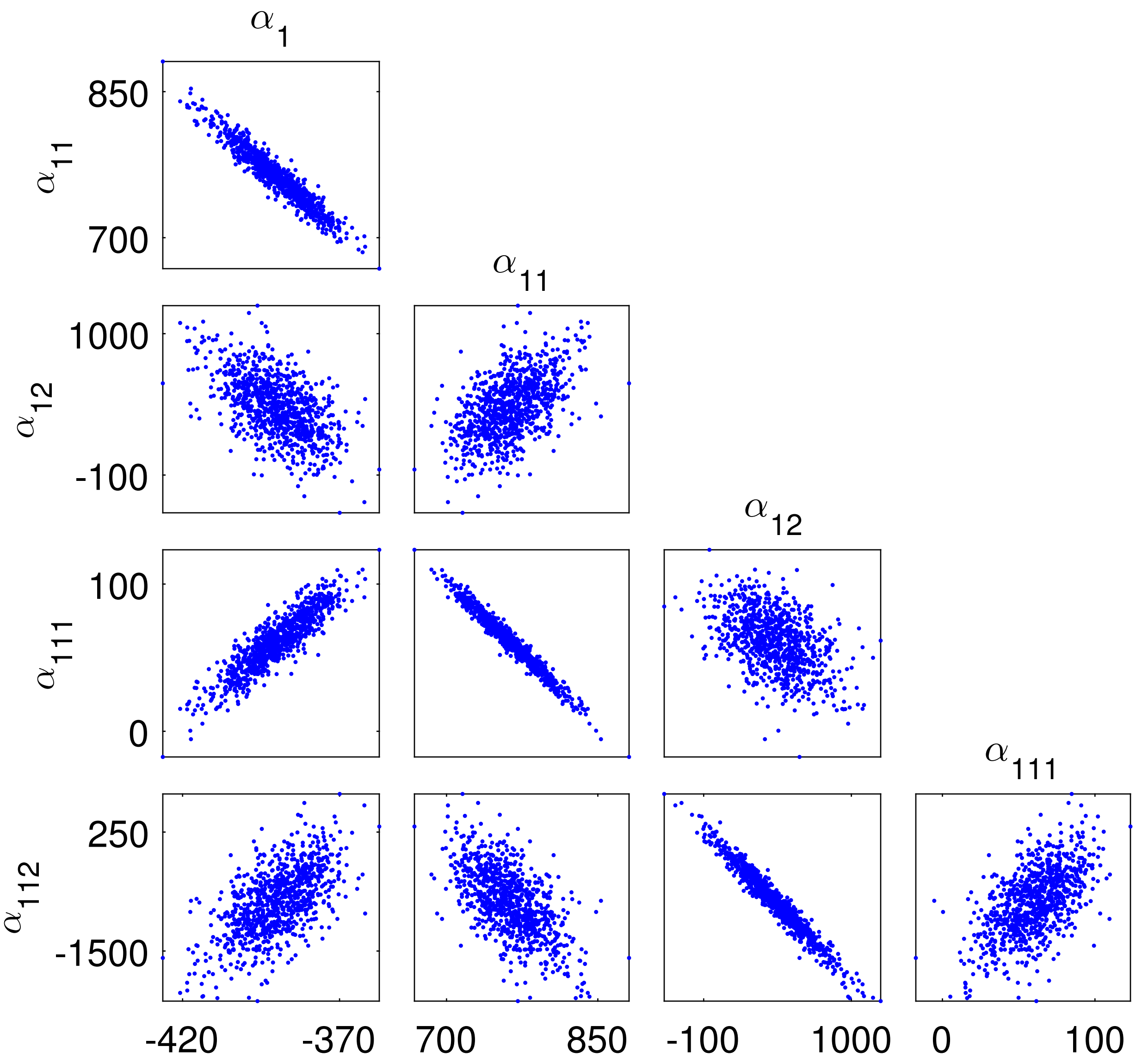

Figure 7.3: Pairwise correlation between each sampled parameter for calibration of phase field model parameters with respect to DFT energy measurements for monodomain structures. A nearly single-valued linear correlation is observed between several parameters.

lines 1 and 4, respectively, from the polarization data sets.

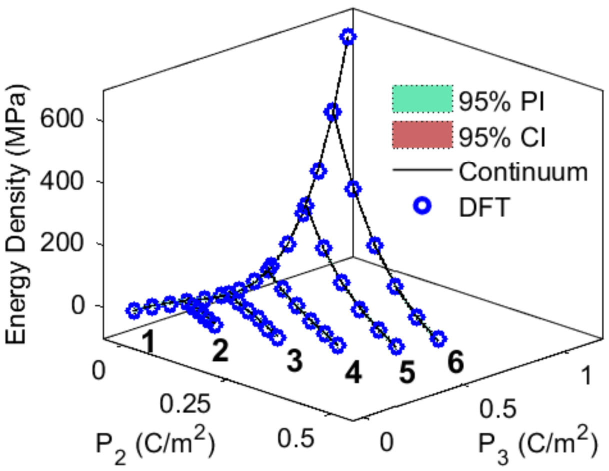

(a) Monodomain Energy Density in P_2P_3-Polarization Space

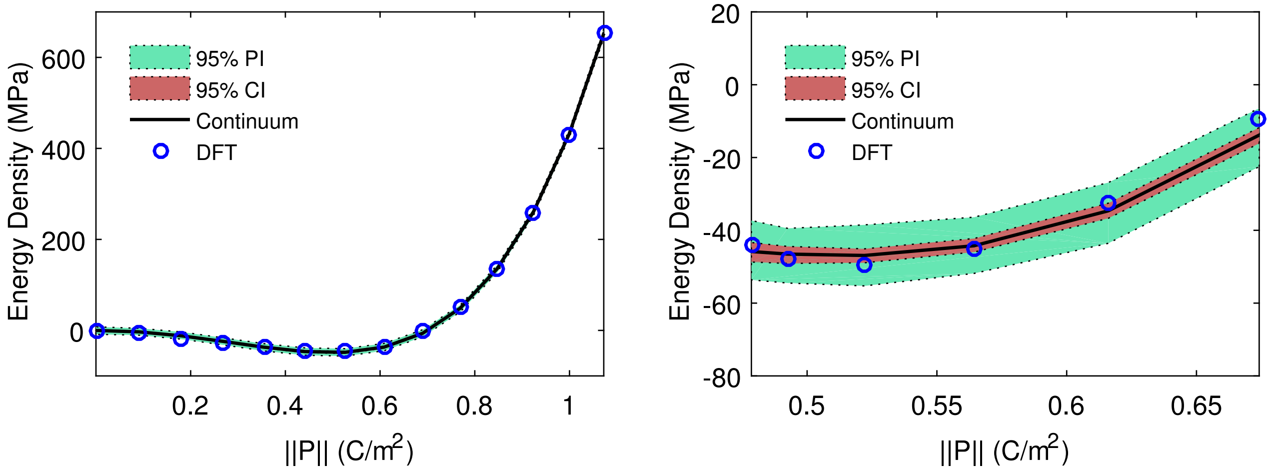

(b) Line 1

(c) Line 4

Figure 7.4: 95% prediction (PI) and credible (CI) intervals for monondomain energy model. (a) Model comparison with all DFT calculations in 3D polarization space. (b,c) Two-dimensional representations of lines 1 and 4 with respect to polarization.

7.2.2 Model Calibration: Stresses

The second calibration study identifies the electrostrictive parameters found in (6.4) as well as a set of residual stresses that arise due to the presence of spontaneous strain. These parameters can be divided into two sets as follows,

$$\begin{aligned}
\theta_{\sigma} &= [\theta_{\sigma_{ns}}, \theta_{\sigma_s}], \\
\theta_{\sigma_{ns}} &= [q_{11}, q_{12}, \sigma^R_{11}, \sigma^R_{22}, \sigma^R_{33}], \\
\theta_{\sigma_s} &= [q_{44}, \sigma^R_{23}].
\end{aligned} \tag{7.2}$$

We can calibrate these parameters by using the model equations given in (7.3) and comparing them with the DFT calculations for monodomain stresses. As discussed Section 6.2, the monodomain DFT calculations were performed such that the total strain components, ε_{ij}, are zero. Furthermore, the polarization space studied is in the P_2P_3-plane, meaning $P_1 = 0$. The final reduced set of stresses on which we will perform uncertainty quantification are

$$\begin{aligned}
\sigma_{11} &= -q_{12}(P_2^2 + P_3^2) + \sigma^R_{11}, \\
\sigma_{22} &= -q_{11}P_2^2 - q_{12}P_3^2 + \sigma^R_{22}, \\
\sigma_{33} &= -q_{11}P_3^2 - q_{12}P_2^2 + \sigma^R_{33}, \\
\sigma_{23} &= -2q_{44}P_2P_3 + \sigma^R_{23},
\end{aligned} \tag{7.3}$$

The constraint that all the polarization is in the P_2 and P_3 directions allows us to take advantage of symmetry where $\sigma^R_{11} = \sigma^R_{22}$ and $\sigma^R_{12} = \sigma^R_{13} = 0$. This assumption was confirmed through the DFT experiments, and also verified using Bayesian statistics by allowing σ^R_{11} and σ^R_{22} to be independent. Furthermore, the calibration study can be decoupled into two components. We use the notation σ_{ns} and σ_s to refer to the non-shear and shear stress parameters, respectively.

It is important to refer back to (7.3) to highlight the decoupling between the electrostrictive parameters associated with normal stress (q_{11} and q_{12}) and the shear electrostrictive coefficient (q_{44}). From (7.3) it is seen that the electrostrictive shear stress only depends on the parameters q_{44} and σ^R_{32}. Therefore, these parameters may be sampled separately from the normal stress components to determine how this influences parameter identification and uncertainty. In the following, we compare sampling all stress parameters contained within θ_σ versus the reduced set defined by θ_{σ_s}.

Similar to the results presented for the monodomain energy, a set of Bayesian statistical results are calculated for the electrostrictive stress constitutive law given by (7.3) in light of the DFT stress calculations. Again 1×10^5 iterations are calculated to ensure the parameter values are burned-in similar to the results shown in Figure 7.1. For brevity, we only show statistical results in terms of the posterior densities of the electrostrictive parameters and the residual stress. The results are in agreement with the mean and standard deviations given in Table 7.2 which show larger uncertainty in the shear coefficient q_{44} when it is identified together with all parameters in θ_σ. When θ_{σ_s} is identified separately the standard deviation of the shear parameters is reduced. Also note that the shear residual stress is nominally zero as expected; however, there is uncertainty associated with its value.

The posterior densities for both θ_σ and θ_{σ_s} are shown in Figure 7.5. All posteriors are approximately normal distributions. Importantly, we find reduced uncertainty when the shear parameters are identified independently from the normal stress parameters. The uncertainty of the normal stress parameters is unaffected by decoupling the parameter estimation. Given these posterior densities, we propagate them through the normal and shear stress components along different polarization paths to highlight propagation of error.

The model predictions of the relevant stress components along with their prediction and credible intervals are shown in Figure 7.6 using the parameter set θ_σ. Similar to the case of the Landau energy surface, reasonable prediction is observed over the range of polarization

Table 7.2: A summary of the continuum material parameters determined using Bayesian statistics and the MCMC/DRAM methods. The parameters with an asterisk were identified using $\theta_{\sigma 2}$.

Symbol	Mean Value	Standard Deviation	Units
q_{11}	19.2	0.258	GV·m/C
q_{12}	3.14	0.182	GV·m/C
q_{44}	1.39	0.538	GV·m/C
q_{44}^*	1.40	0.019	GV·m/C
σ_{11}^R	-3.977	0.103	GPa
σ_{22}^R	-3.995	0.101	GPa
σ_{33}^R	-3.410	0.118	GPa
σ_{23}^R	-4.00×10^{-4}	96.2×10^{-3}	GPa
σ_{23}^{R*}	-7.79×10^{-4}	3.32×10^{-3}	GPa

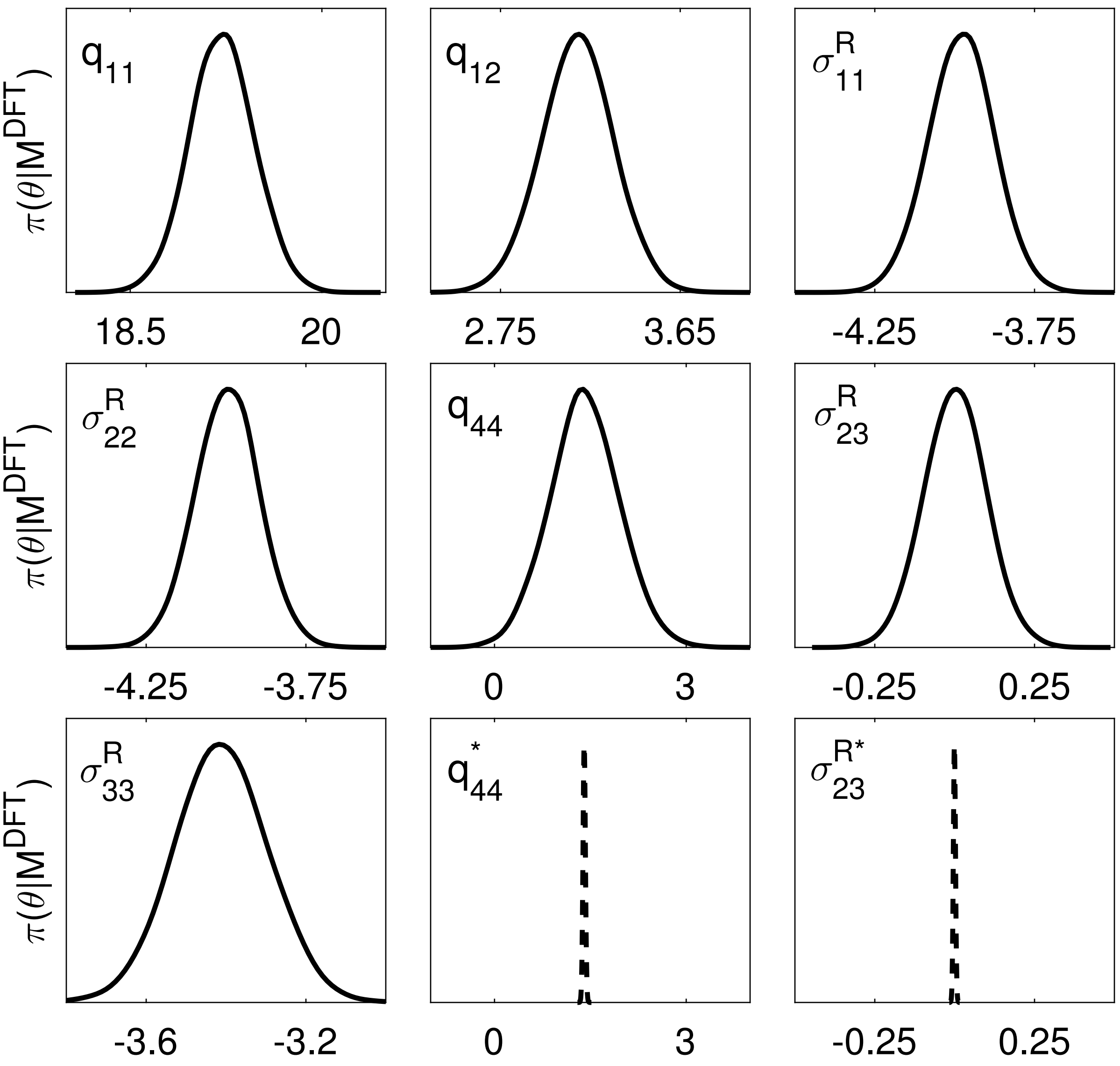

Figure 7.5: Marginal posterior densities for calibration of phase field model parameters with respect to DFT stress measurements for monodomain structures. The marginal posterior densities for the shear stress parameters are reduced if calibrated separately, as seen by the dashed lines.

values simulated; however, the range of uncertainty in electrostrictive stress is more difficult to see over the entire polarization space. Select two-dimensional plot examples examining σ_{33} and σ_{23} are shown in Figures 7.7 to further illustrate the propagation of uncertainty. Note that the error propagation in Figure 7.7(c,d) is based on the reduced uncertainty using parameters θ_{σ_s}. It is clearly shown that less uncertainty exists for the normal stress along the direction of polarization when $P_2 = 0$ (similar results are found for σ_{11} and σ_{22}). The shear stress and normal stresses for cases where $P_2 \neq 0$ exhibit larger uncertainty. This is due to the magnitude of the stress, the larger uncertainty in the shear electrostrictive parameter q_{44}, and the additional uncertainty of the shear residual stress. However, as mentioned earlier, by decoupling the parameter identification there is a significant decrease in the uncertainty contained within the shear electrostrictive and shear residual stress parameters.

7.3 Polydomain Structures

The model for the 180° domain wall structure are calibrated using Bayesian statistics. To calibrate, we must compare the models with data or results from a high fidelity simulation. We will compare the model results for the energy across the domain wall as noted by (6.30). From literature, it has been reported that the energy across the 180° domain wall is 132 mJ/m^2 [48]. This result comes from performing DFT calculations.

Recall from Chapter 2 that the adaptive Metropolis algorithm depends on the sum-of-squares difference between the model response and data, or in this case DFT, measurement - $ss = \sum_{i=1}^{N}[E^{DFT}(i) - E(i;\theta)]^2$. The sum-of-squares measure is extremely sensitive when only calculating scalar quantities such as $E_{180^\circ} = 132$ mJ/m^2. To offset this, a set of simulated data is generated using the mean value from literature with perturbations of ± 10%. The simulated data sets contained 1000 points. Introducing this perturbation is useful to stabilizing the numerical algorithm; however, it is important to remember that it will be reflected in the inferred parameter distributions.

7.3.1 180° Domain Wall

For this domain wall structure, we are interested in inferring the uncertainty associated with the exchange parameter g_{44}. Our parameter of interest is then $\theta = [g_{44}]$. Note, that for the present analysis we have assumed a decoupled problem with regard to the other unknown phenomenological parameters. In Sections 7.2.1 and 7.2.2 we discussed how the Landau and electrostrictive parameters were inferred by analysis of monodomain energy and stress.

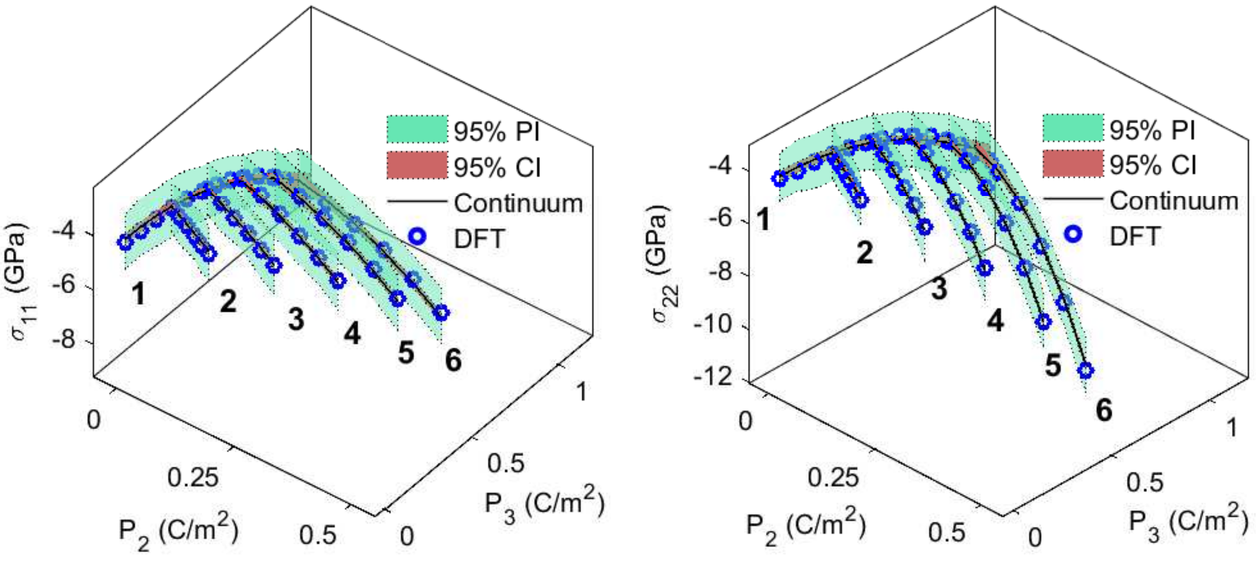

(a) σ_{11} (b) σ_{22}

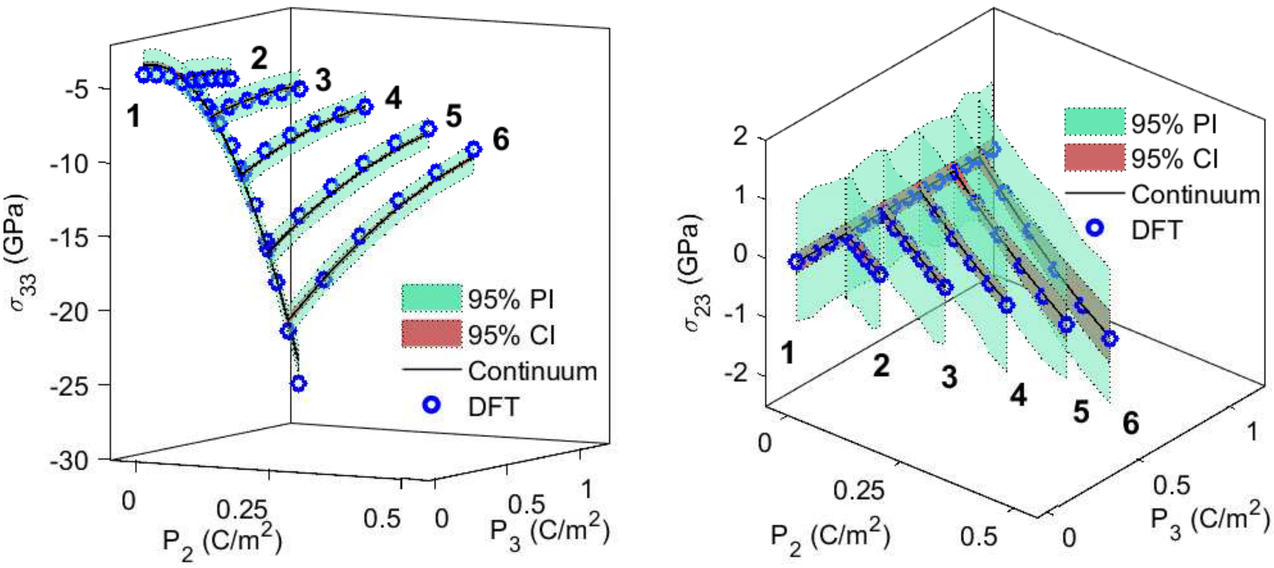

(c) σ_{33} (d) σ_{23}

Figure 7.6: Examples of the mean model estimates along with 95% prediction (PI) and credible (CI) intervals in relation to DFT stresses for (a) σ_{11} , (b) σ_{22}, (c) σ_{33} and (d) σ_{23}. Note that each plot consists of a set of stresses along different lines in the P_2P_3-plane. The lines have been numbered 1-6 for reference in later discussion.

From the calibration of the domain wall model, we can assess certain aspects of the resulting parameter chain. As seen in Figure 7.8(a), the sampling of g_{44} has the appearance of white noise, so we can say that it has “burned-in”. Furthermore, we see that the chain

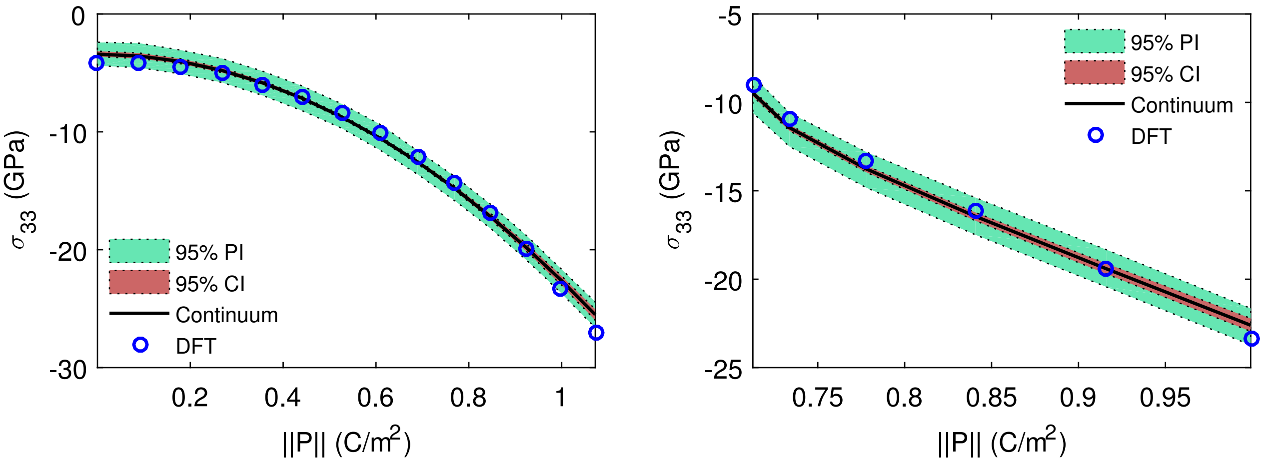

(a) σ_{33} - Line 1 (b) σ_{33} - Line 6

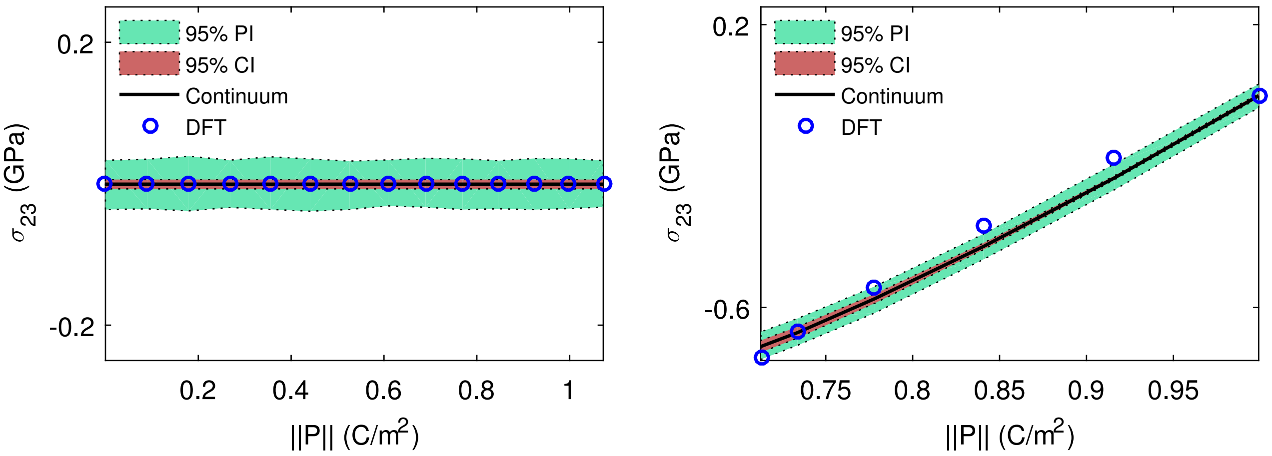

(c) σ_{23} - Line 2 (d) σ_{23} - Line 5

Figure 7.7: Two-dimensional representations of the uncertainty propagation shown in Figure 7.6. Note, (c,d) presents a contrast to Figure 7.6 in that the 95% prediction and credible intervals were generated from propagating the uncertainty from the reduced parameter set θ_{σ_s}.

has converged to the posterior density, which is shown in Figure 7.8(b).

At this point, we have quantified the uncertainty associated with the exchange parameter, g_{44}. We are now interested to see how that uncertainty propagates through the model and affects the calculation of certain quantities of interest. Furthermore, we are interested in observing how the uncertainty associated with the Landau and electrostrictive parameters affects model predictions for polydomain structures. By sampling from the posterior densities

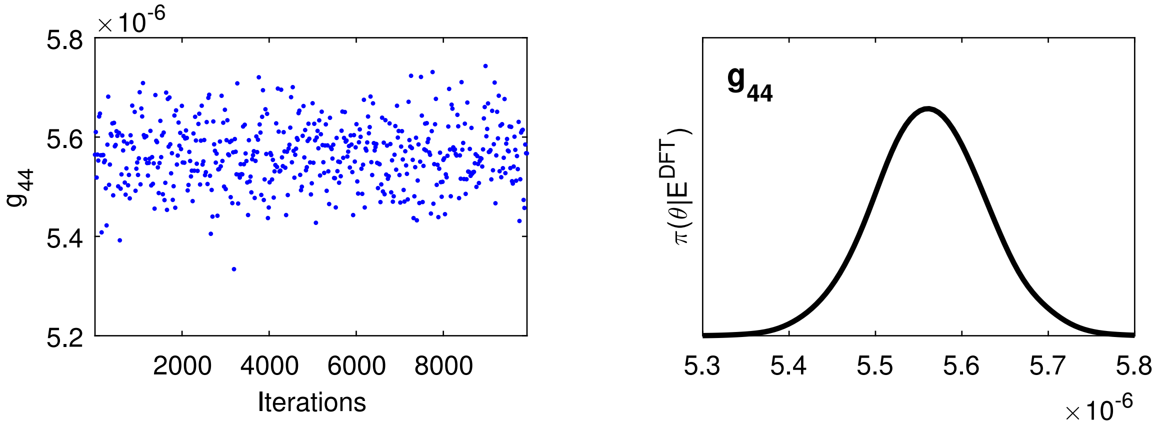

(a) Chain for g_{44} (b) Posterior Density $\pi(g_{44}|E_{180}^{DFT})$

Figure 7.8: (a) Sampling chain of g_{44}. (b) Marginal posterior density generated using a Kernel Density Estimator (KDE).

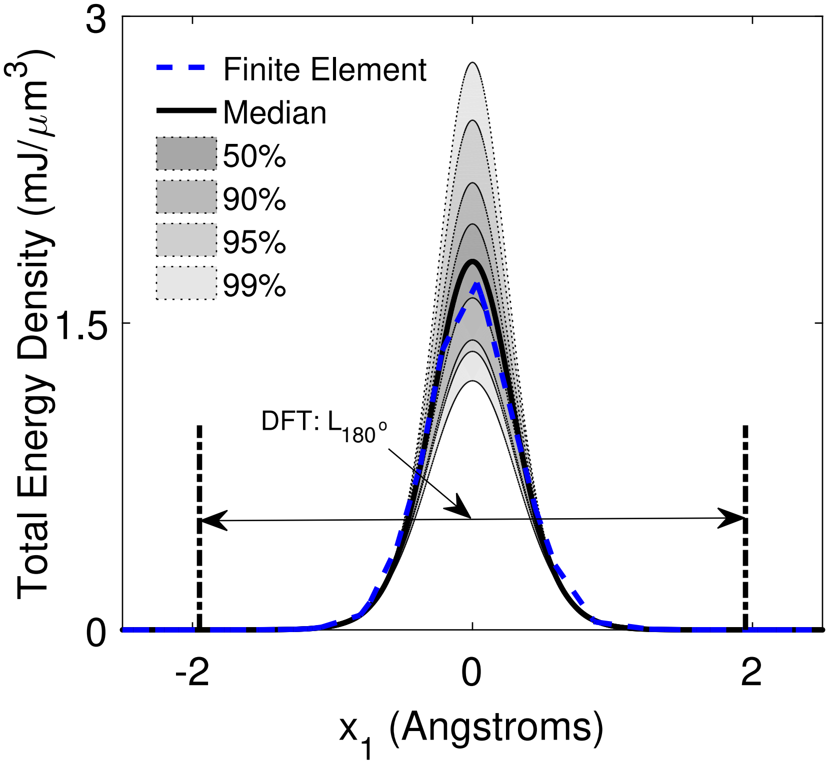

Figure 7.9: Credible intervals for energy density model of 180° domain wall structure.

and evaluating the model at each set of samples, one can generate credible intervals. The model evaluations are sorted such that one can extract $(1-\alpha)\times 100\%$ intervals. Figure 7.9 shows an array of credible intervals based on propagating uncertainty through calculations for the energy density. Most of the uncertainty is within the domain wall region as expected. Note, in addition to estimates of the domain wall energy reported in literature, there are also estimates as to the size of the domain wall. Meyer and Vanderbilt reported the domain wall width of 180° domain structures to be on the same order of magnitude as the lattice constant, $a = 3.9$ Å [48]. As seen in Figure 7.9, the domain wall energy is isolated inside the estimated domain wall width (DFT: L_{180°).

7.4 Concluding Remarks

Parameters contained within a ferroelectric monodomain model have been analyzed by comparing continuum scale model approximations to DFT energy and stress calculations. Bayesian statistics have provided information about parameter uncertainty when quantifying the energy landscape over the three dimensional polarization space. Previous analysis that considered changes in energy along the spontaneous polarization direction [54] showed relatively low uncertainty in predictions of energy and stress. Here parameter uncertainty is found to be larger during polarization rotation as highlighted by the shear related constitutive parameter posterior densities; see Figures 7.2 and 7.5. The parameter uncertainty is propagated through the continuum model to quantify prediction intervals of energy and stress along different thermodynamic paths as illustrated in Figures 7.4, 7.6, and 7.7. The larger uncertainty during polarization rotation is believed to manifest at the atomic scale when approximating the motion of multiple atoms within a unit cell in terms of a single polarization vector along directions not aligned with the spontaneous polarization.

We also performed uncertainty analysis to infer unknown exchange parameters associated with polydomain structures. We considered the exchange parameter g_{44}, and inferred its posterior density via calibration with DFT calculations of the energy across the domain wall structure. The amount of uncertainty in the exchange parameter is relatively small; however, the approximation implemented here did not account for the potential correlation between the Landau, electrostrictive, and exchange parameters. Future research will determine the extent to which parameters can be uniquely identified. Moreover, we will couple results for 180° domains with 90° domains to identify the additional exchange parameters contained within the energy function.

A quantitative comparison of the Landau, electrostrictive, elastic, and gradient energy terms found using finite difference and finite element methods enable us to identify potential areas of model improvement without introducing unnecessary intricacies which can plague Bayesian statistical analyses. Such analyses also couple closely with sensitivity analysis and should be done in parallel to identify the most relevant parameters governing the material physics.

CHAPTER 8

CONCLUDING REMARKS & FUTURE WORK

In the previous chapters we have demonstrated the advantages of performing uncertainty analysis during model development, specifically in applications related to smart materials and adaptive structures. Quantifying the uncertainty in model input parameters and propagating that uncertainty through the model provides more realistic limits on the predictive limits of the model. Analysis of this information provides us with an opportunity to refine our model and identify the greatest sources of uncertainty. Also, by considering the correlation between model parameters, it highlighted the importance of performing sensitivity analysis which can lead to model reduction.

In Chapter 3 we analyzed the uncertainty associated with modeling viscoelasticity in a linear and nonlinear framework. The rate dependent nature of the model parameters motivated the search for an alternative approach, which led to the use of fractional order calculus in Chapter 4. The new viscoelastic model was found to predict the material behavior well across the entire range of deformation rates tested. Our analysis of each model was enhanced by considering the uncertainty at each step, and propagating the uncertainty put realistic bounds on the model output.

We applied the same techniques on considering the electromechanical behavior of the dielectric elastomer VHB 4910 in Chapter 5. By using two different sources of evidence we demonstrated many of the challenges associated with data fusion as well as the importance of testing calibration results against data not used to train the model. The homogeneous model assumption reasonably approximates the electromechanical behavior during transverse loading; however, the permittivity found is not consistent with the results obtained from the rate dependent dielectric model. The next step is to test inhomogeneous model to determine whether a rate dependent permittivity term is required.

The same techniques were applied in consideration of ferroelectric domain wall structures in Chapters 6 and 7. The continuum approximation of the electronic and atomic structures results in many different levels of uncertainty. In considering the ferroelectric lead titanate, we quantified the uncertainty associated with monodomain Landau and electrostrictive parameters. The analysis of polydomain structures is required to identify the exchange parameters. The theoretical model development as well as uncertainty analysis was discussed for 180° domain wall structures. Ongoing efforts are focused on applying the same principles in the analysis of 90° domain wall structures, and also considering the potential correlation between monodomain and polydomain model parameters.

8.1 Publications & Proceedings

Journal Publications

- Miles, P., Hays, M., Smith, R., Oates, W., "Bayesian Uncertainty Analysis of Finite Deformation Viscoelasticity." *Mechanics of Materials*, 2015, Vol. 91, pp. 35-49.
- Mashayekhi, S., Miles, P., Hussaini, M. Y., Oates, W., "Fractional Viscoelasticity in Fractal and Non-Fractal Media: Theory, Experimental Validation, and Uncertainty Analysis." *Mechanics and Physics of Solids*, 2017, *submitted for review.*
- Miles, P., Leon, L., Smith, R., Oates, W., "Analysis of a Multi-axial Quantum-Informed Ferroelectric Continuum Model: Part I Uncertainty Quantification." *Intelligent Material Systems and Structures*, 2017, *submitted for review.*
- Leon, L., Smith, R., Oates, W., Miles, P., "Analysis of a Multi-axial Quantum-Informed Ferroelectric Continuum Model: Part II Sensitivity Analysis." *Intelligent Material Systems and Structures*, 2017, *submitted for review.*
- Miles, P., Moura, A., Gao, W., Hussaini, M. Y., Oates, W., "Uncertainty Analysis of Dielectric Elastomer Membranes Under Electromechanical Loading." 2017, Smart Materials and Structures, *in preparation.*

Conference Proceedings:

- Miles, P., Leon, L., Smith, R., Oates, W. "Uncertainty Analysis of Ferroelectric Polydomain Structures." *ASME Smart Materials, Adaptive Structures, and Intelligent Systems*, 2017, *accepted.*

- Leon, L., Smith, R., Oates, W., Miles, P. "Identifiability and Active Subspace Analysis for a Polydomain Ferroelectric Phase Field Model." *ASME Smart Materials, Adaptive Structures, and Intelligent Systems*, 2017, *accepted.*
- Oates, W., Miles, P., Gao, W., Clark, J., Mashayekhi, S., Hussaini, M.Y. "Rate Dependent Constitutive Behavior of Dielectric Elastomers and Applications in Legged Robotics." *SPIE Smart Structures and Materials + Nondestructive Evaluation and Health Monitoring*, 2017.
- Miles, P., Leon, L., Smith, R., Oates, W. "Uncertainty Analysis of Continuum Phase Field Modeling in 180 Degree Domain Wall Structures." *SPIE Smart Structures and Materials + Nondestructive Evaluation and Health Monitoring*, 2017.
- Leon, L., Smith, R., Miles, P., Oates, W. "A Quantum-Informed Homogenized Energy Model for Ferroelectric Materials." *SPIE Smart Structures and Materials + Nondestructive Evaluation and Health Monitoring*, 2017.
- Leon, L., Smith, R., Oates, W., Miles, P. "Sensitivity Analysis of a Quantum Informed Ferroelectric Energy Model." *ASME Smart Materials, Adaptive Structures, and Intelligent Systems*, 2016.
- Oates, W., Miles, P., Leon, L., Smith, R. "Uncertainty Analysis of Continuum Scale Ferroelectric Energy Landscapes Using Density Functional Theory." *SPIE Smart Structures and Materials + Nondestructive Evaluation and Health Monitoring*, 2016.
- Miles, P., Guettler, A., Hussaini, M. Y., Oates, W. "Uncertainty Analysis of a Dielectric Elastomer Membranes Under Multi-Axial Loading." *ASME Smart Materials, Adaptive Structures, and Intelligent Systems*, 2015. Best Student Paper Award in Mechanics & Behavior of Active Materials.
- Miles, P., Hays, M., Smith, R., Oates, W. "Uncertainty Analysis of a Finite Deformation Viscoelastic Model." *ASME Smart Materials, Adaptive Structures, and Intelligent Systems*, 2014.
- Miles, P., Archibald, C. M. "Experimental Investigation of Bicycle Frame FEA Models." *ASME International Mechanical Engineering Congress and Exposition*, 2013.
- Oates, W., Hays, M., Miles, P., Smith, R. "Uncertainty Quantification and Stochastic Based Viscoelastic Modeling of Finite Deformation Elastomers," *SPIE Smart Structures and Materials + Nondestructive Evaluation and Health Monitoring*, 2013.

- Miles, P., Archibald, C. M. “Experimental Determination of Operational Pedal Cycle Frame Loads.” *ASEE North Central Section Conference*, 2012.

APPENDIX A

SUPPLEMENTAL MATERIAL

A.1 Dempster-Shafer Theory of Evidence

Many engineering problems are not conducive to sampling based methods. Although computational speed has dramatically increased, many problems still take hundreds or thousands of computational hours to solve with a single set of parameter values, making sampling inconceivable. Similarly, many experiments are only capable of retrieving a limited number of data points, making a probabilistic approach unrealistic. In such circumstances it is often ideal to approach uncertainty quantification from the stand point of set theory. For problems in which limited data is available, or perhaps simulation time is unreasonable, we can consider the uncertainty quantification technique known as Evidence Theory [16, 71]. The basic principles of evidence theory make it potentially useful when considering engineering problems. Previous studies have considered turbulent flow models [67], flight path trajectories [66], and also medical analysis of dosing levels [11]. Evidence theory, or more fully, Dempster-Shafer Theory of Evidence, is a more conservative method to uncertainty quantification that allows for lack of knowledge to exist in the analysis. The best way to understand this is in the form of an example. If a survey is performed asking a sample of the population to indicate whether they like a certain product, the responses are limited to“Yes”, “No”, and “I do not know.” Probabilistic techniques will simply ignore responses of “I do not know”, thereby ignoring the uncertainty associated with that response group. Those responses could be “Yes” or “No”, so if a large number of people respond in this manner, the uncertainty in the solution is extremely large.

Evidence theory, or Dempster-Shafer theory, quantifies uncertainty in two ways, giving us a measure of Belief (Bel) and Plausibility (Pl). This is in essence giving us a lower and upper bound on the likelihood of an event being the true event. Dempster argued that in the case of a nonlinear function, $y(x)$, if the probability of x is known, the only probability that can be concluded with respect to the function value, y, is the upper and lower probabilities [16]. Shafer established a mathematical description of evidence theory that deviates from the focus on probability and instead relies on evidence from finite sets [71].

In consideration of this theory, the basic concept can be outlined as follows:

1) Determine the quantity of interest.
2) Define what constitutes conflicting evidence.
3) Construct the universal set.
4) Construct the belief structure.

We desire to quantify the evidence in support of a given proposition. Suppose our quantity of interest is the elastic modulus for some new material. We may have different experimental measurements that support different values for the elastic modulus. The universal set would comprise all possible values for the quantity of interest. Conflict would occur if different sources supported different values for the elastic modulus (see Section A.1.1 for more details). The belief structure would quantify the measure of belief that the modulus is within a particular range of values or subsets. This requires us to define an m-function. The m-function will assign a value in the range [0,1] to a subset, and the value of the m-function can be interpreted as the mass or belief mass. This assignment will satisfy

$$m(\emptyset) = 0, \quad \sum_{b_i \subseteq \mathbf{U}} m(b_i) = 1. \tag{A.1}$$

where $\mathbf{U}$ is the universal set and b_i are different subsets of evidence within the universal set. The null set, $\emptyset$, must have no supporting evidence. We now have some form of belief structure but in order to have any useful meaning, it is required to have a convex shape. Convexity is reached when the mass of evidence contains a global maximum with adjacent sets all decreasing in magnitude away from the maximum (see Figure A.1). With our m-function clearly defined, we can then quantify the two key measures in evidence theory: Belief (Bel) and Plausibility (Pl). These quantities are given by

$$Bel(A) = \sum_{b_i \subseteq A} m(b_i); \quad Pl(A) = \sum_{b_i \cap A \neq \emptyset} m(b_i), \tag{A.2}$$

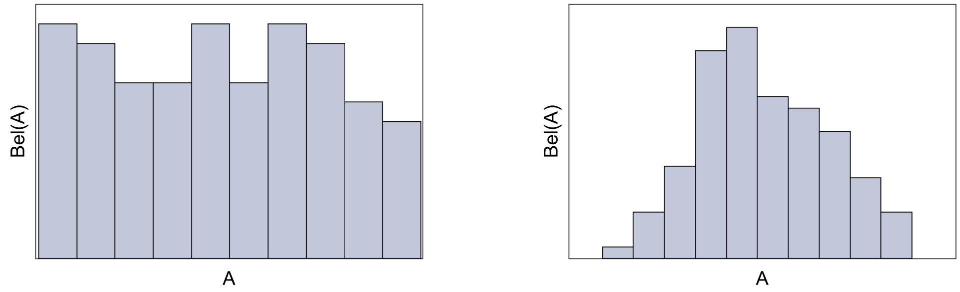

(a) Non-convex Belief Structure (b) Convex Belief Structure

Figure A.1: The shape of the belief structure must be refined for meaningful interprepation. The partitioning of the evidence must by done in such a manner that a convex belief structure (b) is generated. A structure without convex shape as seen in (a) does not allow for any meaningful statistical inference of the proposition.

where A is a proposed true value of the quantity of interest, $b_i \subseteq A$ indicates we are summing all the evidence contained in A, and $b_i \cap A \neq \emptyset$ indicates we are summing all the evidence that does not directly contradict the proposition A. The equation for plausibility can alternatively be expressed as $Pl(A) = 1 - Bel(\bar{A})$, where $\bar{A}$ is the complement of A. Understanding the distinction between belief and plausibility can be better understood by considering the Venn diagrams in Figure A.2.

The belief of $\mathbf{U}$ is equal to the sum of the mass of evidence of all the subsets of $\mathbf{U}$, i.e.,

$$Bel(\mathbf{U}) = \sum_i m(b_i) = 1 \tag{A.3}$$

where $m(b_i)$ is the mass of evidence in support of the i^{th} subset of $\mathbf{U}$. By definition, this quantity will sum to 1. However, it is important to realize that $m(\mathbf{U})$ is not equal to 1. In fact, the quantity $m(\mathbf{U})$ is the mass of uncertainty. That is to say any evidence that exists in the universal set that does not support or contradict a proposed true value. The relationship between belief, plausibility, and the universal set is presented in Figure A.3.

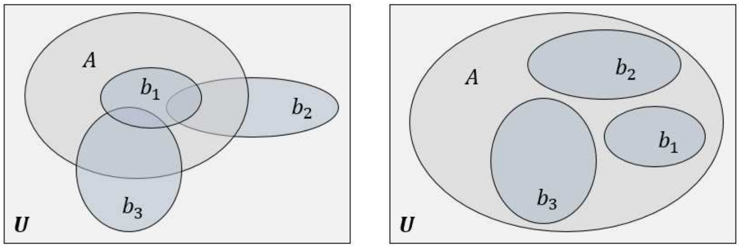

(a) $Bel(A) \neq Pl(A)$ (b) $Bel(A) = Pl(A)$

Figure A.2: Venn diagram relationships describing two cases of belief and plausibility functions. In (a), the belief and plausibility functions lead to differences since not all b_i that intersect A are subsets of A. In (b), belief and plausibility functions are equal because all sets b_i intersect A and are subsets of A. These distinctions give additional statistical information that can be used in decision making which is not contained within probability theory.

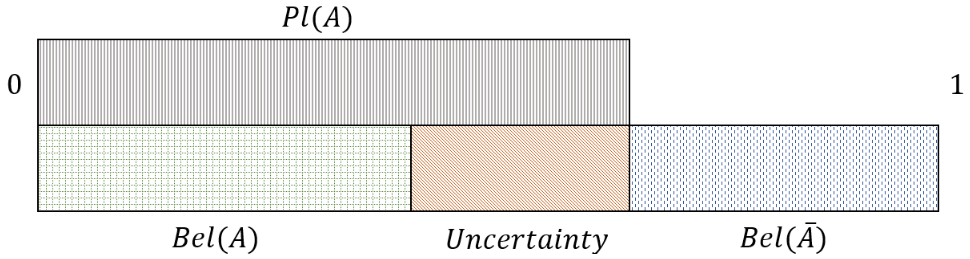

Figure A.3: Relationship between belief, plausibility, and uncertainty for a given proposition, A. The mass of uncertainty is evidence that could either support or conflict with A [28].

A.1.1 Rules of Combination

To assess the validity of a proposition we must often account for evidence from different sources. This is clearly seen in the judicial system, where each witness's testimony is weighed in light of their credibility and circumstances. In the same way, when analyzing an engineering problem we must account for data from multiple sources and find a way to combine them. Evidence theory allows us to quantify the uncertainty, and by combining different sets of evidence we can provide a broader picture of the degree of confidence we can have for a specific outcome.

Many rules of combination exist, and there are different schools of thought as to which are appropriate. Depending on the evidence being combined, a particular rule of combination may produce non-intuitive results. So, as mentioned before, this particular tool must also be assessed on a case-by-case basis as to whether or not it is applicable. Let us begin by assessing Dempster's Rule of Combination (DRC).

$$m_{1,2}(A) = \sum_{B \cap C = A \neq \emptyset} \frac{m_1(B)m_2(C)}{1-K} \tag{A.4}$$

where K is a measure of the amount of conflict defined by

$$K = \sum_{B \cap C = \emptyset} m_1(B)m_2(C). \tag{A.5}$$

We interpret $m_{1,2}(A)$ as the mass of evidence supporting proposition A based on the evidence provided by two independent sources, m_1 and m_2. Now, these two sources of evidence may or may not have coinciding sets. So, based on this definition we only add the mass when the intersection of B and C contains the proposition A. Furthermore, the metric is normalized by the conflict. As seen in (A.5) conflict occurs when the intersection of B and C is the empty set, i.e., they are nonoverlapping sets. This method for combining evidence will tend to amplify areas of agreement and dampen sets when the sources of evidence provide opposing degrees of belief. This can lead to nonintuitive results [85], so it is only presented here as an example of how combination rules can be interpreted and applied. Alternative approaches may be more appropriate depending on the quantity of interest.

REFERENCES

[1] Klas Adolfsson, Mikael Enelund, and Peter Olsson. On the fractional order model of viscoelasticity. *Mechanics of Time-dependent materials*, 9(1):15–34, 2005.

[2] Iain A Anderson, Todd A Gisby, Thomas G McKay, Benjamin M OBrien, and Emilio P Calius. Multi-functional dielectric elastomer artificial muscles for soft and smart machines. *Journal of Applied Physics*, 112(4):041101, 2012.

[3] Manuel Aschwanden and Andreas Stemmer. Low voltage, highly tunable diffraction grating based on dielectric elastomer actuators. In *The 14th International Symposium on: Smart Structures and Materials & Nondestructive Evaluation and Health Monitoring*, pages 65241N–65241N. International Society for Optics and Photonics, 2007.

[4] Ronald L Bagley and PJ Torvik. A theoretical basis for the application of fractional calculus to viscoelasticity. *Journal of Rheology (1978-present)*, 27(3):201–210, 1983.

[5] Yoseph Bar-Cohen and Qiming Zhang. Electroactive polymer actuators and sensors. *MRS bulletin*, 33(03):173–181, 2008.

[6] JS Bergström and MC Boyce. Constitutive modeling of the large strain time-dependent behavior of elastomers. *Journal of the Mechanics and Physics of Solids*, 46(5):931–954, 1998.

[7] Onur Bilgen, Carlos De Marqui jr, Kevin B Kochersberger, and Daniel J Inman. Macro-fiber composite actuators for flow control of a variable camber airfoil. *Journal of Intelligent Material Systems and Structures*, 22(1):81–91, 2011.

[8] Wenwu Cao and LE Cross. Theory of tetragonal twin structures in ferroelectric perovskites with a first-order phase transition. *Physical Review B*, 44(1):5, 1991.

[9] Louis N Cattafesta III and Mark Sheplak. Actuators for active flow control. *Annual Review of Fluid Mechanics*, 43:247–272, 2011.

[10] Long-Qing Chen. Phase-field models for microstructure evolution. *Annual review of materials research*, 32(1):113–140, 2002.

[11] Wenzhou Chen, Yunfeng Cui, Yanyan He, Yan Yu, James Galvin, Yousuff M Hussaini, and Ying Xiao. Application of dempster–shafer theory in dose response outcome analysis. *Physics in medicine and biology*, 57(17):5575, 2012.

[12] Inderjit Chopra and Jayant Sirohi. *Smart structures theory*, volume 35. Cambridge University Press, 2013.

[13] RM Christensen. A nonlinear theory of viscoelasticity for application to elastomers. *Journal of Applied Mechanics*, 47(4):762–768, 1980.

[14] Bernard D Coleman and Morton E Gurtin. Thermodynamics with internal state variables. *The Journal of Chemical Physics*, 47(2):597–613, 1967.

[15] Jacob D Davidson and NC Goulbourne. A nonaffine network model for elastomers undergoing finite deformations. *Journal of the Mechanics and Physics of Solids*, 61(8):1784–1797, 2013.

[16] Arthur P Dempster. Upper and lower probabilities induced by a multivalued mapping. *The annals of mathematical statistics*, pages 325–339, 1967.

[17] Aleksey D Drozdov. *Mechanics of viscoelastic solids.* Wiley, 1998.

[18] John D Ferry, Robert F Landel, and Malcolm L Williams. Extensions of the rouse theory of viscoelastic properties to undiluted linear polymers. *Journal of Applied Physics*, 26(4):359–362, 1955.

[19] Grant R Fowles. *Introduction to modern optics.* Courier Corporation, 2012.

[20] Søren L Frederiksen, Karsten W Jacobsen, Kevin S Brown, and James P Sethna. Bayesian ensemble approach to error estimation of interatomic potentials. *Physical review letters*, 93(16):165501, 2004.

[21] Andrew Gelman, John B Carlin, Hal S Stern, and Donald B Rubin. *Bayesian data analysis*, volume 2. Chapman & Hall/CRC Boca Raton, FL, USA, 2014.

[22] TA Gisby, SQ Xie, EP Calius, and IA Anderson. Leakage current as a predictor of failure in dielectric elastomer actuators. In *SPIE Smart Structures and Materials+ Nondestructive Evaluation and Health Monitoring*, pages 764213–764213. International Society for Optics and Photonics, 2010.

[23] Xavier Gonze, B Amadon, P-M Anglade, J-M Beuken, F Bottin, P Boulanger, F Bruneval, D Caliste, R Caracas, M Cote, et al. ABINIT: First-principles approach to material and nanosystem properties. *Computer Physics Communications*, 180(12):2582–2615, 2009.

[24] Nakhiah Goulbourne, Eric Mockensturm, and Mary Frecker. A nonlinear model for dielectric elastomer membranes. *Journal of Applied Mechanics*, 72(6):899–906, 2005.

[25] Alexei Gruverman, JS Cross, and WS Oates. Peculiar effect of mechanical stress on polarization stability in micrometer-scale ferroelectric capacitors. *Applied Physics Letters*, 93(24):242902, 2008.

[26] Heikki Haario, Marko Laine, Antonietta Mira, and Eero Saksman. Dram: efficient adaptive mcmc. *Statistics and Computing*, 16(4):339–354, 2006.

[27] Heikki Haario, Eero Saksman, and Johanna Tamminen. An adaptive metropolis algorithm. *Bernoulli*, pages 223–242, 2001.

[28] Yanyan He. *Uncertainty Quantification and Data Fusion Based on Dempster-Shafer Theory*. PhD thesis, Florida State University, 2013.

[29] Harry H Hilton and Sung Yi. The significance of (an) isotropic viscoelastic poisson ratio stress and time dependencies. *International Journal of Solids and Structures*, 35(23):3081–3095, 1998.

[30] Katie L Hoffman and Robert J Wood. Myriapod-like ambulation of a segmented microrobot. *Autonomous Robots*, 31(1):103, 2011.

[31] Gerhard A Holzapfel. On large strain viscoelasticity: continuum formulation and finite element applications to elastomeric structures. *International Journal for Numerical Methods in Engineering*, 39(22):3903–3926, 1996.

[32] Gerhard A Holzapfel. *Nonlinear solid mechanics*, volume 24. Wiley Chichester, 2000.

[33] Gerhard A Holzapfel and Juan C Simo. A new viscoelastic constitutive model for continuous media at finite thermomechanical changes. *International Journal of Solids and Structures*, 33(20):3019–3034, 1996.

[34] Zhengzheng Hu, Ralph C Smith, Nathanial Burch, Michael Hays, and William S Oates. A modeling and uncertainty quantification framework for a flexible structure with macrofiber composite actuators operating in hysteretic regimes. *Journal of Intelligent Material Systems and Structures*, page 1045389X13489781, 2013.

[35] Bernard Jaffe, William R Cook, and Hans Jaffe. *Piezoelectric ceramics*, volume 3. Elsevier, 2012.

[36] Kwangmok Jung, Jaedo Nam, Youngkwan Lee, and Hyoukryeol Choi. Micro inchworm robot actuated by artificial muscle actuator based on nonprestrained dielectric elastomer. In *Smart Structures and Materials*, pages 357–367. International Society for Optics and Photonics, 2004.

[37] Sangbae Kim, Jonathan E Clark, and Mark R Cutkosky. isprawl: Design and tuning for high-speed autonomous open-loop running. *The International Journal of Robotics Research*, 25(9):903–912, 2006.

[38] Guggi Kofod, Peter Sommer-Larsen, Roy Kornbluh, and Ron Pelrine. Actuation response of polyacrylate dielectric elastomers. *Journal of intelligent material systems and structures*, 14(12):787–793, 2003.

[39] V Kumar, M Hays, E Fernandez, W Oates, and FS Alvi. Flow sensitive actuators for micro-air vehicles. *Smart Materials and Structures*, 20(10):105033, 2011.

[40] Roderic S Lakes. *Viscoelastic materials*. Cambridge University Press, 2009.

[41] Donald J Leo. *Engineering analysis of smart material systems*. John Wiley & Sons, 2007.

[42] Malcolm E Lines and Alastair M Glass. *Principles and applications of ferroelectrics and related materials*. Oxford university press, 1977.

[43] John D Madden. Mobile robots: motor challenges and materials solutions. *Science*, 318(5853):1094–1097, 2007.

[44] Francesco Mainardi. An historical perspective on fractional calculus in linear viscoelasticity. *Fractional Calculus and Applied Analysis*, 15(4):712–717, 2012.

[45] Lawrence E Malvern. *Introduction to the Mechanics of a Continuous Medium*. Number Monograph. 1969.

[46] Somayeh Mashayekhi, Paul Miles, M. Yousuff Hussaini, and William Oates. Fractional viscoelasticity in fractal media: Theory, experimental validation, and uncertainty analysis. *Mechanics and Physics of Solids*, 2017 (submitted for review).

[47] Robert M McMeeking and Chad M Landis. Electrostatic forces and stored energy for deformable dielectric materials. *Journal of Applied Mechanics*, 72(4):581–590, 2005.

[48] B Meyer and David Vanderbilt. Ab initio study of ferroelectric domain walls in pbtio 3. *Physical Review B*, 65(10):104111, 2002.

[49] Paul Miles, Adriane Guettler, Yousuff Hussaini, and William S Oates. Uncertainty analysis of dielectric elastomer membranes under multi-axial loading. In *ASME 2015 Conference on Smart Materials, Adaptive Structures and Intelligent Systems*, pages V001T02A004–V001T02A004. American Society of Mechanical Engineers, 2015.

[50] Paul Miles, Michael Hays, Ralph Smith, and William Oates. Bayesian uncertainty analysis of finite deformation viscoelasticity. *Mechanics of Materials*, 91:35–49, 2015.

[51] Donald Frederick Nelson. *Electric, optic, and acoustic interactions in dielectrics*. John Wiley & Sons, 1979.

[52] VV Novikov and KV Voitsekhovskii. Viscoelastic properties of fractal media. *Journal of applied mechanics and technical physics*, 41(1):149–158, 2000.

[53] Jurgen Nuffer and Thilo Bein. Applications of piezoelectric materials in transportation industry. In *Global symposium on innovative solutions for the advancement of the transport industry*, volume 4, 2006.

[54] William Oates. A quantum informed continuum model for ferroelectric materials. *Smart Materials and Structures*, 23(10):104009, 2014.

[55] William S Oates, Michael Hays, Paul Miles, and Ralph Smith. Uncertainty quantification and stochastic-based viscoelastic modeling of finite deformation elastomers. In *SPIE Smart Structures and Materials+ Nondestructive Evaluation and Health Monitoring*, pages 86871O–86871O. International Society for Optics and Photonics, 2013.

[56] Zaid M Odibat and Nabil T Shawagfeh. Generalized taylors formula. *Applied Mathematics and Computation*, 186(1):286–293, 2007.

[57] Ailish OHalloran, Fergal Omalley, and Peter McHugh. A review on dielectric elastomer actuators, technology, applications, and challenges. *Journal of Applied Physics*, 104(7):9, 2008.

[58] Chan Yik Park, Anthony N Palazotto, Chad S Hale, and Hwee Kwon Jung. Internal longitudinal damage detection in a steel beam using lamb waves: Simulation and test study. *Journal of Intelligent Material Systems and Structures*, page 1045389X17708046, 2017.

[59] Mike C Payne, Michael P Teter, Douglas C Allan, TA Arias, and JD Joannopoulos. Iterative minimization techniques for ab initio total-energy calculations: molecular dynamics and conjugate gradients. *Reviews of Modern Physics*, 64(4):1045, 1992.

[60] Qibing Pei, Marcus Rosenthal, Scott Stanford, Harsha Prahlad, and Ron Pelrine. Multiple-degrees-of-freedom electroelastomer roll actuators. *Smart Materials and Structures*, 13(5):N86, 2004.

[61] Qibing Pei, Marcus A Rosenthal, Ron Pelrine, Scott Stanford, and Roy D Kornbluh. Multifunctional electroelastomer roll actuators and their application for biomimetic walking robots. In *Smart Structures and Materials*, pages 281–290. International Society for Optics and Photonics, 2003.

[62] Ron Pelrine, Roy D Kornbluh, Qibing Pei, Scott Stanford, Seajin Oh, Joseph Eckerle, Robert J Full, Marcus A Rosenthal, and Kenneth Meijer. Dielectric elastomer artificial muscle actuators: toward biomimetic motion. In *SPIE's 9th Annual International Symposium on Smart Structures and Materials*, pages 126–137. International Society for Optics and Photonics, 2002.

[63] STJ Peng, KC Valanis, and RF Landel. Nonlinear viscoelasticity and relaxation phenomena of polymer solids. *Acta Mechanica*, 25(3-4):229–240, 1977.

[64] Néstor O Pérez-Arancibia, Kevin Y Ma, Kevin C Galloway, Jack D Greenberg, and Robert J Wood. First controlled vertical flight of a biologically inspired microrobot. *Bioinspiration & Biomimetics*, 6(3):036009, 2011.

[65] Igor Podlubny. *Fractional differential equations: an introduction to fractional derivatives, fractional differential equations, to methods of their solution and some of their applications*, volume 198. Academic press, 1998.

[66] Svetlana V Poroseva, Yanyan He, M Yousuff Hussaini, and Reda R Mankbadi. Uncertainty quantification in the horizontal projection of flight plan trajectories using evidence theory. In *Proceedings of the 13th AIAA Non-Deterministic Approaches Conference, Denver, Colorado*, 2011.

[67] Svetlana V Poroseva, M Yousuff Hussaini, and Stephen L Woodruff. Improving the predictive capability of turbulence models using evidence theory. *AIAA journal*, 44(6):1220–1228, 2006.

[68] Raffaele Resta. Macroscopic polarization in crystalline dielectrics: the geometric phase approach. *Reviews of modern physics*, 66(3):899, 1994.

[69] Gianluca Rizzello, Micah Hodgins, David Naso, Alexander York, and Stefan Seelecke. Dynamic electromechanical modeling of a spring-biased dielectric electroactive polymer actuator system. In *ASME 2014 Conference on Smart Materials, Adaptive Structures and Intelligent Systems*, pages V002T02A012–V002T02A012. American Society of Mechanical Engineers, 2014.

[70] M Rubenstein and RH Colby. Polymer physics: Oxford university press, 2003.

[71] Glenn Shafer et al. *A mathematical theory of evidence*, volume 1. Princeton university press Princeton, 1976.

[72] David Sholl and Janice A Steckel. *Density functional theory: a practical introduction.* John Wiley & Sons, 2011.

[73] JC Simo. On a fully three-dimensional finite-strain viscoelastic damage model: formulation and computational aspects. *Computer methods in applied mechanics and engineering*, 60(2):153–173, 1987.

[74] Ralph C Smith. *Smart material systems: model development*, volume 32. Siam, 2005.

[75] Ralph C Smith. *Uncertainty quantification: theory, implementation, and applications*, volume 12. SIAM, 2013.

[76] Ralph C Smith and Zhengzheng Hu. Homogenized energy model for characterizing polarization and strains in hysteretic ferroelectric materials: Material properties and uniaxial model development. *Journal of Intelligent Material Systems and Structures*, 23(16):1833–1867, 2012.

[77] Hyun Jeong Song, Young-Tai Choi, Norman M Wereley, and Ashish S Purekar. Energy harvesting devices using macro-fiber composite materials. *Journal of Intelligent Material Systems and Structures*, 21(6):647–658, 2010.

[78] Yu Su and Chad M Landis. Continuum thermodynamics of ferroelectric domain evolution: theory, finite element implementation, and application to domain wall pinning. *Journal of the Mechanics and Physics of Solids*, 55(2):280–305, 2007.

[79] Kenji Uchino. *Ferroelectric Devices 2nd Edition.* CRC press, 2009.

[80] Kenji Uchino and Jayne Giniewicz. *Micromechatronics.* CRC Press, 2003.

[81] Dejan Vasic, Emmanuel Sarraute, François Costa, Patrick Sangouard, and Eric Cattan. Piezoelectric micro-transformer based on pzt unimorph membrane. *Journal of Micromechanics and Microengineering*, 14(9):S90, 2004.

[82] Michael Wissler and Edoardo Mazza. Electromechanical coupling in dielectric elastomer actuators. *Sensors and Actuators A: Physical*, 138(2):384–393, 2007.

[83] Robert J Wood. The first takeoff of a biologically inspired at-scale robotic insect. *IEEE transactions on robotics*, 24(2):341–347, 2008.

[84] Robert J Wood, Ben Finio, Michael Karpelson, Kevin Ma, Néstor Osvaldo Pérez-Arancibia, Pratheev S Sreetharan, Hiroto Tanaka, and John Peter Whitney. Progress on picoair vehicles. *The International Journal of Robotics Research*, 31(11):1292–1302, 2012.

[85] Lotfi A Zadeh. A simple view of the dempster-shafer theory of evidence and its implication for the rule of combination. *AI magazine*, 7(2):85, 1986.

[86] Qingsong Zhang and William A Goddard III. Charge and polarization distributions at the 90 domain wall in barium titanate ferroelectric. *Applied physics letters*, 89(18):182903, 2006.

[87] W Zhang and K Bhattacharya. A computational model of ferroelectric domains. part i: model formulation and domain switching. *Acta materialia*, 53(1):185–198, 2005.

[88] Xuanhe Zhao, Wei Hong, and Zhigang Suo. Electromechanical hysteresis and coexistent states in dielectric elastomers. *Physical review B*, 76(13):134113, 2007.

[89] Xuanhe Zhao and Zhigang Suo. Theory of dielectric elastomers capable of giant deformation of actuation. *Physical Review Letters*, 104(17):178302, 2010.

[90] Bruno H Zimm. Dynamics of polymer molecules in dilute solution: viscoelasticity, flow birefringence and dielectric loss. *The journal of chemical physics*, 24(2):269–278, 1956.

BIOGRAPHICAL SKETCH

Paul Miles was born on October 16, 1990 in Bellevue Nebraska, and his family moved to Colorado Springs, Colorado in 1991. Upon completion of the home school curriculum organized by his parents, Paul enrolled at Grove City College, where he earned his Bachelor's of Science in Mechanical Engineering in May of 2013. In August of 2013 Paul moved to Tallahassee to start in the BS/PhD program at Florida State University in the Mechanical Engineering Department under the supervision of Dr. William Oates.

Paul's research has covered a broad range of topics. His main focus has been on uncertainty analysis of the viscoelastic and electromechanical response of dielectric elastomers, and domain structure evolution of ferroelectric atomic structures. Additional interests are in fluid structure interaction and also evaluation of student learning methods.